

NANOFABRICATION USING FOCUSED ION BEAM

by

Adnan Latif

Darwin College, Cambridge



A dissertation submitted for the degree of Doctor of Philosophy in the
University of Cambridge

June 2000

Revised November 2000

To my Parents

Summary

Focused ion beam (FIB) technique uses a focused beam of ions to scan the surface of a specimen, analogous to the way scanning electron microscope (SEM) utilizes electrons. Recent developments in the FIB technology have led to beam spot size below 10 nm, which makes FIB suitable for nanofabrication. This project investigated the nanofabrication aspect of the FIB technique, with device applications perspective in several directions. Project work included construction of an in-situ FIB electrical measurement system and development of its applications, direct measurements of nanometer scale FIB cuts and fabrication and testing of lateral field emission devices. Research work was performed using a number of materials including Al, Cr, SiO₂, S₃N₄ and their heterostructures. Measurements performed included in-situ resistometric measurements, which provided milled depth information by monitoring the resistance change of a metal track while ion milling it. The reproducibility of this method was confirmed by repeating experiments and accuracy was proven by atomic force microscopy (AFM). The system accurately monitored the thickness of 50 nm wide and 400 nm thick (high aspect ratio) Nb tracks while ion milling them. Direct measurements of low aspect ratio nanometer scale FIB cuts were performed using AFM on single crystal Si, polycrystalline Nb and an amorphous material. These experiments demonstrated the importance of materials aspects for example the presence of grains for cuts at this scale. A new lateral field emission device (in the plane of the chip) was fabricated, as FIB offers several advantages for these devices such as control over sharpness and decrease in anode-to-cathode spacing. FIB fabrication achieved field emission tip sharpness below 50 nm and anode-to-cathode spacing below 100 nm. For determining the field emission characteristics of the devices, a low current (picoampere) measurement system was constructed and devices operated in ultra high vacuum (10⁻⁹ mbar) in picoampere range. One device fabricated using a FIB sharpening process had a turn on voltage of 57 V.

Preface

This thesis describes research performed at the Department of Materials Science and Metallurgy, University of Cambridge. Except where specific reference is made to the work of others, it is the result of my own work and includes nothing which is the outcome of work done in collaboration. No part of this work has been, or is being submitted for any other qualification at this, or any other university.

Some of the work described in the thesis has been published as follows:

Real Time Resistometric Depth Monitoring in the Focused Ion Beam by A. Latif, W. E. Booij, J. H. Durrell, and M. G. Blamire, *J. Vac. Sci. Techno. B* **18** (2), Mar/Apr 2000.

Nanofabrication using Focused Ion Beam by A. Latif, Accepted for publication in the *Materials World* **8**, 12 (2000).

Adnan Latif

Acknowledgments

Firstly, I would like to thank my supervisor Dr. Mark Blamire for his many suggestions, advice, encouragement and patience throughout the years. I benefited mostly from his interest in nanotechnology and expertise in microfabrication techniques. Many thanks to Dr. Zoe Barber for demonstrating microfabrication techniques and for help with deposition of thin films. I also thank Prof. Jan Evetts for his advice regarding funding, his recommendations and general encouragement.

I would also like to thank Dr. Wilfrid Booij for great help with preparing samples and performing software programming for in-situ FIB measurements. I thank Dr. Gavin Burnell for help with computing and with clean room techniques. I am grateful to Mr. David Nicol for help with scanning electron microscopes and Dr. David Foord for training me to use the focused ion beam. I should like to thank Mr. Ashish Garg and Mr. John Durrell for great help with atomic force microscope and computers. Many thanks to Dr. Jim Conyers for help with field emission measurements. I am especially grateful to Dr. Dae-Joon Kang, Mr. Ashish Garg, Mr. Yee Cheng and Mr. Rajkumar Jakkaraju for help with the writing of the dissertation. I also wish to express my appreciation for the very difficult machining the people in the workshop of Materials Department performed for the project.

I am very grateful to my parents, Cambridge Commonwealth Trust, Lundgren Research Award, Darwin College and Department of Materials Science and Metallurgy for the financial help, which made this project possible. I would also like to thank Mr. Peter Martin for the internship with SEMIKRON.

Lastly, I will like to thank my family, my friends (especially my cousins) in Pakistan, friends in England and friends in Czech Republic for the support and advice.

Table of Contents

Chapter 1: Introduction

1.1	Outline of the thesis	5
1.2	References	6

Chapter 2: Technology, Functions and Applications of the FIB

2.1	Introduction	8
2.2	The FIB system	9
2.2.1	Column	9
2.2.1.1	Liquid Metal Ion Source	11
2.2.1.2	Lens System	11
2.2.1.3	Stage, Detector and Gas Injection	12
2.2.1.4	Image Generation	12
2.2.1.5	Milling	13
2.3	Functions of the FIB	14
2.3.1	Imaging	14
2.3.2	Simple Ion Milling and Ion Milling with Enhanced Etch	15
2.3.2.1	Simple Ion Milling	16
2.3.2.2	Ion Milling with Enhanced Etch	20
2.3.3	Material Deposition with the FIB	23
2.3.3.1	Chemical Assisted Deposition	23
2.3.3.2	Direct Deposition	26
2.3.4	End Point Detection using Absorbed Current	27
2.4	Applications of the FIB	31
2.4.1	Repair of Lithographic Masks and Integrated Circuits	31
2.4.2	Defect Analysis	32
2.4.3	Transmission Electron Microscope Specimen Preparation	34
2.4.4	Channeling Contrast	35

2.5	Ion Lithography, Suspended Structures and Other Applications of the FIB	36
2.5.1	Ion Lithography and Doping	36
2.5.2	Suspended Structures	37
2.5.3	General Micromachining	38
2.5.4	Device Fabrication	39
2.5.5	General FIB Fabrication	40
2.6	Summary	40
2.7	References	41

Chapter 3: Experimental Fabrication and Measurement Methods

3.1	Introduction	45
3.2	Specimen Fabrication	46
3.2.1	Thermal Oxidation	46
3.2.2	Sputter Deposition	47
3.2.3	Photolithography	48
3.2.4	Al Dissolution, Advanced Scanning Electron Microscope Specimen Preparation and Other Methods	50
3.2.4.1	Al Dissolution	50
3.2.4.2	Advanced Scanning Electron Microscope Specimen Preparation	51
3.2.4.3	Metal Deposition by Chemical Displacement and Other Methods	51
3.3	Measurement Systems and Methods	53
3.3.1	Low Level Current Measurements	53
3.3.2	Field Emission Measurements in Ultra High Vacuum	56
3.3.3	In-situ FIB Measurement System	60
3.3.3.1	Field Emission Measurements in the FIB	64
3.3.3.2	Heating inside the FIB	65
3.3.3.3	Four Point Resistance Measurements	68
3.4	Summary	68

3.5	References	68
------------	-------------------	----

Chapter 4: Real Time Resistometric Depth Monitoring in the FIB

4.1	Introduction	70
4.2	Thickness Measurement Techniques for High Aspect Ratio Cuts	71
4.2.1	General Thickness Measurement Techniques	71
4.2.2	Absorbed Current Method, Difficulties and Limitations	72
4.2.3	Model Resistometric Depth Monitoring Technique	72
4.3	Measurements	75
4.3.1	Verification and Reproducibility of the Technique	76
4.3.2	High Aspect Ratio Structures	80
4.4	Summary	82
4.5	References	83

Chapter 5: Direct Measurements of the FIB Cut Parameters

5.1	Introduction	84
5.2	Comparison of Techniques, Definitions and Reliability	85
5.3	Experimental Scheme	91
5.4	Results and Discussion	96
5.4.1	Measurements of FIB Cuts in Si	96
5.4.1.1	150 pA Beam Current (Simple Ion Milling)	96
5.4.1.2	70 pA Beam Current (Simple Ion Milling)	107
5.4.1.3	150 pA Beam Current (Enhanced Etch)	109
5.4.1.4	70 pA Beam Current (Enhanced Etch)	114
5.4.1.5	Comparison Enhanced Etch milling and Simple Ion Milling (Si)	116
5.4.2	Width Measurements in Different Materials	118
5.5	Summary	121

5.6	References	121
Chapter 6: Lateral Field Emission Device Fabrication with the FIB		
6.1	Introduction	123
6.1.1	Applications, Difficulties, and Fabrication Processes	124
6.1.2	FIB and Field Emission	127
6.2	Fabrication Process for Field Emission Device	128
6.2.1	Preliminary Work	128
6.2.2	Materials Selection for Field Emission Device	130
6.2.3	Initial Field Emission Device Fabrication	130
6.2.4	Modification of the Device Fabrication Process	131
6.2.5	Final Structure of Field Emission Device	134
6.3	Field Emission Device Variables	136
6.3.1	Sharpening of the Field Emission Device	136
6.3.2	Anode-to-Cathode Spacing of the Field Emission Device	145
6.3.3	Geometric Shapes of the Field Emission Device	146
6.4	Summary	147
6.5	References	148
Chapter 7: Lateral Field Emission Device Measurements		
7.1	Introduction	150
7.2	Field Emission Theory	151
7.2.1	Image Force	153
7.2.2	Wentzel-Kramers-Brillouin Approximation	154
7.2.3	Fowler Nordheim Equation	154
7.3	Field Emission Measurements	157
7.3.1	In-situ FIB Experiments on the Field Emission Device	158
7.3.1.1	Measurements	158
7.3.2	Arcing and Poisoning	159
7.3.3	Testing of the Field Emission Device in Ultra High Vacuum	163
7.3.3.1	Field Emission Measurements (chip # 34)	163

7.3.3.2	Field Emission Measurements (chip # 56)	165
7.3.3.3	Comparison and Discussion	167
7.4	Summary	168
7.5	References	169
Chapter 8: Conclusions and Future Work		
8.1	Conclusions	170
8.2	Future Work	173
8.3	References	174
Appendixes		175

Chapter 1

Introduction

Focused ion beam (FIB) technique uses a focused beam of ions to scan the surface of a specimen, analogous to the way electrons are used in a scanning electron microscope (SEM). Application of a very high electric field onto a liquid metal ion source (LMIS) generates ions, which are focused by electrostatic lenses. The development of LMIS is crucial for the development of FIB. Krohn first observed the emission of large number of charged ions along with charged droplets while performing experiments on wood metal (the eutectic alloy of Bi, Pb, Sn and Cd) for space thruster applications [1]. By mid 70's the work performed on LMIS had reached to a stage where these sources of ions could be used in a FIB.

Bombardment of the specimen surface by extracted ions from LMIS results in the generation of secondary electrons, ions and sputtered material. These different kinds of generated species are used for different functions of the FIB. Imaging function results due to secondary electrons and ions while fabrication function occurs due to sputtering. Generation of secondary electrons result from closer to the surface (10's of nm) than in a SEM (100's of nm) and the back scattered electron signal does not occur as the bombarding particles are ions. The release of an appropriate gas close the surface as Ga^+ ions bombard the specimen surface leads to additional capabilities of the FIB such as material deposition and enhanced removal of material. Different materials can be deposited for example Pt, SiO_2 etc. [2].

FIB systems are mostly used in semiconductor industry and in 1993 there were approximately 150-200 commercial systems world wide [3]. The primary advantage of FIB is the capability to form an image of the specimen and then precisely mill the material away from selected areas. The major applications of the FIB systems are failure analysis, device modification, and repair of photomasks [4,5]. New applications developed in this field include ion lithography and applications related to micromachining. This project used

a FEI (manufacturer's name) 200 series type FIB. The milling spot size of this machine can be varied from 8 nm to 500 nm, which makes it suitable for nanofabrication [6,7].

Nanos is a greek word which means dwarf, as the name suggests, nanotechnology involve things, which are small. The definition of the nano scale varies from country to country. In Germany, the definition covers anything, which is smaller than 1 μm in size. In the US, the definition covers things which are largely limited to atomic and molecular level (10^{-8} – 10^{-10} m). The UK definition takes a middle course, describing it as a technology in which dimensions and tolerances in the range of 0.1 μm to 0.1 nm perform a major part [8].

Nanofabrication, is more narrowly defined than nanotechnology which currently includes research areas ranging from microelectromechanical systems (MEMS) to protein engineering [9-11]. Nanofabrication is a progression of microfabrication, which uses two different technologies both originating predominantly in the work on Si namely microelectronics technology and micromachining technology. Microelectronics technology utilises primarily Si and its properties for fabrication. The technology builds planar structures on Si wafers and no assembly of parts is required. There is a wide spectrum of technologies used in the microelectronics industry such as photolithography, ion implantation *etc.* Micromachining technology has its roots in discoveries concerning the piezoresistive effect in Si; however, Si material is not greatly important in this area [12]. Structures are more 3-dimensional and different parts require assembling [13]. Currently various technologies are being used for micromachining such as bulk micromachining, surface micromachining *etc.* [14-16]. Presently most of the technologies for achieving nano scale feature have limitation for instance optical contact lithography is limited by Fresnel diffraction, X-ray lithography is very expensive and the masks are fragile and e-beam lithography is serial in nature thus very expensive.

The developments in the above mentioned technologies have led to a wide range of applications. Nanolithography is one of the most important applications of nanofabrication and developments in this field will determine the speed and density of electronic devices. FIB offers advantages over e-beam lithography in this field due to no back scattering of electrons while performing nanolithography thus making it suitable for performing high density lithography. There are a wide range of applications in the field of micromachining such as micromotors, nanoresonators, microsuperconductive devices,

mechanical devices and components [8-27]. These devices use different principles such as piezoelectric, electrostatic, *etc.* [28-31]. Presently FIB is used for nanofabrication in different devices such as superconductive devices and field emission devices. Applications of the FIB technology such as transmission electron microscopy (TEM) specimen preparation also extends FIB fabrication into the nano range as the specimens are 100 nm thick.

FIB technology offers a number of advantages for nanofabrication which are summarised as follows:

- The ability of the technique to perform both milling and imaging.
- Milling spot size below 10 nm, leading to fabrication of thin sections approximately 100 nm.
- Flexibility in processing, for example milling of different shapes and deposition of different materials.
- Ease of fabrication; fabrication only requires overlying patterns on the substrate surface.
- Uniqueness of this technique to mill oblique cuts.
- Minimum back scattering of electrons relative to e-beam lithography while performing nanolithography which makes it suitable for performing high density lithography.

Present FIB research work largely involves development of its new applications. Recently there is reported work on exploiting the technology for commercial applications [32].

The above-mentioned advantages of the FIB technique and the present trends of developing practical applications of the FIB provided the motivating factors for the project. It is of great importance for device applications that the current capabilities of the FIB technology should be increased. One way in which the technological capabilities of the FIB system can be increased is by building an in-situ electrical measurement system, thus offering the ability to perform electrical measurements while using different functions of the FIB. As more of the device applications involving FIB extend into the nano scale it has become very important for researchers to know about FIB cut parameters such as width of cut at this scale. Thus a study of FIB cut parameters by some direct measurement method is essential for future developments in this field. Presently there are various device applications such as field emission devices. The fabrication of lateral field emission devices with the FIB offers a number of advantages for example control over sharpness

and this leads to control over turn-on voltage. These advantages of the FIB can provide this whole area of research a new perspective.

The objectives of the work included developing new techniques in the field of nanofabrication and understanding the effect of materials properties such as grain structure and surface properties on nano scale FIB milling parameters for example the width of cut, depth of the milled structure *etc.* Development of new techniques included for example: fabrication and testing of lateral field emission devices, construction of in-situ electrical measurement system, exploring its applications and finding new methods to study the FIB milled structures for nanofabrication. An understanding of the various FIB techniques, milling, imaging *etc.* at the nano scale is essential for nanofabrication. Device fabrication with the FIB presently uses various materials, such as Nb for superconductive devices and Si for fabrication of cantilevers [3,32]. The research work involved the use of different material for example Si, Nb, Al, Cr, Si_3N_4 , SiO_2 *etc.* and their heterostructures. The study of milling of these materials is important for better understanding of FIB milling process and as it provides with useful information such as the milling rates of different materials. For device applications the shape of the FIB cut and material factors which influence the shape of the FIB cut for nanofabrication are also very important.

The project work included the building of an in-situ electrical measurement system, atomic force microscope (AFM) measurement on nano scale FIB cuts and fabrication and testing of a field emission device. An in-situ electrical measurement system increases the capability of the FIB system as different type of electrical measurements can be performed while milling or without removing the specimen from the FIB vacuum chamber. For this project, the present system was used for three different purposes: in-situ resistometric measurements, low current measurements (currents in the picoampere range) and heating of the devices. AFM measurements were performed on nano scale FIB milled cuts in single crystal Si, polycrystalline Nb and an amorphous material. A framework was established to perform AFM measurements, which is also useful for other similar measurements. This investigation increased understanding of the FIB technology and the influence of materials parameter on the milled structures such as the variation of the width of cut in a grainy material. End point detection (EPD) (which is the current signal to ground as milling is performed) was used for the study of Cr/Al/ SiO_2 structure, which increased understanding of the complexity of the milling process. This technique was also

used to calculate the milling rates and sputter yield of different materials. The fabrication of field emission devices proved to be very successful as a new field emission device was fabricated which exploits the flexibility of the technique. Devices with different materials and dimensions can be easily fabricated. Field emission devices were fabricated on chip and operated in ultra high vacuum (UHV). A FIB device sharpening process resulted in device turn-on voltage of 57 V.

1.1 *Outline of the thesis*

Chapter 2 discusses the FIB technology, its applications and different functions. Applications section discusses the different commercial and research applications. FIB functions section discusses different functions such as imaging, milling, deposition and EPD technique. Different experiments performed during the project demonstrated different capabilities of the FIB. These are presented with the discussion of the working of the various functions, applications *etc.*

Chapter 3 discusses the experimental techniques and measurement methods used during the project. The first part of the chapter describes the standard fabrication techniques such as sputtering, photolithography *etc.* The second part of the chapter discusses low current measurements and various electrical systems built during the course of this project.

Chapter 4 discusses the in-situ FIB resistometric technique to measure milled depth and to detect the end point. The reliability of the technique was tested by measuring milled depth with this technique and comparing the data with depth measurements by AFM. The technique was demonstrated for 50 nm wide and 400 nm thick (high aspect ratio cuts).

Chapter 5 discusses the applications of the AFM technique for the measurement of the width of cut and milled depth of nano scale FIB cuts. An investigation was carried out on Si, Nb and an amorphous material, the results from these materials are discussed in this chapter.

Chapter 6 presents an overview of the area of field emission, its applications and fabrication methods. Experimental work follows this general discussion, which was carried out in order to fabricate a lateral field emission device. The experimental work explored various capabilities of the FIB for lateral field emission devices from materials perspective.

Chapter 7 presents the field emission theory, an investigation into different causes of failure of field emission devices and field emission measurements. Successful field emission measurements were performed in UHV and these are discussed in this chapter.

Finally, chapter 8 presents conclusions drawn from the present work and future directions.

1.2 References

1. P. D. Prewett and G. L. R. Mair, (Chapter 1) Focused Ion Beams from Liquid Metal Ion Source, (Research Studies Press, 1991).
2. K. Nikawa, *J. Vac. Sci. Technol. B* **9**, 2566 (1991).
3. R. J. Young, *Vacuum* **44**, 353 (1993).
4. M. T. Abramo and L. L. Hahn, *Microelectron. Reliabi.* **36**, 1775 (1996).
5. J. C. Morgan, *Solid State Technology* 61-73, March (1998).
6. FIB manual for FEI 200 Series system, (1996)
7. K. Gamo, *Microelectronic Engineering* **32**, 159 (1996).
8. G. Smith, G. Davies, and O. Saxl, *Materials World* **8**, 1 (2000).
9. I. Malsch, *Nanotechnology*, **10**, 1 (1999).
10. R. Allan, *Electronic Design*, 100-3 January (1999).
11. K. Tanaka, *Thin Solid Films*, **341**, 120 (1999).
12. S. M. Sze, (Chapter 5) *Semiconductor Sensors*, (John Wiley & Sons 1994).
13. G. Thornell and S. Johansson, *J. Micromech. Microeng.* **8**, 251 (1998).
14. P. Ohlckers, A. Hanneborg, and M. Nese, *J. Micromech. Microeng.* **5**, 47 (1995).
15. C. R. Friedrich, P. J. Coane, and M. J. Vasile, *Microelectronic Engineering* **35**, 367 (1997).
16. M. J. Vasile, C. R. Friedrich, B. Kikkeri, and R. McElhannon, *Precision Engineering* **19**, 180 (1996).
17. H. Lüth, *Phys. Stat. Sol. (b)* **192**, 287 (1995).
18. A. G. Frangoul and K. B. Sundaram, *J. Micromech. Microeng.* **5**, 11 (1995).
19. A. N. Cleland and M. L. Roukes, *Appl. Phys. Lett.* **69**, 2653 (1996).
20. L. Mechin, J. Villegier, and D. Bloyet, *Appl. Phys. Lett.* **70**, 123 (1997).

21. L. Mechin, J. Villegier, P. Langlois, D. Robbs, and D. Bloyet, *Sens. Actuators A* **55**, 19 (1996).
22. G. Ensell, *J. Micromech. Microeng.* **5**, 1 (1995).
23. D. F. Moore, M. I. Lutwyche, N. Fujimaki, and K. Gotoh, *Superconductor Sci. Tech.* **4**, 401 (1991)
24. H. Fujita, *Sens. Actuators A* **56**, 105 (1996).
25. M. Bao and W. Wang, *Sens. Actuators A* **56**, 135 (1996).
26. S. Shoji and M. Esashi, *J. Micromech. Microeng.* **4**, 157 (1994).
27. M. Gretillat, P. Thiebaud, C. Linder, and N. F. Rooij, *J. Micromech. Microeng.* **4**, 156 (1995).
28. W. Fang and J. A. Wickert, *J. Micromech. Microeng.* **5**, 276 (1995).
29. M. Kohl, K. D. Skrobanek, E. Quandt, P. Scholßmacher, A. Schüßler and D. M. Allen, *Journal de Physique IV* **5**, C8-1187 (1995).
30. T. Itoh and T. Suga, *J. Micromech. Microeng.* **5**, 231 (1995).
31. O. Ruiz, J. Samitier, S. Marco, J. R. Morante, C. Burrer, and J. Esteve, *J. Micromech. Microeng.* **6**, 103 (1996).
32. D. F. Moore, J. H. Daniel, and J. F. Walker, *Microelectronics Journal* **28**, 465 (1997).

Chapter 2

Technology, Functions and Applications of FIB

2.1 Introduction

This chapter discusses the FIB technology, functions and applications; the discussion includes technological aspects of liquid metal ion source (LMIS), ion milling function of the FIB and applications such as micromachining. The chapter has three parts, the first part discusses the FIB system technology, the second part discusses various functions of the FIB, and the last part discusses major applications of the FIB technology both in industry and in research.

Ion milling is one of the most important functions of the FIB, it depends on several factors; two very important factors are overlap of collision cascades and re-deposition of sputtered material. End point detection (EPD) technique is another important function of the FIB, it uses the current signal to the ground while ion milling to identify different materials and to measure thickness. This technique is very important for the project as it provided information regarding thickness milled of different layers while fabricating field emission devices and it also led to the calculation of milling rates and sputter yields of different materials. Section 2.3.4 discusses the detailed working principle of EPD with the help of an example. Presently FIB systems applications are mostly in the semiconductor industry, important applications include repair of IC circuits, TEM specimen preparation and defect analysis [1,2]. New applications developing in this field include ion lithography and applications related to micromachining [3-6]. A lateral field emission device was fabricated as part of this project, the section on micromachining discusses the applications of the FIB technology for field emission applications. Section 2.5.2 presents work performed on micromachined structures for example micro-cantilevers.

2.2 FIB System

This project used a FEI 200 series type FIB. Figure 2.1 shows a photograph of the FIB system, which shows the various components of the system, for example the detector, the ion column, and the specimen chamber. The following sub-sections describe the detailed working of the various components of the system.

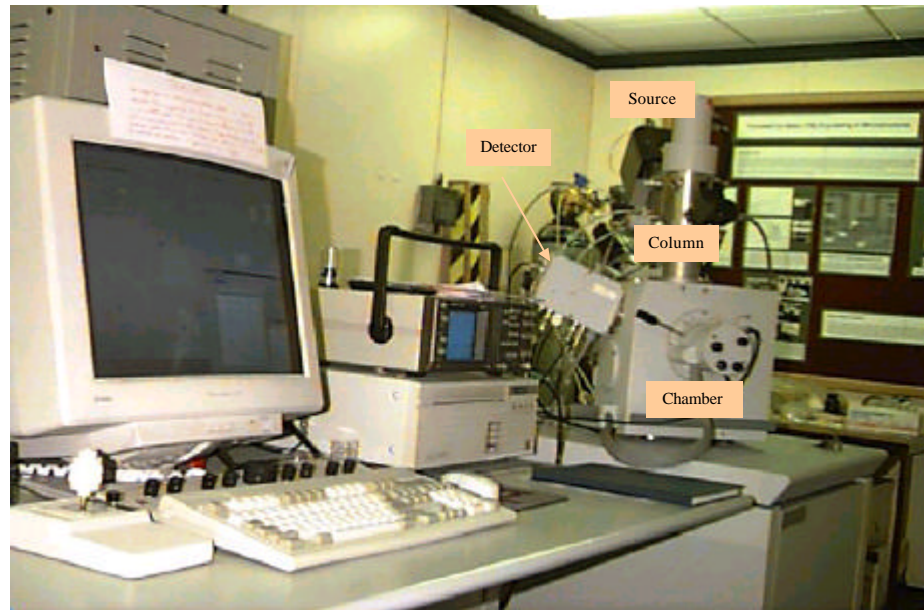


Figure 2.1 FIB system used for this project (FEI 200 series type FIB).

2.2.1 The Column

The column mounts on top of the specimen chamber and consists of a LMIS, two electrostatic lenses, a set of beam blanking plates, a beam acceptance aperture, a beam defining aperture, a steering quadrupole and an octupole deflector. Figure 2.2 shows a schematic of the FIB system.

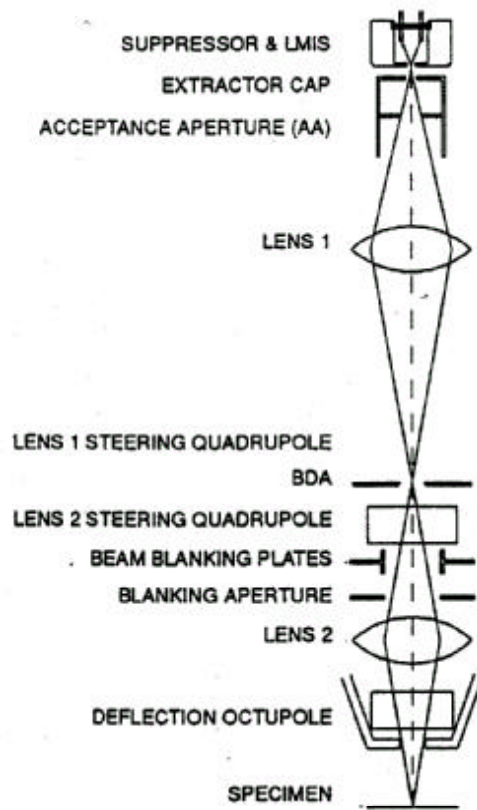


Figure 2.2 Schematic of the FIB system [Source: FIB manual for FEI 200 (1996)].

Application of a negative bias of 30 kV extracts Ca^+ ions from the LMIS and accelerates them towards the specimen. Two electrostatic lenses, a steering quadrupole and an octupole deflector in the column focus the ions into a beam and scan the beam on the specimen. The ion beam strikes the specimen and removes material by physical sputtering process. The striking of the ions onto the specimen also generate secondary ions and secondary electrons, which are detected to form an image of the scanned area. The scan control system allows milling of different patterns. Injection of different gases close to the specimen surface while ion milling results in deposition of different materials and enhanced removal of material [Source: FIB Manual for FEI 200 (1996)]. The following sub-sections describe the various components of the column.

2.2.1.1 Liquid Metal Ion Source (LMIS)

The work on electrohydrodynamic spraying of liquids performed an important role in the development of liquid metals as a source of positive ions. In 1745, Bose reported the phenomenon when he observed the formation of water threads at the nozzle of an electrified capillary [7]. In 1882, Lord Rayleigh made the first calculations on the effects of electric stress on conducting fluids [7]. In early 20th century,

researchers performed different experiments involving liquids such as ethyl alcohol, glycerine, soap bubbles *etc.* It was in 1964 that Taylor, in his classic paper showed theoretically that an uncharged spheroid droplet could exist in equilibrium in a uniform electric field provided:

$$F(r_0/\gamma)^{1/2} < 1.625 \quad (2.1)$$

Where F is a uniform electric field (Vcm^{-1}), γ is the surface tension (dyn/cm) and r_0 is the radius of the droplet (cm).

In mid 1970's the first LMIS was developed and presently there are various types of sources [2]. The LMIS in the FIB used for the project consists of a conical shaped emitter; the source material (Ga) liquefies upon heating. The source material covers the cone and when a strong electric field is applied, the material layer deforms into a Taylor cone. The end of the tiny cone has an end radius of approximately 2nm and ion emission occurs from this end. The half angle of the Taylor cone is determined by the electric field force and the counterbalancing surface tension forces. Ga ion source is commercially used due to its low melting point, low vapour pressure, very high brightness ($10^6 \text{Acm}^{-2}\text{sr}^{-1}$), long life time and high stability variation [Source: FIB Manual for FEI 200 (1996)]. There are various other source materials including Au, Cs, In, Bi, Pb, Ga, *etc.*; a particular application may require a different source material [8]. For example, the fabrication of CoSi_2 microstructure by Co^+ implantation requires a Co source [9].

2.2.1.2 Lens System

The beam from the source first passes through a beam acceptance aperture and then enters Lens 1 (Fig. 2.2). The quadrupole, located just above the beam-defining aperture (BDA) adjusts the beam position so that the beam travels through the centre of BDA. The Lens 2 quadrupole then aligns the beam to the optical axis of Lens 2. The octupole below the Lens 2 provides scan and shift as well as beam astigmatism correction. The beam blanking assembly is located between the Lens 2 steering quadrupole and the second lens assembly. It consists of blanking plates, aperture and an electrical path for the current to be measured. Beam blanking is useful as it protects specimens from constant milling.

2.2.1.3 Stage, Detector and Gas Injection

The stage is motorised and software provides control of X, Y axis and rotation and it can be manually tilted in the XZ plane. Two different type of gases can be released above the specimen surface at a distance of approximately 100 μm , one is used for enhanced etch, the other for Pt deposition. During ion bombardment while milling, charged species form and these are attracted to the detector, which is close to the specimen by applying appropriate bias. The detector is a microchannel plate (MCP), which is a glass array of millions of tiny channel electron multipliers. Figure 2.3 shows a schematic of the stage, ion column and the gas injection needle.

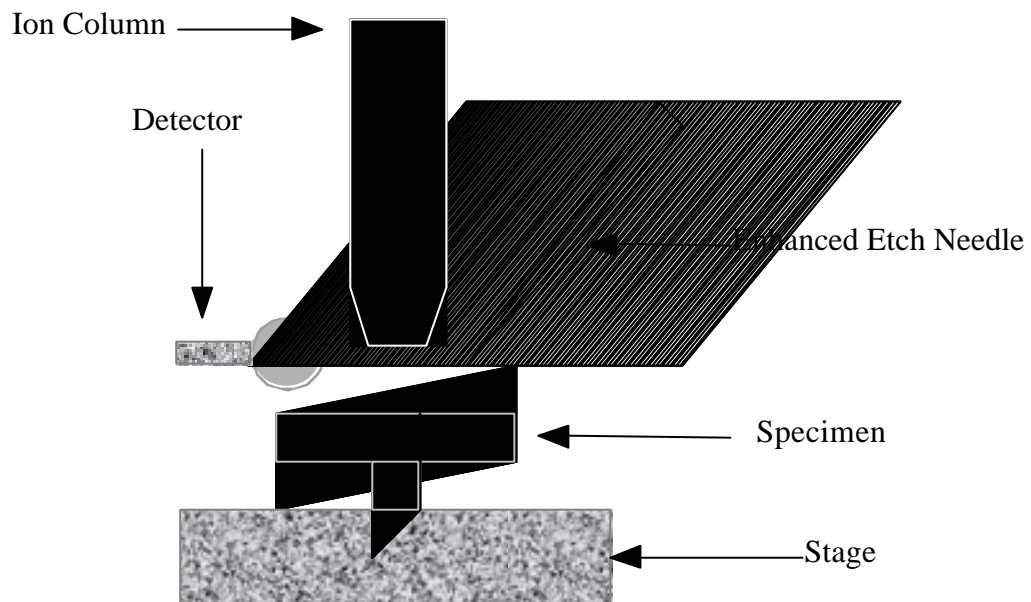


Figure 2.3 Schematic shows the stage, ion column, detector and the gas injection needle.

2.2.1.4 Image Generation

The primary beam is scanned across the specimen as a raster, which consists of a series of lines in the horizontal (X) axis, shifted slightly from one another in the vertical (Y) axis. As the beam scans over the specimen, secondary electrons and secondary ions that are generated by the specimen are detected and the information is stored in the computer; the image is generated from this stored information. The monitor displays the image at TV rate but the information update in the computer occurs only at the beam scan rate. There are three different types of image quality: high (1024 \times 1024 pixel), medium (512 \times 512 pixel) and low (256 \times 256 pixel) [Source: FIB Manual for FEI 200 (1996)].

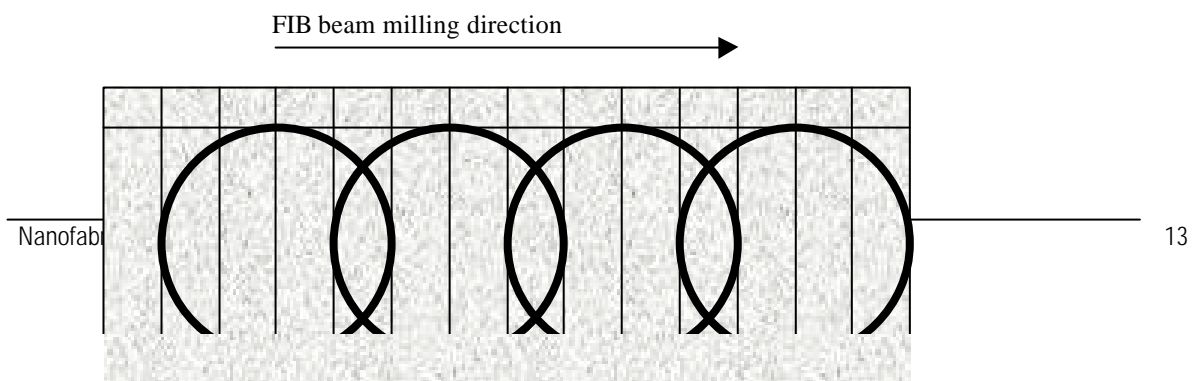
2.2.1.5 Milling

During ion milling the beam is un-blanked and lines, circles, rectangles, polygons with four corners and stepped profiles can be milled using the scan control system. Table 2.1 shows different beam currents and the corresponding milling spot sizes.

Table 2.1 Different beam currents and the corresponding milling spot sizes [Source: FIB manual for FEI 200 (1996)].

Beam current (pA)	Milling spot size (nm)
1	8
4	12
11	15
70	25
150	35
350	55
1000	80
2700	120
6600	270
11500	500

Figure 2.4 shows a diagram of the beam overlap, pixel size and milling spot size. Dwell time is the period of time the beam stays at a particular position. Overlap is defined as the area overlapped when the beam moves from one position to the next and is calculated in terms of percentage of area. The method by which FIB calculates the actual beam overlap is explained in chapter 5, the particular method provides a rough estimate of overlap (it is a simplified method). For milling the pixel size is calculated by measuring the full length of the image observed on the work station divided by 4096, the number 4096 comes from the use of a 12 bit analogue-to-digital card. The milling pixel resolution and milling spot size has to be of appropriate size to define fine features (discussed in detail in chapter 5). The milling conditions for Si material of dwell time of 1 μs and overlap of 50% were used for simple ion milling. Milling conditions with dwell time 0.4 μs and overlap of 0% were used for ion milling with enhanced etch.



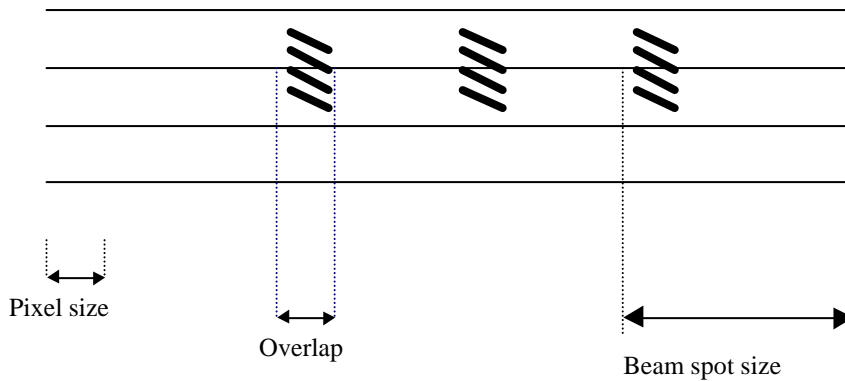


Figure 2.4 Schematic of the beam milling spot size, overlap and the pixel size as the FIB performs milling.

2.3 Functions of the FIB

FIB has various functions, for example, imaging, simple ion milling, ion milling with enhanced etch, Pt deposition and end point detection (EPD). Both secondary electrons and secondary ions can be used to perform imaging. FIB used for this project utilises I_2 gas to enhance the ion milling of different materials. Release of an organo-metallic gas close to the surface while ion milling results in the formation of a Pt deposit. Electrical signal generated while milling through a multi-layered structure can be used to find the end point of a layer. The following sections discuss these different functions of the FIB.

2.3.1 Imaging

Scanning of the ion beam on the specimen surface results in the ejection of electrons and ions. The primary Ga^+ ions scan the surface and penetrate into the surface to depth of 10's of nm, this penetration depth varies from material to material. During ion milling the secondary electron yield is much higher than secondary ion yield, due to this reason FIB is mostly used in the secondary electron mode. Secondary-ion images are of better quality at medium to high probe currents (medium currents include 70 pA and 350 pA, while high beam currents are 1000 pA and above). This arises due to the generation of more secondary ions with these beam currents. At very low beam currents such as 4 pA and 1 pA the images generated by secondary ions are of low quality due to the small amount of secondary ions generated. Images generated by FIB are different from the images formed by SEM, this occurs due the large size of ions relative to the electrons, and due to the positive charge of ions. As the Ga^+ ions are much larger than electrons the interaction volume in FIB is lower than that in SEM; hence secondary electrons and

secondary ions are generated from regions much closer to the specimen surface. Figure 2.5 shows schematically the generation of secondary electrons and ions during FIB milling.

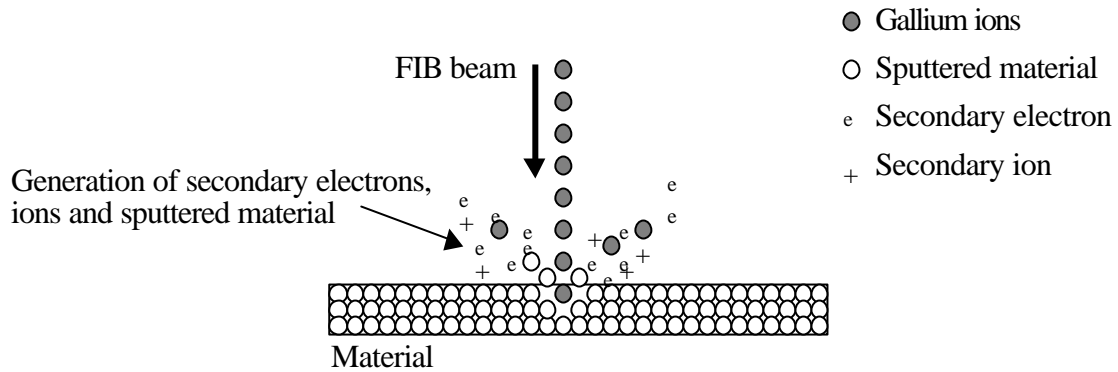


Figure 2.5 Ga^+ ions upon striking the surface of the material generate electrons, ions and sputtered material.

2.3.2 Simple ion Milling and Ion milling with Enhanced Etch

Material removal is performed in the FIB by either physical sputtering or physical sputtering combined with chemicals. The material removal rate in physical sputtering depends on various parameters such as dwell time, overlap *etc.* During the course of the project different materials for example, Al, Cr, SiO_2 *etc.* were used and sputter removal rates were calculated. Release of an appropriate gas close to the surface while performing milling leads to enhanced removal of material. Enhanced removal of material was also performed on various materials and the milling rates were calculated. The following subsections discuss in detail simple ion milling and ion milling with enhanced etch.

2.3.2.1 Simple Ion Milling

The sputter removal rate in FIB depends on the ion flux to the target, the probability that the impact of an incident ion will eject a target atom, the re-deposition of the sputtered material, and the angle of incidence of the ions with the specimen surface. The FIB system used contains material files for sputtering of different materials. In these material data files, beam dwell times and overlap have been calibrated for different material. For a new material, these parameters need adjustment in order to obtain the highest sputtering rate.

Table 2.2 summarises the milling rates of different materials used during the project. The milling rates were calculated by first measuring the thickness of the material

by profilometer and then by observing the milling time in the FIB. The milling time was measured using EPD technique, which is discussed in section 2.3.4. Milled area of size $5\ \mu\text{m} \times 5\ \mu\text{m}$ was used for the calculation of milling rates.

Table 2.2 Milling rates of different materials with simple ion milling.

Material	Simple milling rate($\text{mm}^3\ \text{nA}^{-1}\ \text{s}^{-1}$)
Al	0.37
Cr	0.28
Au	1.8
Si_3N_4	0.21
SiO_2	0.19

Sputter Yield

Table 2.3 shows the sputter yield of different metals used during the course of the project. Sputter yield, S , is the ratio of the number of the target atoms ejected from the target to the number of ions incident on the target. It depends on ion mass, ion energy, target mass, and the crystallinity of the target material. For each target material there exists a threshold energy below which no sputtering occurs. The energy is typically in the range of 10 to 30 eV. Sputtering yield of 2.1 for Si and 5.6 for GaAs at zero degree angle of incidence has been reported [10,11].

Table 2.3 Sputter yields of different metals.

Material	Sputter yield
Al	3.6
Cr	3.7
Au	17

Angular Dependence

The variation in the angle of incidence between the bombarding ions and the surface of the material changes the sputter yield of some materials. The angular dependence of sputter yield is a strong function of the target material and the incident ion

energy. Materials such as Au, Pt and Cu, which have high sputter yields, usually have small angular dependence and maximum sputter yield occurs at $\sim 80^\circ$ incidence angle [12]. Figure 2.6 shows a graph of sputter yield against angle of incidence with respect to target normal. Several authors have reported work on the angular dependence of materials such as Permalloy, diamond, *etc.* [11,13]. The sputter yield of Si and SiO_2 for example increases by a factor of seven to eight times in going from normal incidence to an angle of $75^\circ - 85^\circ$ [11].

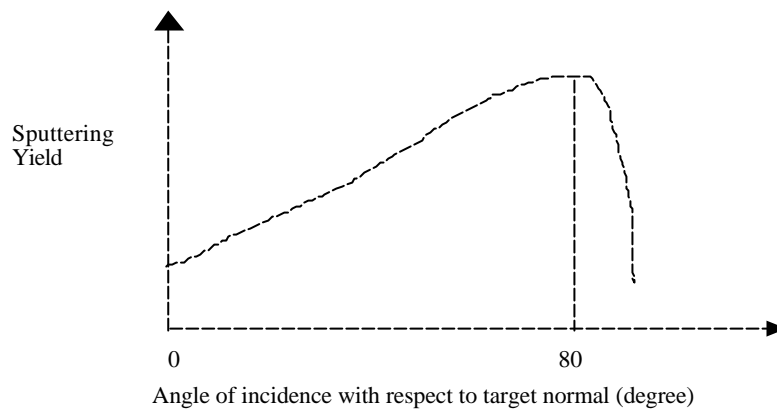


Figure 2.6 A typical variation of materials with pronounced angular dependence on sputter yield.

Re-deposition and Dwell Time

Re-deposition of the sputtered material during normal ion milling in FIB limits the depth of the milled patterns. As the beam mills deeper into the sample, sputtered material is not ejected from the crater but remains within it. Eventually milling stops as the ion beam moves the previously milled material around the crater but does not mill any deeper into the sample. In normal ion milling, it is found that re-deposition on the side wall is controllable by adjusting the FIB scan speed (dwell time) and direction [14-16]. Figure 2.7 shows a small step-like slope, which forms in the bombarded spot during FIB milling. Sputtered atoms are re-deposited more on the side-wall facing the slope having the gradient θ than on the side-wall in the back of the slope. By varying the scan speed, θ and hence sputter re-deposition can be controlled. The adjustment of θ also results in the change in geometrical enhancement factor (angular dependence), so by adjusting the dwell

time different sputtering rates are obtained. Dwell time needs to be optimised for a particular material and a particular application.

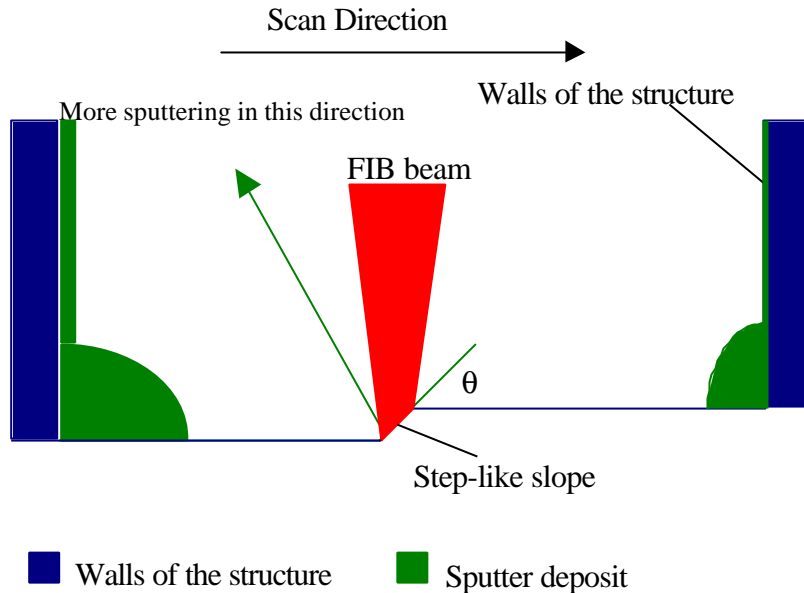


Figure 2.7 Schematic of the FIB milling process at slow speed.

Overlap of collision cascades

Material removal rate can also be changed by varying the overlap of the collision cascades, which occur in the sample material during ion milling. When the ion beam hits the sample surface, collision cascades within the sample take place, resulting in some material sputtered out of the sample surface. Figure 2.8 shows schematic of collision cascades occurring within the material as the beam mills the material. Higher sputtering rate occurs when the collision cascades overlap than when collision cascades does not overlap [7]. This enhancement occurs due to the increase in collision cross-section when the collision cascades overlap. This parameter needs adjustment for a particular material to achieve the highest sputtering rate.

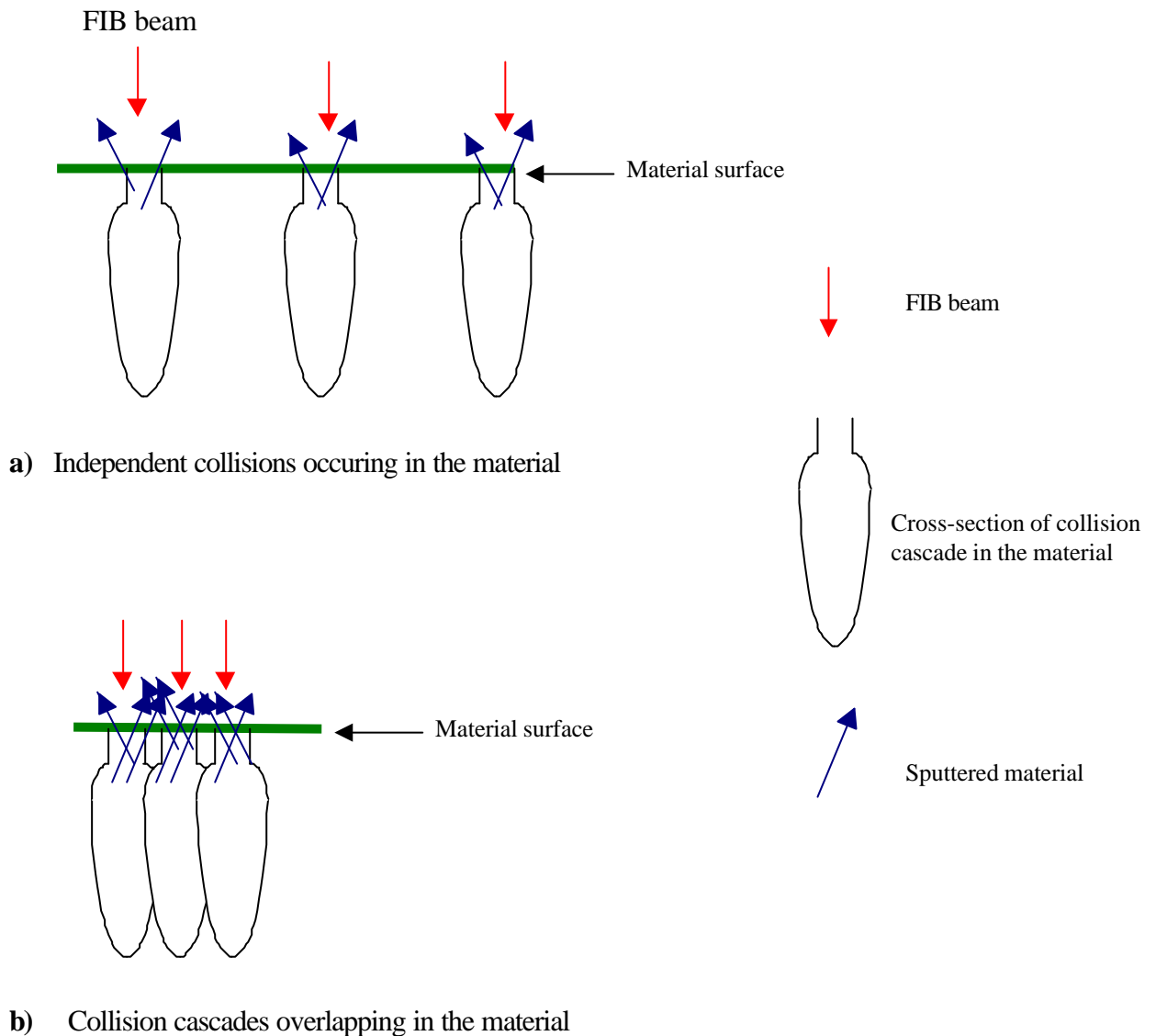


Figure 2.8 Overlapping collision cascades within the material lead to enhancement of milling.

2.3.2.2 Ion Milling with Enhanced Etch

Normal ion beam milling results in the sputtered material re-depositing near the milled area. Re-deposition limits the depth or aspect ratio of the milled patterns, which is defined as the ratio between the depth milled and the shortest dimension of the milling pattern. Gas-assisted etch process removes certain materials faster than normal ion beam milling. The increased etch rate is due to the sputtered material chemically reacting with the assisting gas to form volatile compounds which are removed by the vacuum pump. The

combination of FIB milling and a reactive gas offer a number of advantages over conventional milling:

- increased material removal rates;
- higher removal selectivity among materials and
- absence of re-deposited material.

H₂O, halogen compounds and I₂ have been used as gases for enhanced etching [16-20]. In the FIB system used, enhanced etching is achieved by directing I₂ gas onto the surface of the sample while milling it with ion beam.

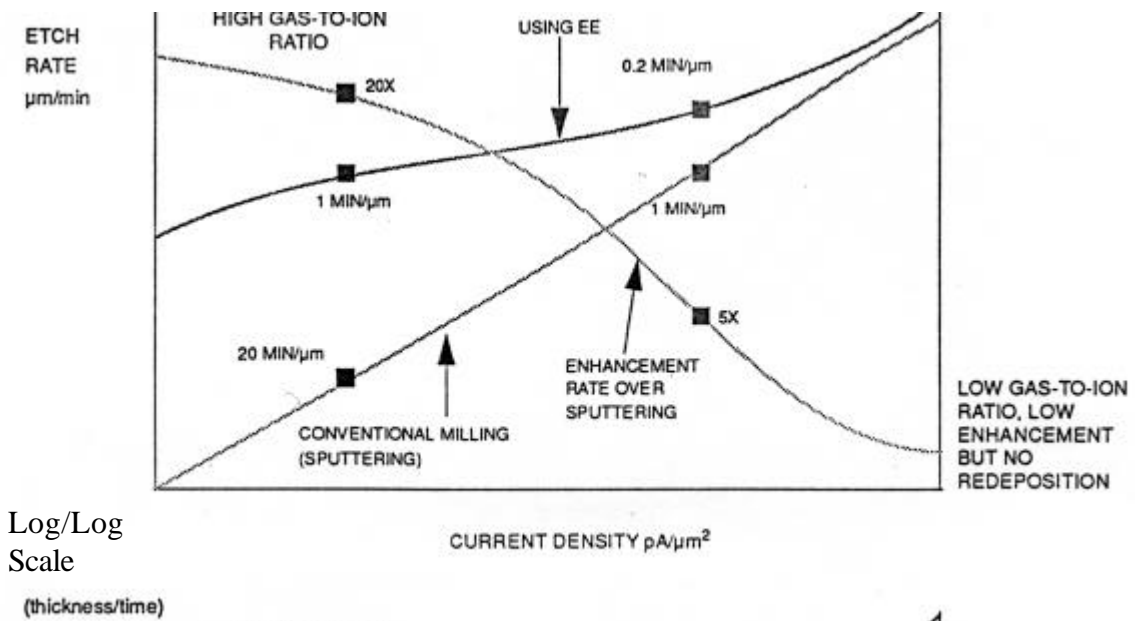


Figure 2.9 Enhancement varies with the gas-to-ion ratio. High gas-to-ion ratio results in higher enhancement [Source: FIB manual for FEI 200 (1996)].

Figure 2.9 shows relationship between etch-rate and current density. Figure 2.9 is only a schematic and its function is to clarify the difference in milling rate, which arises due to the use of enhanced etch and it also helps to clarify the effect of enhancement on gas-to-ion ratio. Conventional milling rate is directly proportional to the ratio of current density to number of ions bombarded on the surface, while enhancement varies with the current density. At low current densities, excess halogen gas is present which ensures that all the sputtered material reacts, thus leading to minimum or no re-deposition. There is insufficient gas present at higher beam current densities to react with all the sputtered material resulting in material re-deposition, which results in low enhancement ratio.

Different materials such as diamond, Permalloy, InP, Si, SiO₂, *etc.* have been milled using ion milling with enhanced etch [13,18,20].

Table 2.4 Milling rates of Al, Cr and Si with simple ion milling and with ion milling using enhanced etch.

Material	Simple milling rate (mm ³ nA ⁻¹ s ⁻¹)	Enhanced etch milling rate (mm ³ nA ⁻¹ s ⁻¹)
Al	0.37	4.1
Cr	0.28	0.48
Si	0.15	0.75-2.25

Table 2.4 shows the milling rates of Al and Cr with simple ion milling and with ion milling with enhanced etch. These two materials were commonly milled with the FIB during the course of the project. The milling time was measured using EPD technique which is discussed in section 2.3.4. The simple milling rate and enhanced etch milling rate for Si in table 2.4 are provided for comparison and are provided in the FIB manual for FEI 200 (1996). The comparison of enhanced etch milling rate shows that Al has the highest milling rate. This can be partly explained by comparing the melting and boiling points of iodides of Al, Cr and Si. Table 2.5 shows the melting (m.p) and boiling points (b.p) of different metal iodides used during this project. AlI₃ has a lower melting and boiling point than Cr iodides, so the enhanced etch rate is higher. The information regarding the melting and boiling points of metals is useful to roughly estimate the milling rate of a particular metal due to the use of enhanced etch. Information regarding the melting and boiling point of iodides in vacuum can improve this rough estimation. Figure 2.10 shows a plot of melting and decomposition points of different iodides. The plot shows that iodides for example Al, Si have low melting points while Cr iodides have high melting points. The plot helps to clarify the information presented in table 2.5.

Table 2.5 Melting and boiling points of iodides of different metals used during this project [Source: Handbook of physics and chemistry (1995)].

Metal	Iodides	m.p (°C)	b.p (°C)
-------	---------	----------	----------

Al	AlI_3	191	360
Cr	CrI_2	856	Sublimes in vacuum at 800
	Cr_2I_3	>600	Without I_2 in vacuum at 350
Ga	GaI_3	212	Sublimes at 345
Au	AuI	Decomposes at 120	
	AuI_3		
Nb			Sublimes in vacuum
Si	SiI_4	120.5	287.5
	Si_2I_6	Decomposes at 250	Decomposes

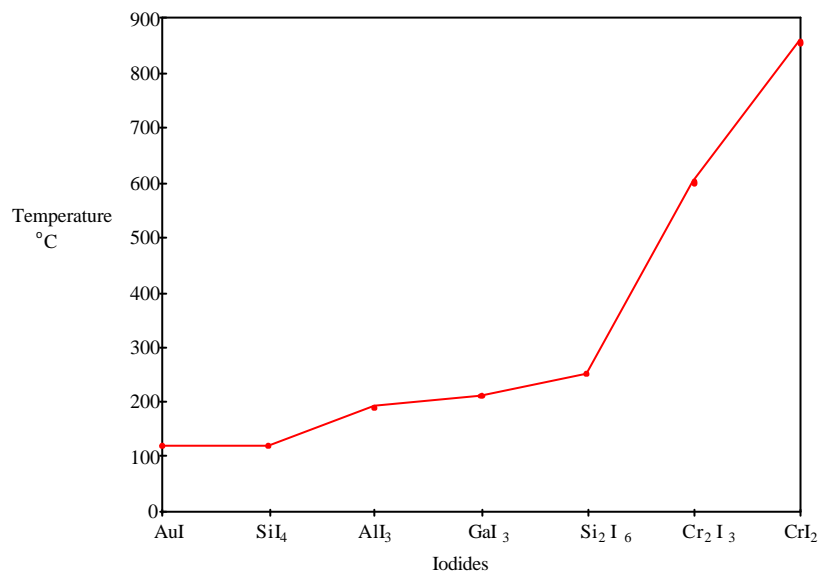


Figure 2.10 Melting and decomposition points of iodides of different metals used during this project

2.3.3 Material Deposition with the FIB

There are two types of FIB deposition: chemical assisted deposition, and direct deposition. Chemical assisted deposition uses chemical reactions between the substrate surface and the molecules adsorbed on the surface. On the other hand, direct deposition uses low energy ions from the source. FIB used for this project is equipped with a Pt deposition facility. The following sections discuss these two methods for depositing materials in the FIB.

2.3.3.1 Chemical Assisted Deposition

The deposition of material using FIB relies upon the delivery of gas molecules to the surface. A gas carrying the element to be deposited is delivered through a capillary nozzle, various gases are used for this purpose [21,22]. Several materials such as W, Pt, Al, Ta, C, SiO₂ can be deposited in the FIB [23-27]. FIB deposition process requires that gas molecules delivered to the surface are adsorbed in adequate numbers and their binding energy to the surface is sufficiently large. Figure 2.11 shows schematically the mechanism of the FIB deposition using adsorbed gas. An incoming ion produces collision cascade effect in the target surface. If the adsorbate binding energy (BE) is less than its decomposition energy (DE), the gas molecules on the surface will be sputtered away and no deposition will occur. Only if the binding energy is sufficiently large compared to the decomposition energy of the molecule that efficient deposition will take place [28]. The precise mechanism by which decomposition of the adsorbate occurs has not been determined. Usually the deposited layer is contaminated by other elements such as oxygen or carbon from the background gas within the vacuum chamber, and by the elements forming the ion beam.

Deposition Rate

Various factors control the deposition rate. One of these, the local gas flux on the sample, is determined for a particular deposition material by the:

- needle position;
- needle diameter and
- crucible temperature

The deposition rate is a combination of the local gas flux and

- beam current;
- scan area and
- scan speed.

Deposition is a delicate balance between decomposing the adsorbed gas to produce a conductive layer and sputtering material from the specimen's surface. The net deposition rate is the deposition rate minus the sputtering rate.

Fast scanning produces fast layer growth over a wide range of ion beam currents and scan areas. With fast scanning, the dwell time at any particular point is short, during

which time the ion beam converts any gas on the surface to a deposited product. Once all gas has been converted, sputtering occurs until the ion beam moves to the next point, the longer the ion beam remains at a particular point, the less net deposition there is [Source: FIB manual for FEI 200 (1996)].

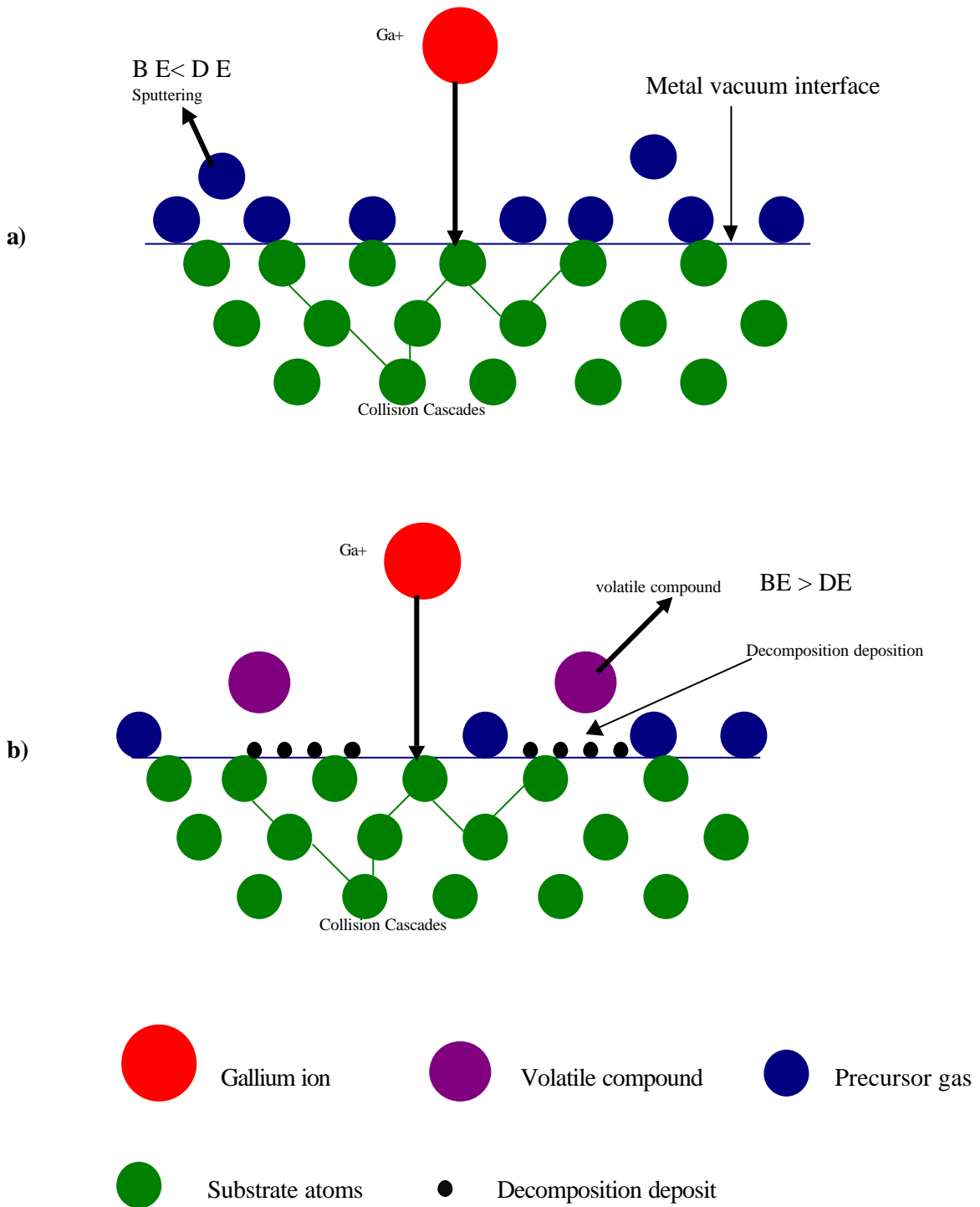


Figure 2.11 Schematic shows mechanism of the FIB deposition using adsorbed gas. **a)** Binding energy is lower than the decomposition energy so the gas atoms sputter away. **b)** Binding energy is higher than the decomposition energy so the gas atoms decompose to leave a deposit.

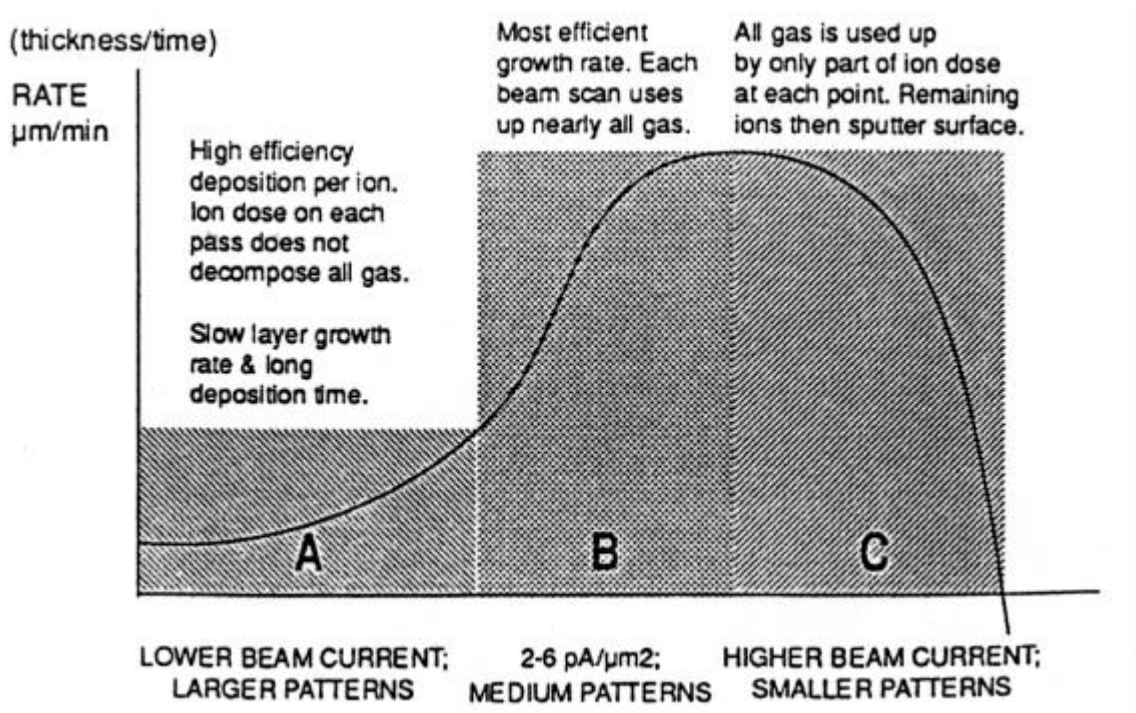


Figure 2.12 Deposition rate of the metal deposit in the FIB varies with the beam current [Source: FIB manual for FEI 200 (1996)].

Figure 2.12 shows the variation of the deposition rate of metal in the FIB with beam current. In area A of figure 2.12 low beam currents are being used, this results in slower growth rate due to the incomplete conversion of the gas on the surface. In area B higher beam current is used, which leads to more gas disassociating on the surface, resulting in higher growth rate. In area C, the beam current is so high that all the gas on the surface is used up and material starts to be sputtered which results in a drop in growth rate.

2.3.3.2 Direct Deposition

In FIB direct deposition, ions are bombarded on the surface with such low accelerating voltages that instead of sputtering the material these ions stick to the surface. Beam energy around 50 eV was used to deposit Au and Ga, the limitation of this method is

its slow deposition rate [2]. FIB direct deposition has several advantages over the FIB gas-assisted deposition one such advantage is that the purity of the deposited film is higher because of the high vacuum conditions maintained during the deposition process. Direct deposition of Au, Cu, Al, Ga, Nb, Nb for superconductive applications and multi-layer structures have been demonstrated [2,29].

2.3.4 End Point Detection (EPD) using Absorbed Current

Absorbed current generated while milling through a multi-layered structure can be used to identify different materials in the structure [30]. The information provided by this method was used in this project to determine the milling time required to mill through different materials. The following paragraphs discuss this method in detail with the aid of a practical example.

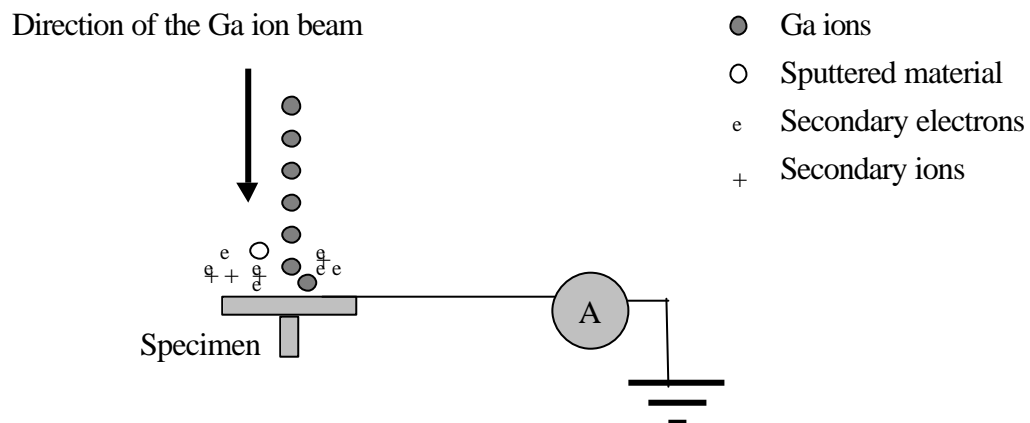


Figure 2.13 Ga^+ ion bombardment generates secondary electrons and ions, which results in a current flowing from the specimen to the ground.

During ion milling, if the specimen is grounded a current flows to the ground which depends on the beam current and on the number of generated secondary electrons and ions. As previously discussed, the number of secondary electrons and ions generated during milling is material dependent. Thus, by monitoring the current flow to the ground (absorbed current), different materials can be identified. Figure 2.13 shows a primary beam of Ga^+ ions hitting the substrate and the generation of secondary ions and electrons. During this process, a current flows to the ground and an ammeter detects it. While milling a multi-layered structure as Ga^+ ions mill through one layer to the next, the current generated

changes thus identifying different materials. EPD works well with conductors, if an insulator is present the information needs to be analysed carefully. In order to find reliable information with EPD, the specimen needs good grounding and a relatively large area needs to be milled. For single pixel line milling, the signal-to-noise level is very high thus making the results unreliable.

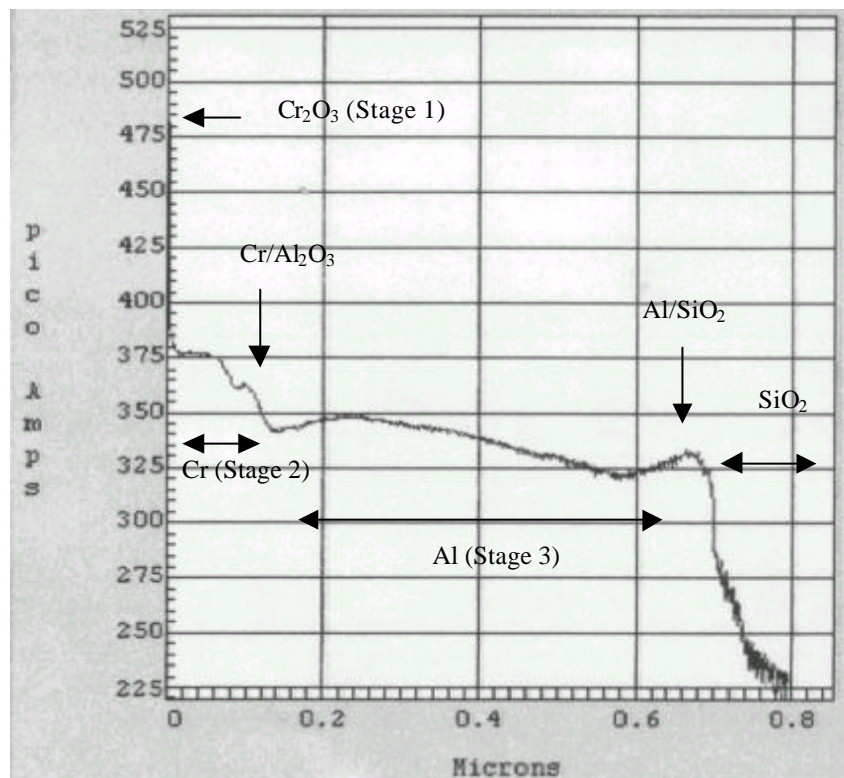


Figure 2.14 EPD graph shows the current signal from different materials. The thickness shown on the graph corresponds to the thickness milled for Si material.

A practical example of a multi-layered structure of Cr and Al deposited on SiO₂ substrate used for the fabrication of field emission devices helps to clarify the method. Si data file was used to mill structures of 5 μm² for EPD. Figure 2.14 shows an EPD graph for this type of structure, the figure is a plot of measured current versus thickness, as the milling conditions used were for Si, the computer analysed the signal as generated by Si. However, the information displayed is useful; by first measuring the thickness of Al and Cr

by profilometer, EPD can be calibrated and then used for these materials. This method was used to determine the milling rates of different materials.

Figure 2.14 shows signal level not only generated by Al and Cr but also by their oxides. There is a thin oxide layer approximately 5-10 nm thick present on both materials, which occurs due to the oxidation of these metal surfaces by atmospheric O_2 . Cr, the first layer to be milled had a grain size of 50 nm, surface roughness of 20 nm and thickness of approximately 250 nm, the grain size and surface roughness were measured using AFM. The milling is divided into different stages and the signal level is considered at each stage to explain figure 2.14. Figure 2.15 shows diagrammatically the milling process and different stages in it. In stage 1, the signal from the oxide above the Cr layer is observed, as milling proceeds this signal mixes with the signal from the Cr material and diminishes. In stage 2 the signal level remains relatively constant as only Cr is milled, a spike in the measured current is observed due to the presence of Al_2O_3 above Al. Non-uniform milling of Cr film due to the presence of grains in the Cr film exposes Al_2O_3 above Al in certain areas thus forming this spike. It was observed by only milling Al and monitoring the EPD signal that the signal level from Al_2O_3 is higher than that from the Al. This signal from the Al_2O_3 interferes with the signal from the Cr until all the Cr is removed. As Al has a lower signal level than Cr a decrease in the signal level is observed as milling continues from the Cr layer to the Al layer. In stage 3 the signal level only occurs due to the milling of Al, which is approximately 900 nm thick. An increase in the current is again observed as milling proceeds from the Al layer to the SiO_2 . However, this increase in signal level is more difficult to explain as the signal from Al (conductor) is mixed with a signal from the oxide (insulator). There are two possible reasons: It could be due to impurities present between the interface that result in this rise in signal level or it could be due to reaction between the SiO_2 and the sputter-deposited Al.

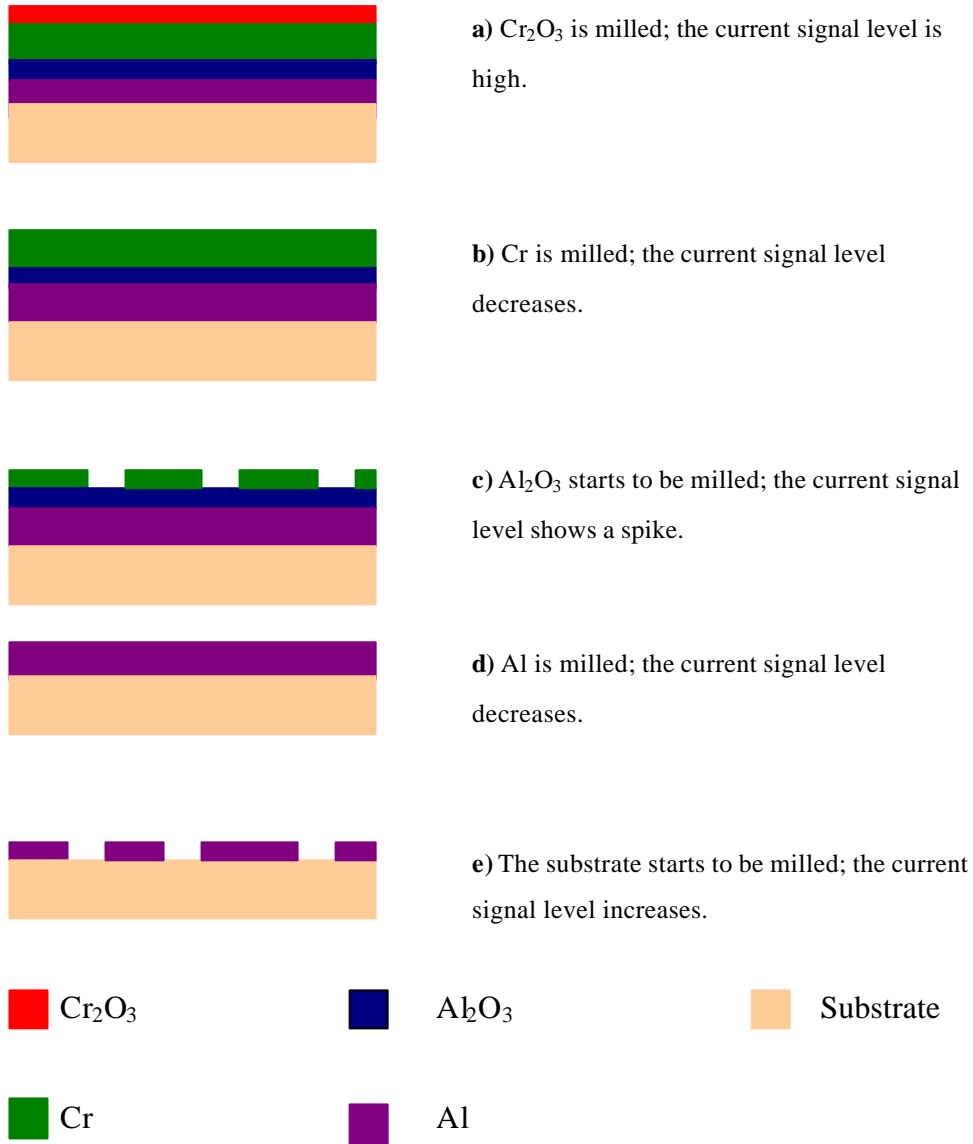


Figure 2.15 Schematic of the different layers of materials removed during the milling of multi-layer structure of Cr/Al/SiO₂. The oxides are approximately 5-10 nm thick, while Cr and Al are 250 nm and 900 nm thick respectively.

From figure 2.14, it is observed that both the oxides have a higher signal level than the corresponding metals and that Cr has a higher signal level than Al, which in turn has a higher signal level than SiO₂. This is due to the different number of charged species produced by different materials, as well as their subsequent escape and charge

neutralisation. It appears to be material dependent and presently there is no theory to predict which material will give a higher or lower signal level.

2.4 *Applications of the FIB*

Presently FIB is mostly used in the semiconductor industry thus major applications are related to the semiconductor industry. Repair of lithographic mask, defect analysis and circuit re-wiring are major industrial applications of the FIB. FIB is also used for TEM specimen fabrication and approximately 100 nm thick sections for TEM can be prepared with this technique. Imaging is a primary function of the FIB and grain contrast is obtained as ions penetrate deeper into some grains of the specimen, this grain contrast is used to measure grain size. The following sections discuss these applications of the FIB technique.

2.4.1 **Repair of Lithographic Masks and Integrated Circuits**

FIB offers a very powerful tool for the removal or addition of material up to an accuracy of 0.1 μm . This is ideal for repairing lithographic masks and integrated circuits where critical dimensions are much less than 1 μm in many processes. The repair of optical lithographic masks was one of the first practical applications of the FIB to be realised. Opaque defects are removed by milling while transparent ones are covered by metal deposition. X-ray lithography is another area where FIB is used for mask repair, transparent defects are repaired by depositing an X-ray absorbing material, for which high-mass atoms such as Pt or Au would be ideal [23,24,33,34]. FIB is also used to repair phase-shift masks, these masks use the shifting of phase of light to form a pattern for lithography [35]. FIB modification of complete devices offers a wide range of possibilities, not only can conductors be cut and re-routed on faulty devices but it is also possible to access buried structures [1,2,28,36-38]. Figure 2.16 illustrates this with an example in which milling provides access to a buried track line, insulator deposition avoids shorting and metal deposition provides electrical connection.

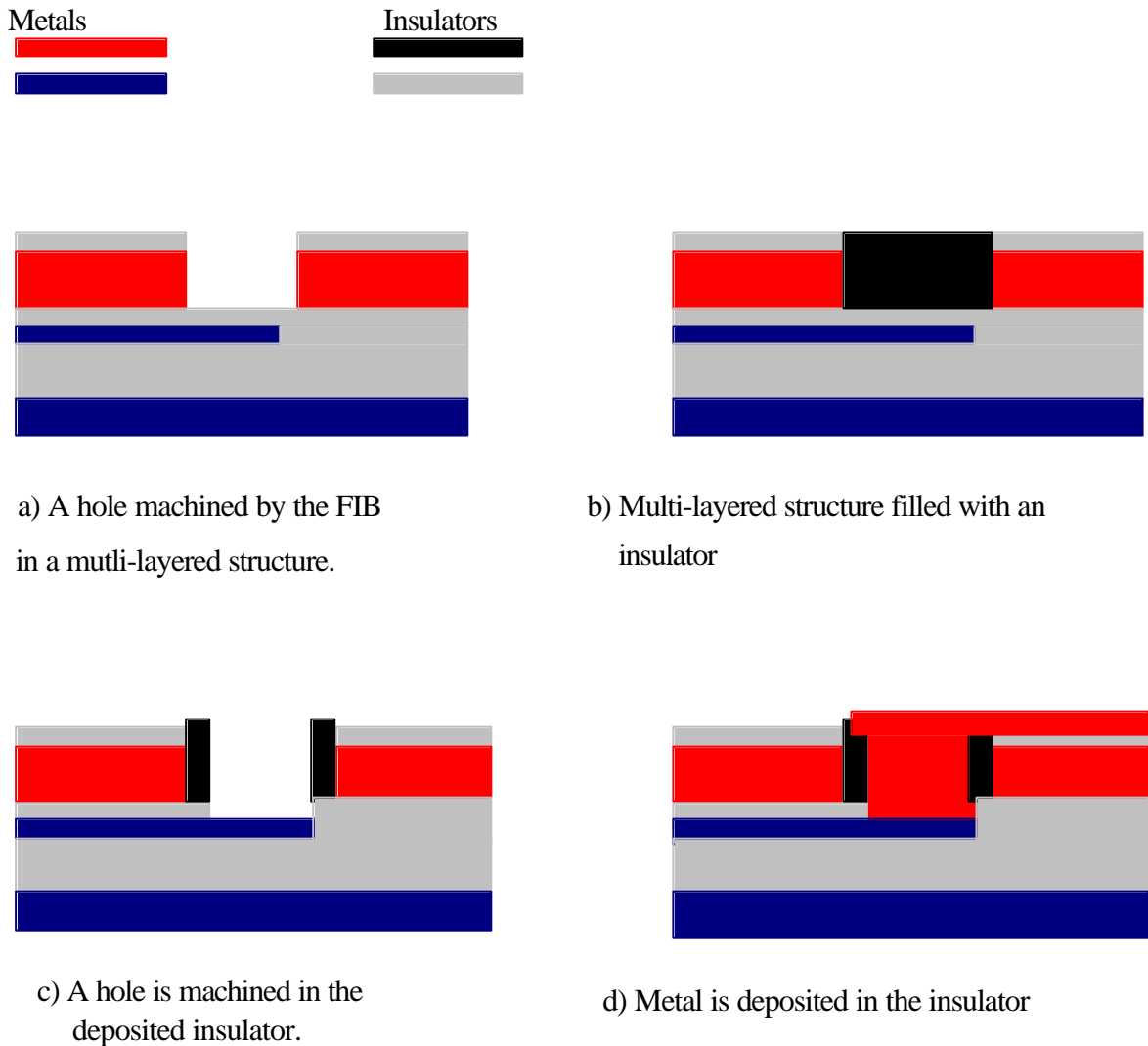


Figure 2.16 Schematic shows a connection to a buried track made using insulator deposition.

2.4.2 Defect Analysis

The ability of the FIB to cut sections in precise positions and imaging is used to analyse defects. This task is usually impossible to perform with conventional methods such as cutting the specimen, polishing and observing with a microscope, while FIB performs this task easily. Other advantages of this technique include:

- A series of sections can be cut to provide 3-dimensional view of a feature.
- Several sections can be cut at different points within an individual device, or across a wafer [1,2,5].

Figure 2.17 shows the most common method, which is to cut and then image cross-sections through semiconductor specimens. During FIB milling, first the defect site is

located then large volume milling (in μm) is performed, next the area under investigation is cleaned. Cleaning is performed step by step by removing lower volumes of material and by using low beam currents such as 11 pA. Figure 2.17 a) shows a sketch of a surface feature under which a suspected defect lies while figure 2.17 b) shows a sketch of a defect after FIB milling and imaging it by tilting the stage.

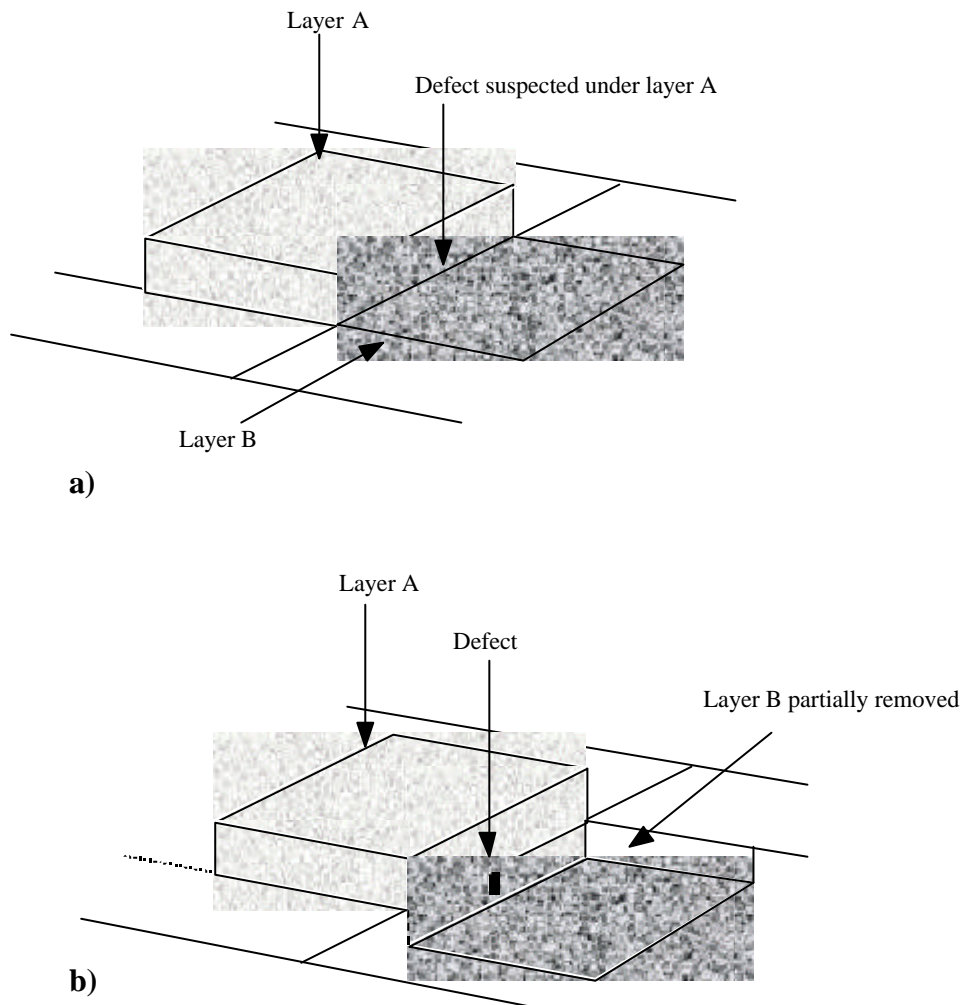


Figure 2.17 Schematic shows FIB machining and imaging for defect analysis. **a)** Defect is suspected under the metal track as shown. **b)** Material is removed and the defect is observed by tilting.

2.4.3 TEM Specimen Preparation

FIB offers the following advantages over conventional ion milling for TEM specimen preparation:

- Specific region with precision of 100 nm range can be milled in the FIB.

- Multi-layered structure, which has different sputtering rates, can be uniformly milled in the FIB.
- Time required for the preparation of a specimen is shorter than conventional Ar ion milling.
- Wide area of up to $10\ \mu\text{m} \times 10\ \mu\text{m}$ can be observed.

The starting point for TEM specimen preparation is a membrane $< 100\ \mu\text{m}$ thick. A Pt pad is deposited on top of the area of interest to protect it from damage while milling. Material is removed from both sides of the region of interest, leaving an electron-transparent slice of approximately $100\ \text{nm}$ thick. The section can then be viewed in the TEM down the milled trench [5]. Figure 2.18 illustrates this by a sketch of a TEM specimen prepared in the FIB. One of the major disadvantages of TEM specimen preparation by the FIB is damage to the material, which can be reduced for certain materials by using enhanced etch [20,39].

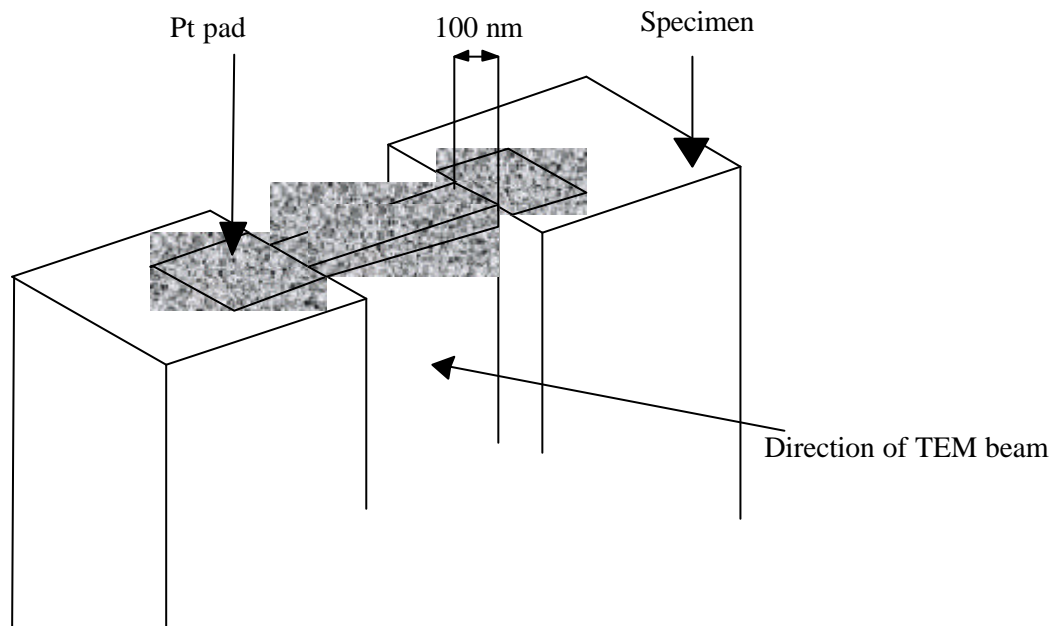


Figure 2.18 Sketch of a TEM specimen prepared using the FIB.

2.4.4 Channelling Contrast

During FIB imaging certain materials show a contrast called channelling contrast, which depends on the grain orientation of the material [1,31]. This occurs due to the penetration of ions to greater depths in certain grain orientation of the material. Figure 2.19

shows schematically that the greater penetration of ions lead to lower secondary electron signal. Figure 2.19 shows two crystallographic orientation of a material, in one orientation ions penetrate deeper than in the other orientation. The shape of the secondary electron generation area is approximate. The grain in which the ions are penetrating deeper generates secondary ions and secondary electrons from a greater depth, thus less signal appears to the surface resulting in darker appearance of the grain [32]. This method can be used to measure grain size.

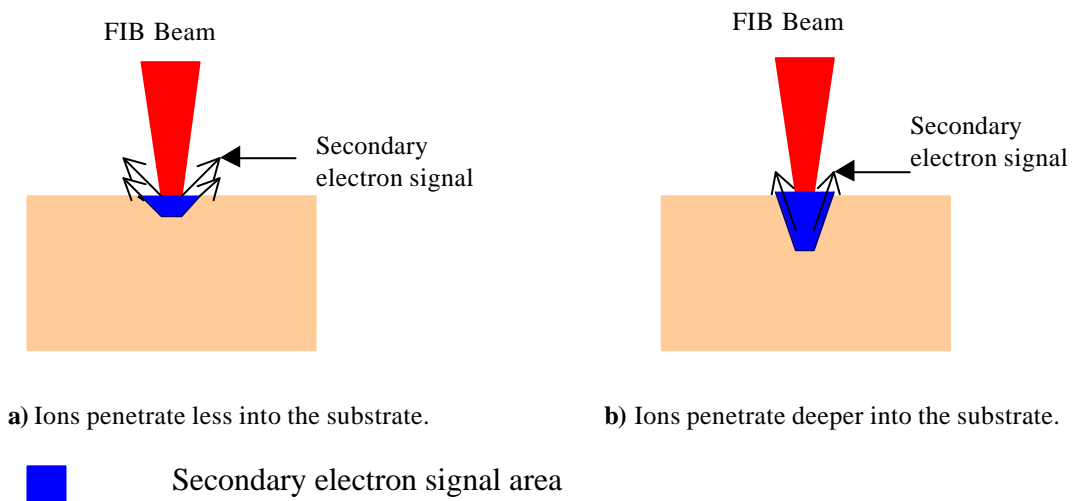


Figure 2.19 Schematic shows FIB beam hitting the substrate surface and generating secondary electron from different depths.

2.5 Ion Lithography, Suspended Structures and Other Applications of the FIB

FIB has been mainly used in the semiconductor industry due to large number of immediate applications. FIB is also used in several other applications including: ion

lithography and doping, fabrication of suspended structures, simple machining of shapes and fabrication of different devices. During the course of the project, FIB applications for the fabrication of micro-cantilevers were explored and trimming of cantilevers was demonstrated. Circular vertical structures with radius approximately 100 nm, useful for field emission devices were also fabricated. The following sections discuss these structures and the various applications of the FIB in detail.

2.5.1 Ion Lithography and Doping

FIB is being presently used as a tool for very high-resolution lithography as ion implantation results in change in the chemical and physical properties of the sample material. Both organic and inorganic resists have been used to form thin walls, arrays of posts and lines. Ladder spin on glass, polymethyl methacrylate (PMMA), Si_3N_4 , Nb, Ti, SiO_2 , AlF_3 , SiC, molybdenum oxide and tungsten oxide have been used to form thin walls, posts and lines [3,4,40-50]. The fine nanometer scale patterns made using this technique have applications in device fabrication. FIB resist exposure is more rapid than FIB direct device etching as resist exposure requires low exposure to the ion beam. For example, spin on glass requires approximately 10^{13} gallium ions/cm² [40] for exposure, which approximately corresponds to exposing 1 μm^2 area with 1 pA beam current for 0.1 s.

Inorganic Resists

Ion bombardment leads to the implantation of ions in thin films which changes the chemistry of these films, in general this requires only low doses. The changes in the chemical properties make it harder or easier for the thin film to etch in a plasma or liquid. The etch resistance of the implanted thin films are thought to arise from the formation of gallium fluorides and gallium oxides during plasma etching using CF_4 or a mixture of CF_4/O_2 plasma [44]. Lines with sub-micron size dimensions have been demonstrated using inorganic resist. One particular application of the FIB inorganic resists is the patterning of high temperature superconductors. High temperature superconductors suffer harmful effects if patterned normally using e-beam lithography and baking [44].

Organic Resists

Exposure of organic resists materials to the FIB leads to scission of organic chain molecules. Dissolution of these exposed regions in alkaline solution results in the fabrication of thin patterns. Ion beam exposure of organic resist material is different from

e-beam exposure due to the difference between ions and electrons. In e-beam exposure, electrons back scatter from the substrate underneath the resist pattern thus exposing a much bigger area than the beam diameter. Due to this reason, FIB lithography has an advantage over e-beam lithography where dense sub-micron patterns are required. Ions are also much more efficient than e-beam for exposing resists due to the large mass of the ions which leads to the ion energy being much more completely absorbed in the resist material. Sub-micron lines and dots have been fabricated using organic resists [4].

Doping

Doping is widely used in the semiconductor industry and is one of the major applications of the FIB. FIB performs doping by implantation. Implantation is the incorporation of the incoming ions into the sample material. As a mask-less process, it offers the possibility of tailoring the band gap of a material by using controlled lateral doping or point defect injection [51,52].

2.5.2 Suspended Structures

Si cantilevers and accelerometer devices have been demonstrated by FIB machining [5,6,53,54]. During this project, FIB was used to perform trimming and fabrication of different shapes of cantilevers. FIB machined the desired shape from a standard shape fabricated with a standard Si micromachining technology. Figure 2.20 shows one such example, in which a rectangular cantilever was trimmed. This type of approach results in several advantages such as it avoids stiction, as thicker sections fabricated with wet Si technology can be trimmed to thin sections with FIB. The method also saves time as it leads to fabrication of a prototype from a standard shape. While trimming cantilevers with the FIB a grainy morphology in the FIB exposed area of the Si_3N_4 film was observed. This observed structure occurs due to the enhanced removal of material from grain boundaries as Si_3N_4 has an acicular structure.

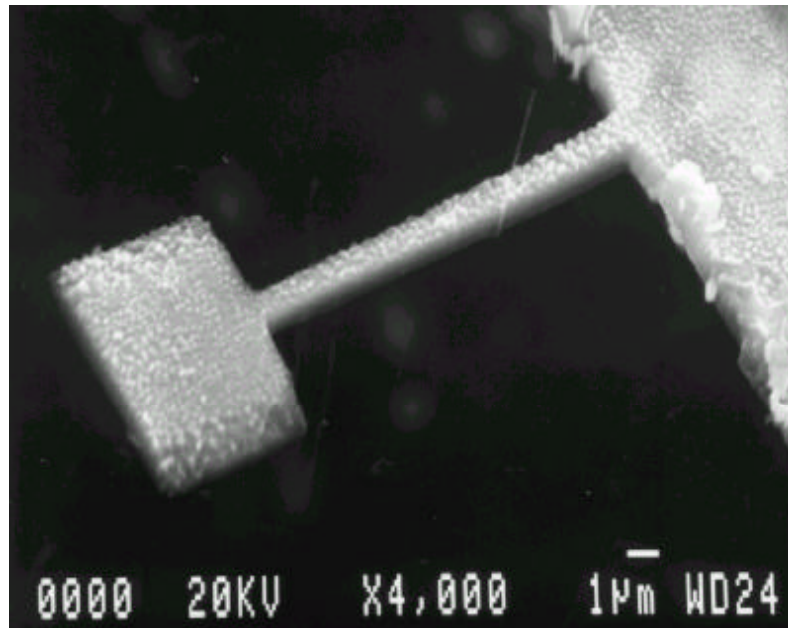


Figure 2.20 SEM photograph of a trimmed Si_3N_4 cantilever, the cantilever was rectangular before trimming. The observed grainy morphology occurred due to the enhanced removal of material along grain boundaries. (Image taken by A. Latif).

Implantation and KOH Etching

Ga implanted Si etches slower than non-implanted Si in KOH solution. This has been combined with the knowledge that etch rate of Si $\langle 111 \rangle$ in KOH is several orders of magnitude lower than that of Si $\langle 100 \rangle$ and Si $\langle 110 \rangle$ to fabricate suspended structures, nano-cups and other 3-dimensional structures [55,56]. The Ga implanted area acts like an etch-resistant mask in this process. The main advantage of the process is that it is maskless.

2.5.3 General Micromachining

General FIB micromachining applications include fabrication of cutting tools, moulds, tips for field ion microscopy, and scanning probe microscopy tips [57,58]. The FIB milling capability has been used to fabricate constricted channels and to mill out holes for field emission device fabrication [59]. FIB metal deposition can be used to fabricate field emission structures, figure 2.21 shows a FIB image of a structure for a possible application as a field emission device. The fabricated structure has a plate-like morphology, this occurs due to shifting of the specimen surface during deposition. This image shift can occur due to vibrations in the FIB system or due to surface of the specimen charging.

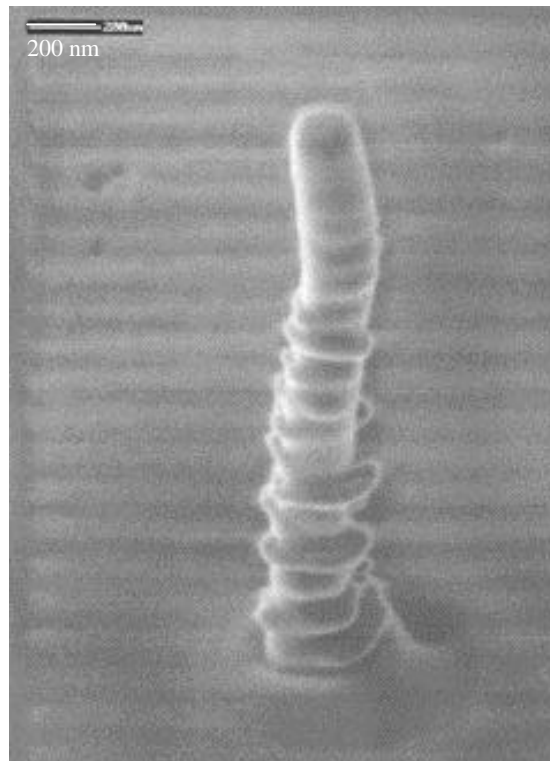


Figure 2.21 A structure deposited using Pt in the FIB. (Image taken by A. Latif).

2.5.4 Device Fabrication

FIB device fabrication includes, field emission, superconductive and tunnelling device fabrication. FIB fabrication results in the fabrication of both lateral and vertical type of field emission devices with a range of materials, chapter 6 discusses this particular aspect of FIB in detail. FIB fabrication leads to fabrication of tunnel sensor, trimming of superconductive devices and fabrication of superconductive tunnel junctions [6,60,61]. FIB is presently not used for mass manufacturing as the FIB technique has low throughput compared to other techniques. This low throughput can be overcome by limiting the FIB processing to certain specialised parts of the structure, or by only producing a small number of prototype or custom devices. Enhanced etch increases etch rate by 10-20 times which makes FIB micromachining more economical.

2.5.5 General FIB applications

This section discusses additional applications of FIB. Thickness measurement with a conventional technique like profilometer provides an estimate of thickness with large error for soft materials. This occurs as a result of profilometer digging into the material and dragging it along the surface. The use of FIB for thickness measurement by milling, tilting and imaging overcomes this difficulty. FIB can also be used for performing

experiments such as isolating different regions of a specimen by milling and then connecting these isolated regions by Pt deposition to measure their properties. FIB technique with controlled focusing opens up the possibility of writing microstructures over a topographic surface profile. This has been demonstrated by forming CoS_2 by Co implantation in Si [62,63].

2.6 Summary

This chapter discussed the FIB technology, its various functions and applications in research and industry. The development of the LMIS led to the birth of the FIB, the research focus has shifted over years from improving the system to developing industrial applications. Different materials were milled using simple ion milling and ion milling with enhanced etch; milling rates and sputter yields of these materials were calculated using the information provided by EPD technique. The EPD technique was explained with the help of ion milling of Cr/Al/SiO₂ heterostructure, this example demonstrated the information provided by this technique. Major applications of the FIB technology include fabrication of TEM specimen, repair of lithographic masks, and defects analysis. Device fabrication with the FIB uses the flexibility and uniqueness of this technique. The ability of the FIB to fabricate structures at nanometer scale makes it a useful tool for nanofabrication. During the course of the project, different structures were fabricated these included fabrication and trimming of cantilevers and deposition of field emission devices.

2.7 References

1. K. Nikawa, *J. Vac. Sci. Technol. B* **9**, 2566 (1991).
2. S. Matsui, and Y. Ochiai, *Nanotechnology* **7**, 247 (1996).
3. H. Lee, S. Paek, and H. Chung, *Jpn. J. Appl. Phys.* **37**, 6792 (1998).
4. S. Matsui, Y. Kojima, Y. Ochiai, and T. Honda, *J. Vac. Sci. Technol. B* **9**, 2622 (1991).
5. R. J. Young, *Vacuum* **44**, 353 (1996).
6. D. F. Moore, J. H. Daniel, and J. F. Walker, *Microelectronics Journal* **28**, 465 (1997).
7. P. D. Prewett and G. L. R. Mair (Chapter 1, & 6), *Focused ion beams from Liquid metal ion source* (John Wiley & Sons, 1991).
8. R. A. D. Mackenzie, *J. Vac. Sci. Technol. B* **9**, 2561 (1991).
9. L. Bischoff and J. Teichert, *Materials Science Forum Vols. 248-249*, pp. 445-450 (1997).
10. B. Khamsehpour and S. T. Davis, *Vacuum* **45**, 1169 (1994).
11. D. Santamore, K. Edinger, J. Orloff, and J. Melngailis, *J. Vac. Sci. Technol. B* **15**, 2346 (1997).

12. S. A. Campbell (Chapter 11), *The Science and Engineering of Microelectronic Fabrication* (Oxford University Press, 1996).
13. P. E. Russell, T. J. Stark, D. P. Griffis, J. R. Phillips, and K. F. Jarausch, *J. Vac. Sci. Technol. B* **16**, 2494 (1998).
14. M. J. Vasile, Z. Niu, R. Nassar, W. Zhang, and S. Liu, *J. Vac. Sci. Technol. B* **15**, 2350 (1997).
15. T. Ishitani, T. Ohnishi, Y. Madokoro, and Y. Kawanami, *J. Vac. Sci. Technol. B* **9**, 2633 (1991).
16. S. Lipp, L. Frey, G. Franz, E. Demm, S. Peterson, and H. Ryssel, *Nuclear Instruments and Methods in Phy. Res. B* **106**, 630 (1995).
17. L. R. Harriot, *Jpn. J. Appl. Phys.* **33**, 7094 (1994).
18. J. Taniguchi, N. Ohno, S. Takeda, I. Miyamoto, and M. Komuro, *J. Vac. Sci. Technol. B* **16**, 2506 (1998).
19. T. J. Stark, G. M. Shedd, J. Vitarelli, D. P. Griffis, and P. E. Russell, *J. Vac. Sci. Technol. B* **13**, 2565 (1995).
20. A. Yamaguchi and T. Nishikawa, *J. Vac. Sci. Technol. B* **13**, 962 (1995).
21. S. Lipp, L. Frey, C. Lehrer, B. Frank, E. Demm, S. Pauthner, and H. Ryssel, *J. Vac. Sci. Technol. B* **14**, 3920 (1996).
22. K. Edinger, J. Melngailis, and J. Orloff, *J. Vac. Sci. Technol. B* **16**, 3311 (1998).
23. H. C. Petzold and P. J. Heard, *J. Vac. Sci. Technol. B* **9**, 2664 (1991).
24. D. K. Stewart, J. A. Morgan, and B. Ward, *J. Vac. Sci. Technol. B* **9**, 2670 (1991).
25. Y. Park, M. Takai, C. Lehrer, L. Frey, and H. Ryssel, *Jpn. J. Appl. Phys.* **37**, 7042 (1998).
26. S. T. Davies and B. Khamsehpour, *Vacuum* **47**, 455 (1996).
27. R. J. Young and J. Poretz, *J. Vac. Sci. Technol. B* **13**, 2576 (1995).
28. P. D. Prewett, *Vacuum* **44**, 345 (1993).
29. S. Nagamachi, M. Ueda, and J. Ishikawa, *J. Vac. Sci. Technol. B* **16**, 2515 (1998).
30. S. T. Davis and B. Khamsehpour, *J. Vac. Sci. Technol. B* **11**, 263 (1993).
31. D. L. Barr and W. L. Brown, *J. Vac. Sci. Technol. B* **13**, 2580 (1995).
32. P. M. Petroff, Y. J. Li, Z. Xu, W. Beinstingl, S. Sasa, and K. Ensslin, *J. Vac. Sci. Technol. B* **9**, 3074 (1991).
33. J. Melngailis, *J. Vac. Sci. Technol. B* **5**, 469 (1987).
34. J. C. Morgan, *Solid State Technology* pp. 61-73 (March 1998).
35. Z. Cui, P. D. Prewett, and J. G. Watson, *J. Vac. Sci. Technol. B* **14**, 3942 (1996).
36. R. V. Camp, K. V. Doorselaer, and I. Clemminck, *Microelectron. Reliab.* **36**, 1787 (1996).
37. S. Lipp, L. Frey, C. Lehrer, E. Demm, S. Pauthner, and H. Ryssel, *Microelectron. Reliab.* **36**, 1779 (1996).
38. M. T. Abramo, and L. L. Hahn, *Microelectron. Reliab.* **36**, 1775 (1996).
39. T. Ishitani, and T. Yaguchi, *Microscopy Research and Technique* **35**, 320 (1996).
40. Y. Koh, T. Goto, J. Yanagisawa, and K. Gamo, *Jpn. J. Appl. Phys.* **31**, 4479 (1992).

41. K. Suzuki, T. Kinoshita, M. Yamashita, N. Kawakami, and A. Nakaue, *J. Vac. Sci. Technol. B* **13**, 2593 (1995).
42. K. Suzuki, M. Yamashita, H. Ueda, and A. Nakaue, *Jpn. J. Appl. Phys.* **33**, 7033 (1994).
43. S. Takahashi, M. Ohashi, S. Fukatsu, Y. Shiraki, and R. Ito, *J. Vac. Sci. Technol. B* **11**, 268 (1993).
44. M. Kusunoki, H. Akaike, A. Fujimaki, and H. Hayakawa, *Jpn. J. Appl. Phys.* **33** part 2, L1124 (1994).
45. J. M. F. Zachariasse and J. F. Walker, *Microelectronic Engineering* **35**, 63 (1997).
46. K. D. Choquette and L. R. Harriot, *Appl. Phys. Lett.* **62**, 3294 (1993).
47. Y. Yamaoka, T. Goto, M. Nakao, S. Kanemaru, and J. Itoh, *Jpn. J. Appl. Phys.* **34** part 1, (1995).
48. J. Gierak, C. Vieu, H. Launois, G. B. Assayag and A. Septier, *Appl. Phys. Lett.* **70**, 2049 (1997).
49. R. Menzel, T. Bachman, W. Wesch, and H. Hobert, *J. Vac. Sci. Technol. B* **16**, 540 (1998).
50. M. Hashimoto, S. Watanuki, S. Koshida, M. Komuro, and N. Atodu, *Jpn. J. Appl. Phys.* **35** part 1, 3665 (1996).
51. K. Gamo, *Microelectronic Engineering* **32**, 159 (1996).
52. C. Crell, H. U. Schreiber, and A. D. Wieck, *Microelectronic Engineering* **41**, 253 (1998).
53. J. H. Daniel, D. F. Moore, J. F. Walker, and J. T. Whitney, *Microelectronic Engineering* **41**, 432 (1998).
54. J. McCarthy, Z. Pei, M. Becker, and D. Atteridge, *Thin Solid Films* **358**, 146 (2000).
55. B. Schmidt, L. Bischoff, and J. Teichert, *Sensors and Actuators A* **61**, 369 (1997).
56. J. Brugger, G. Beljakovic, M. Despont, N. F. de Rooij, and P. Vettiger, *Microelectronic Engineering* **35**, 401 (1997).
57. M. J. Vasile, R. Nassar, and J. Xie, *J. Vac. Sci. Technol. B* **16**, 2499 (1998).
58. M.J. Vasile, C.R. Friedrich, B. Kikkeri, and R. McElhannon, *Precision Engineering* **19**, 180 (1996).
59. G. Thornell, and S. Johansson, *J. Micromech. Microeng.* **8**, 251 (1998).
60. R. W. Moseley, W. E. Booij, E. J. Tarte, and M. G. Blamire, *Appl. Phys. Lett.* **75**, 262 (1999).
61. F. P. Stratton, R. L. Kubena, H. H. McNulty, R. J. Joyce, and J. Vajo, *J. Vac. Sci. Technol. B* **16**, 2449 (1998).
62. L. Bischoff, E. Hesse, D. Panknin, W. Skorupa, and J. Teichert, *Microelectronic Engineering* **23**, 115 (1994).
63. L. Bischoff, J. Teichert, and E. Hesse, *Microelectronic Engineering* **27**, 351 (1995).

Chapter 3

Experimental Fabrication and Measurement Methods

3.1 Introduction

Specimen fabrication and measurement work consisted of the development and testing of a new lateral field emission device, development of a new in-situ FIB measurement technique and specimen preparation for AFM measurements of FIB milled structures. Device fabrication started by dicing the substrate into millimetre size chips. Different fabrication steps such as FIB processing, photolithography, sputtering, and KOH dissolution *etc.* led to the required structure. After fabrication, the device was wire bonded to an IC (Integrated circuit) board for electrical measurements. An investigation with SEM on field emission devices helped to measure the sharpness of the devices and to understand their operation. Electrical measurements performed on these devices included field emission measurements in UHV and high vacuum (HV). Field emission measurements were performed in the low current range (picoampere range) in UHV and HV, which required building of low current measurement systems. A number of precautions were taken in order to perform the measurements such as minimising leakage current, shielding of wires *etc.* An in-situ FIB electrical measurement system was developed as it can be used to perform unique experiments involving FIB milling and electric currents. This development work involved experimenting with different designs and materials. The present project employed this technique for applications such as thickness measurement at nanometer scale, low current measurements and heating of chips. This chapter consists of two major parts: specimen fabrication techniques and measurement methods. Specimen fabrication techniques part includes: methods for fabricating devices and methods such as specimen fabrication for advanced SEM. Measurement methods part of the chapter covers the different electrical measurement and systems used for this project for example low current measurements.

3.2 Specimen Fabrication

Specimen fabrication started with the selection of a suitable substrate and then cutting using a wafer dicing saw. Various substrates were used for example Si, silica (SiO₂), Si coated with Si₃N₄ *etc.* Specimen were commonly cut into sizes of 7.5 mm × 10.5 mm. Wafer dicing left a wax deposit on the surface, which was removed by a two-step cleaning process involving: acetone cleaning with ultra-sonic for 20 minutes and cleaning with chloroform for 24 hrs. Field emission device fabrication required thermal oxidation of Si substrate before any further processing. These devices also required sputter deposition of Al, photolithography, sputter deposition of Cr, FIB processing and chemical dissolution. New methods were experimented to overcome major difficulties in the field of field emission such as poisoning and arcing. The sharpening and arcing of field emission devices was studied by imaging in advanced SEM. The following sections discuss the different fabrication steps involved both in field emission device fabrication and for other processing; FIB processing involved in field emission device fabrication is separately discussed in chapter 6.

3.2.1 Thermal Oxidation

Dry thermal oxidation was used to form an insulating layer of SiO₂ on top of the Si substrates for the fabrication of field emission devices. The type of oxide is called fused silica, and it is amorphous. Thermal oxidation avoids any pinhole formation, which usually occurs in the sputtered films of SiO₂ and hence is an effective method for fabricating a good quality insulator on Si [1]. After some initial experimentation, this processing step was not used further, as the furnace needed for this processing step should be very clean. The furnace used for this step were designed for bulk processing of superconductors, fine dust particles on the surface of the Si chips were interfering with the growth of SiO₂ film, which resulted in poor quality of photolithography. The film thickness was predicted using Deal-Grove model, as it was thicker than 30 nm [1]. Thickness grown was verified by milling, tilting and imaging in the FIB. Equation (3.1) gives the chemical equation for the reaction.



3.2.2 Sputter Deposition

Sputtering is one of the main techniques for metal deposition used in microelectronics fabrication [1]. Sputtering has several advantages over metal deposition techniques like evaporation such as better step coverage, and can easily deposit layers of compound materials and alloys. Magnetron sputtering process was mainly used to deposit Al and Cr, some other materials such as Au, Ni, and Fe were also deposited during the project. The following paragraphs discuss sputtering, difficulties encountered and the processing conditions.

During sputtering when ions strike the surface of the material, four different events may occur. Ions with very low energy may simply bounce off. At energies of less than 10 eV, the ions may also adsorb on the surface, releasing their energy as heat. At energies above 10 keV, the ions penetrate deep into the target material for example several atomic layers spacing, dissipating most of their energy inside the target material and changing the physical structure. Between these two extremes, both energy transfer mechanisms happen. Part of the energy is absorbed as heat and the remainder goes into the physical rearrangement of the

substrate. When this happens, target atoms are ejected from the surface. These ejected atoms travel from the target surface to the chip surface after undergoing numerous collisions with the plasma species. The sputtered film is composed of these ejected atoms from the target. The stress in the film and the adhesion to the surface can be controlled by varying the pressure of the gas during sputtering, and by providing thermal energy to the chip surface. These two variables change the mobility of the sputtered atoms and their impact energy.

Two of the major difficulties encountered due to sputtering were blistering of the deposited film and the low adhesion of the thin film to the chip surface. Blistering of the deposited film resulted in destroying some specimens but it was not as severe as peeling-off the film due to low adhesion. Adhesion to the surface of the chip posed considerable difficulties, as it was observed in two cases: deposition of Al on SiO₂ substrate and the deposition of Au on Al. In the case of Al on the SiO₂ substrate, the film was being removed in the cleaning step. As Al film was essential for the particular fabrication scheme, the cleaning process, which used to involve ultra-sonic cleaning, was modified and specimens were cleaned individually with airgun and acetone. In the case of Au deposition on Al film, due to the presence of Al₂O₃ on the surface of Al the Au film adhered badly to the surface. This could not be addressed easily and hence Au deposition was discontinued.

Table 3.1 provides the deposition conditions used for depositing Cr and Al; Ar gas carried out sputtering. Prior to deposition, the sputtering chamber was allowed to pump overnight for at least 9 hours. A bake out procedure was also carried out for four hours at 120°C. No bake-out was performed for specimens with photoresist on them. The final base pressure was of the order of 10⁻⁸ mbar.

Table 3.1 Deposition conditions used for Cr & Al.

Material	Sputtering gas pressure (Pa)	Power (W)	Target to specimen distance (mm)	Deposition rate (nm/min)
Cr	0.58	2.9	41	25
Al	0.53	3.0	50	15

3.2.3 Photolithography

Photolithography was performed in the clean room by two types of processing: one involving simple photolithography, the other involving an additional step (liftoff process) to improve the roughness of the edge of the film deposited after photolithography [1]. Photolithography was performed by using two different systems: a canon mask projection system, which has a resolution of approximately 2-3 μm and a contact mask aligner (Karl-Suss machine), which has a resolution of approximately 1 μm. The following paragraphs discuss the different machines and the processing types used.

The mask projection system works by focusing an image of the mask onto the specimen and then exposing it, in this particular case the distance between the mask and the specimen is large. On the other hand, the contact exposure system works by bringing the specimen into contact with the mask and then exposing. Two different photoresists were used, microposit 51813 and Hoechst AZ 1529, with the latter being commonly used. The length of time and the speed of rotation at which the substrate and the photoresist

layer is spun, determine the thickness of the photoresist layer. Photoresist was spun at a speed of 6000 rpm for 30 seconds and then baked for 1 minute at 100°C. A standard exposure time of 30 seconds was used in the case of mask projection system. After exposure, the resist was developed using the commercially available developers until a fine pattern was formed.

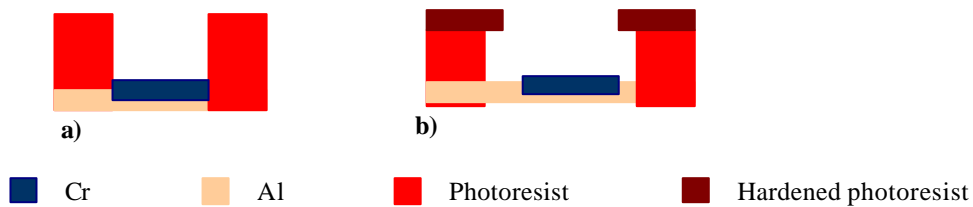


Figure 3.1 Schematic shows a metal deposit of Cr on Al **a)** after common lithography and **b)** after lithography with the liftoff process.

Figure 3.1 shows the liftoff process, which was required for the processing of field emission devices [1]. Appendix 1 shows the photolithographic mask used for patterning Cr lines on Al film deposited on insulating substrates. A simple processing method could have been to sputter Al, then perform lithographic processing and then deposit Cr on the substrate and afterwards remove the photoresist to leave Cr pattern on Al. This type of processing results in poor definition of the metal tracks as the removal of the photoresist, which is in direct contact with the metal deposit, roughens the edge of the metal track. To avoid this roughening of edges the liftoff process was utilised, in this process application of chlorobenzene hardens the surface of the photoresist after spinning. Hardening results in the formation of a ledge on the surface of the photoresist during development. Due to the presence of this ledge, the edge of the deposited metal track does not come into direct contact with the photoresist. This results in better definition of the metal deposit. The chips were soaked in chlorobenzene solution for one minute and then standard photolithographic processing was used. For the removal of the photoresist after Cr deposition, the chips were cleaned with acetone in an ultrasonic bath for approximately ten minutes. On occasions, ultrasonic cleaning was avoided as it resulted in the stripping of the metal film off the substrate.

3.2.4 Al Dissolution, Advanced SEM Specimen Preparation and Other Methods

Field emission device processing required FIB fabrication after processing using thermal oxidation, photolithography, and sputter deposition. FIB fabrication defined the shape and different other parameters of the devices. The deposited Al was partially dissolved to isolate the anode from the cathode. After Al dissolution several specimens were examined in an advanced SEM for the measurement of the sharpness of field emission devices. Some other methods were also experimented after partially dissolving

Al, however these methods were not commonly used in the fabrication scheme, these other methods included chemical displacement and anodization. For electrical measurements, wirebonding provided electrical connections from the chip to the specimen holder for measurements. Wire bonds were first made to the Cu pads on the printed circuit board (specimen holder) and then to the pads on the chip with thin Al wires of diameter 25 μm .

3.2.4.1 Al Dissolution

Dissolution of Al was required during the processing of field emission device. Chemical etching was used to dissolve Al, a weak solution of KOH (0.11 M) was used for this purpose, which approximately corresponds to 0.1 g of KOH in 15 ml of de-ionized water. For this processing it was required to know the colours of different materials and the colours of different substrates. Al was deposited on different substrates for example Si_3N_4 (green), SiO_2 thermally grown on Si (blue to green) and silica (colourless). Cr film was deposited via a photolithography mask on the Al film and afterwards the mask was dissolved to leave Cr pattern on the deposited Al. After FIB processing (discussed in chapter 6) the Al film was partially dissolved in KOH solution. Al dissolution was stopped by putting the chip into a beaker of water, it was done when Al film could not be observed on the surface. This observation was simple to perform because as the substrate surface below the Al film was exposed a colour change was observed, which depended on the type of the substrate.

This was one of the last processing steps and every necessary precaution was taken to make it successful. Fresh KOH solution was prepared every time and continuous stirring of the solution counteracted any local variations in the concentration of the solution and removed any bubbles formed on the chip. Dissolution rate of Al in this solution is approximately 40 nm/minute. At times, this processing step was not successful due to factors such as blistering of the sputtered film *etc.*

3.2.4.2 Advanced SEM Specimen Preparation

Two types of SEM's were used during the course of the project, a standard JEOL 820 SEM with a W filament as source of electrons (thermionic emission), and an advanced SEM with a field emission gun as source of electrons (FEG SEM). FEG SEM requires special specimen cleaning and additional difficulties occurred during imaging due to the insulating substrates. Au sputtering is commonly used to coat insulating

specimens to form a conducting path to ground for imaging in SEM. However, Au sputter deposition could not be used as it is not of high enough quality for this particular application. Either a sputtered Cr or evaporated C coating is used for this particular machine, Cr coating can only be used for imaging once as an insulating oxide grows on Cr, thus evaporated carbon coating was used. C evaporation at an angle led to a continuous electrical path, as overhanging structures were present in the specimen. After C deposition, any organic deposit left due to the cleaning process, which involved cleaning with acetone, is removed by cleaning the specimens in O₂ plasma. All this care needed to be taken as decomposition of organic molecules under the electron beam forms different types of gases which adsorb inside the SEM chamber and over time result in poor performance of the microscope.

3.2.4.3 Metal Deposition by Chemical Displacement and Other Methods

Partial Al dissolution from the chip completed the fabrication of field emission devices. Further fabrication processing steps were experimented to improve the field emission properties of the devices. The area of field emission encounters two major difficulties: poisoning and arcing of the devices (Chapter 7 describes both in detail). Different methods were experimented to overcome these difficulties, most of the steps discussed in the following sections are new to the area of field emission.

Chemical Displacement

A chemical displacement reaction was used to coat field emission devices with a different metal, which is less electronegative than the metals used for the fabrication of field emission devices. Cu was selected over other metals, as it is an excellent thermal conductor, this factor is important as better heat conduction away from the field emission tip should result in improvement in device performance.

Copper nitrate solution was used as a starting precursor which results in the formation of Al and Cr salts during the chemical displacement reaction, these salts are nitrates and thus soluble in water [Source: Handbook of physics and chemistry (1995)]. Both Cr and Al react with O₂ to form protective oxides on the surface. These protective oxides can stop any coating of Cu on the surfaces of these metals, which occurs due to the displacement reaction. This could be a major problem for this type of processing. Thus, following steps were performed immediately after chemical dissolution of Al as an attempt to minimise this problem. After removal of the chips from the KOH solution, the immersion of the chips into a beaker of water ceased the

reaction to form oxides and it also cleaned the chips. The chips were then immersed into a beaker of copper nitrate solution, which resulted in the formation of Cu coating. During the transfer of chips from beaker to beaker, the top surfaces of the chips were kept wet and the processing was performed very quickly. However even after these extra precautions the Cu coating provided inconsistent results. The coating deposited on the surface of the Cr film was μm 's in size and spherical in shape.

O₂ Plasma Cleaning & Ar Ion Milling

Plasma cleaning using O₂ plasma was performed during specimen preparation for SEM examination. It was also used to clean the surface of field emission devices to remove any possible organic deposit left due to the cleaning step, which involved organic solvents. Plasma cleaning involves the formation of reactive O₂ plasma, which reacts with organic deposits on the surface. These organic deposits form carbonic gases, which are pumped out of the plasma cleaning system [3].

Ar ion milling was also used during the course of this project. Ar ions are generated by first forming an Ar ion plasma which is then accelerated towards the specimen surface, Ar ions upon striking the chip surface sputters the film [1]. This processing step was used a few times to remove any impurities left on the chip surface from previous processing or handling steps.

Anodization

This step was performed after partial chemical dissolution of Al. After the chemical dissolution, some Al remained on the surface of the chip, this Al supports the Cr wires. It was attempted to coat this Al with an oxide layer by anodization. However, this could not be achieved since upon the application of current, Cr dissolved in the borate solution used for anodization. This step may work for field emission devices fabricated with other metals such as Au/Cu thus possibly improving their emission properties.

3.3 Measurement Systems and Methods

Different types of electrical measurements were performed during the course of the project. A low current measurement system was built for performing field emission tests in UHV. An in-situ FIB electrical measurement system was built in order to perform experiments involving FIB milling and electrical currents. Measurements performed in this system included four-point resistance measurements, field emission measurements and field emission measurements with heating. The following sections first discuss field emission measurements then field emission measurement system for UHV and then in-situ FIB measurement system and different measurements performed in it.

3.3.1 Low Level Current Measurements

Lateral field emission devices were tested both in UHV and inside the FIB (high vacuum). The devices operated in the picoampere range (low level current measurements). Errors in low level current measurements can arise due to various factors such as leakage currents in the measurement system, different environmental factors, integrity of the device connections and bad rig design [4,5]. Good knowledge and understanding of these sources of errors is required in order to build a useful low current measurement system. The following paragraphs discuss the possible sources of errors and remedies.

Leakage Currents

Leakage currents are generated by high resistance paths between the measurement circuit and the nearby voltage source. In the present case, the main source of possible leakage current was the IC board. Moisture absorbed in the IC board or any material deposit on it were possible causes of leakage current. This was avoided by keeping the IC board in a dessicator and by thorough cleaning of the IC board. General methods to reduce leakage currents are to use good quality insulators, reduce humidity, and use guarding. These methods reduce the possibility of high resistance paths, thus leading to better measurements.

Device Connections

Although instrument accuracy is of great importance when performing low-level measurements, the integrity of the device connections is equally important. The integrity of the device connections means that they are properly clean, they are not adding in any way to the measured current and they are properly guarded. Increased number of device connections result in increased noise in observations, and these should be minimised. The complete signal path from connectors through the cables and into the test fixture must degrade the measured signal as little as possible. Digital multimeters often use paired banana leads, such connection schemes are generally inadequate for most measurements performed by picoammeter. These instruments often use either coaxial or triaxial cables, a coaxial cable consists of a single conductor surrounded by a shield while triaxial cable adds a second shield around the first. However, coaxial cable also creates some noise when subjected to vibration, expansion or contraction. So all connections should be kept short, away from temperature changes (which would create thermal expansion forces), and preferably supported by taping to a non-vibrating surface. Section 3.3.2 discusses the wiring scheme and the connections used for UHV field emission measurements and section 3.3.3.1 discusses this for field emission measurements performed in the FIB.

Zero Drift and Offset Current

Zero drift is a gradual change of the indicated zero without the input signal. It is corrected by zeroing the measured signal before starting the measurement, unless it is corrected by zeroing, the resulting offset produces an error by adding to the input signal

level. This error may occur due to internally generated currents as in the case of instrument input offset current, or it can arise from external sources such as insulators and cables.

General methods of reducing zero drift are improved measurement circuit and the use of good quality insulation.

The ideal ammeter should read zero when its input terminals are left open, however practical ammeters do have some small current that flows when the input is open. This current is known as the input offset current, it is caused by bias currents of active devices and by leakage currents through insulators within the instrument. Offset currents can also be generated externally from sources such as triboelectric and piezoelectric effects. Triboelectric effects are generated by the charge created between a conductor and an insulator due to friction. A typical example is electrical currents generated by insulators and conductors rubbing together in a coaxial cable. Error currents also arise from electrochemical effects when ionic chemical creates weak batteries between conductors on a circuit board. For example, when commonly used epoxy printed circuit boards are not cleaned thoroughly of etching solutions, flux or other contamination can generate currents of a few nanoamperes between conductors.

Environmental Factors and Test Fixture Requirement

Variation in the ambient temperature can affect results in several ways such as thermal expansion or contraction of insulators produce noise currents. Radio frequency (RF) interference severely affects these measurements and in the presence of a close by source of RF interference, these measurements are not possible. There are several important requirements when it comes to test fixtures used for low-level measurements. The insulation resistance of all connectors, internal wiring, terminals, and sockets should be as high as possible and it should provide adequate shielding. The length of the wires and the number of connector should be minimised and special care should be taken about the system cleanliness.

3.3.2 Field Emission Measurements in the UHV

For the construction of a good low current measurement system all possible causes and source of errors, throughout the electrical wiring system needs to be considered, along with the effects due to surrounding environment on observations such as vibrations, RF measurements *etc.* Standard UHV systems with a turbo/diffusion pump and a rotary pump were used for these measurements. The UHV systems are located in the sputtering room, which is a noisy environment, with different type of experiments being performed which affect measurements. Measurements were performed late in the evening in order to minimise this environmental noise.

For the physical construction of an electrical measurement system, a UHV flange was fitted with vacuum feedthrough wires to provide electrical connection into the UHV system. The voltage source and the current measurement instruments were connected to the vacuum feedthrough wires on outside of the UHV system while performing measurements. The vacuum feedthrough wires, which were inside the UHV system, were connected via thin laminated Cu wires to an IC socket, which was held permanently by a supporting Cu plate on the inside of the vacuum feedthrough. Figure 3.2 shows the flange with IC socket used for these measurements. Hollow cylindrical steel connectors were used to connect the thin Cu wires, which were soldered to the IC socket with the feedthrough wires. The Cu wires from one side and vacuum feedthrough wires from the other side were fed into these steel cylinders and screws on the cylinders were tightened to make connections. The use of these connectors resulted in several difficulties, firstly it was physically difficult to make electrical connections with them, secondly there were approximately ten of these connectors, which resulted in the problem of connectors shorting with each other. Due to the unavailability of a better option, these connectors were used. The Cu wires were twisted in order to minimise interference from electromagnetic radiation.

Figure 3.3 shows a schematic of the specimen holder used for UHV measurements. The chips for field emission measurements were glued with silver paint to the central part of the Cu block. Wirebonding connected the chip to the Cu wiring on the IC board; this IC board was permanently fixed to the Cu block. The Cu wiring on the outside of the IC board was soldered to an IC plug. This assembly was plugged into the IC socket on the UHV flange for measurements.

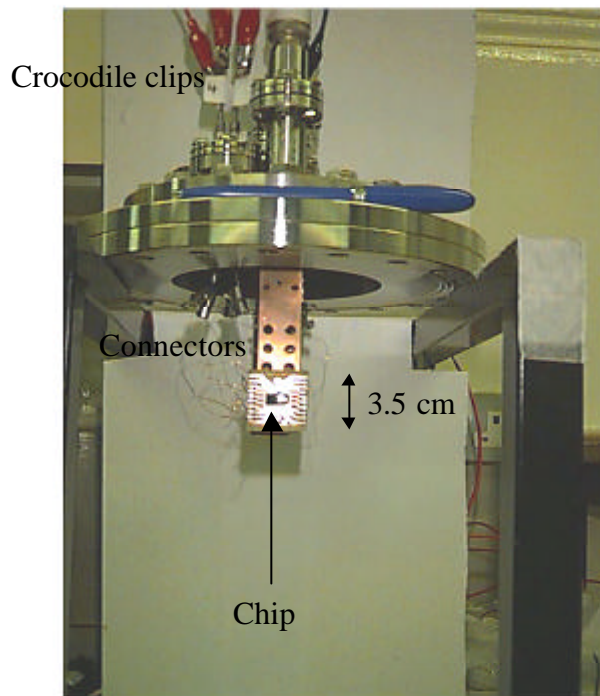


Figure 3.2 Photograph of the flange with chip, connectors, and crocodile clips used for UHV field emission measurements.

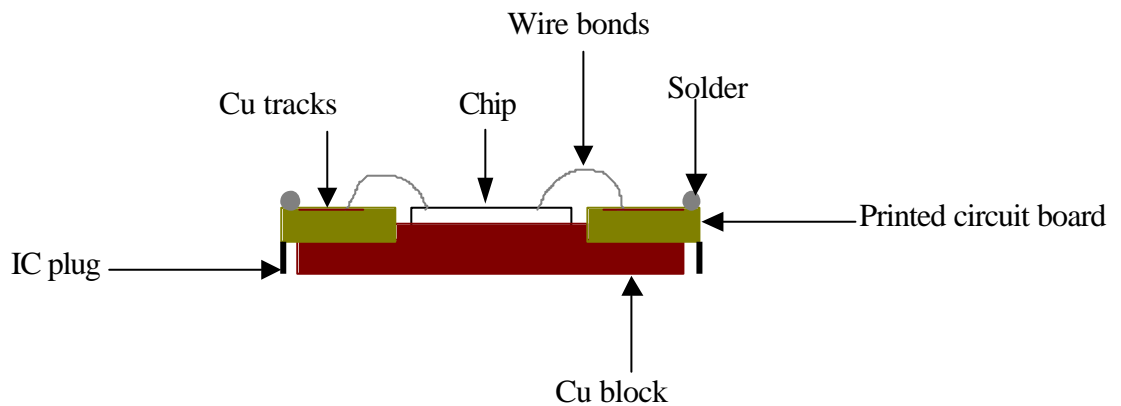


Figure 3.3 Schematic of the specimen holder (cross-sectional view) used for field emission measurements in the UHV.

Crocodile clips and banana plugs provided the electrical connections on the outside of the UHV system from the vacuum feedthrough to the power supply and the measurement circuit. The discussion in the previous section shows that usually the normal wiring and connections with crocodile clips and banana plugs are not sufficient for low current measurements. However in this case, the noise level was reduced by winding

ferrite beads (reduces electromagnetic noise) on the signal carrying wires and by using a metal shield over the crocodile clips on the vacuum feedthrough flange. During measurements, movement of the wiring was avoided, wiring was kept short to lower the noise level and the measurement circuit was kept very close to the flange. Any other large physical movements by the observer were also avoided.

As field emission tests were performed in UHV, the chip, the wiring and the chip holder *etc.* were thoroughly cleaned with acetone in an ultrasonic bath. Extra precautions were taken about loose connections and cleanliness while handling the equipment. Appendix 4 shows the measurement circuit, which was used for performing successful measurements. Measurement accuracy of well below one pA was obtained using this system and it was found suitable for performing accurate field emission measurements. Figure 3.4 shows the configuration in which the devices were connected for measurements.

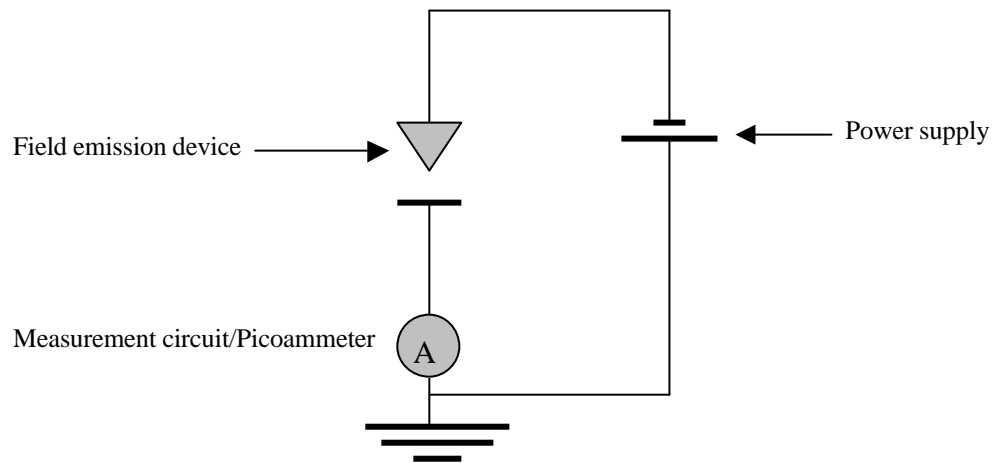


Figure 3.4 Schematic shows a field emission device connected for electrical testing.

After the initial success of field emission experiments, a Keithley 487 picoammeter was used for measurements. Figure 3.5 shows the measurement system used to observe field emission with a Keithley 487 picoammeter along with the apparatus to heat up devices in UHV.

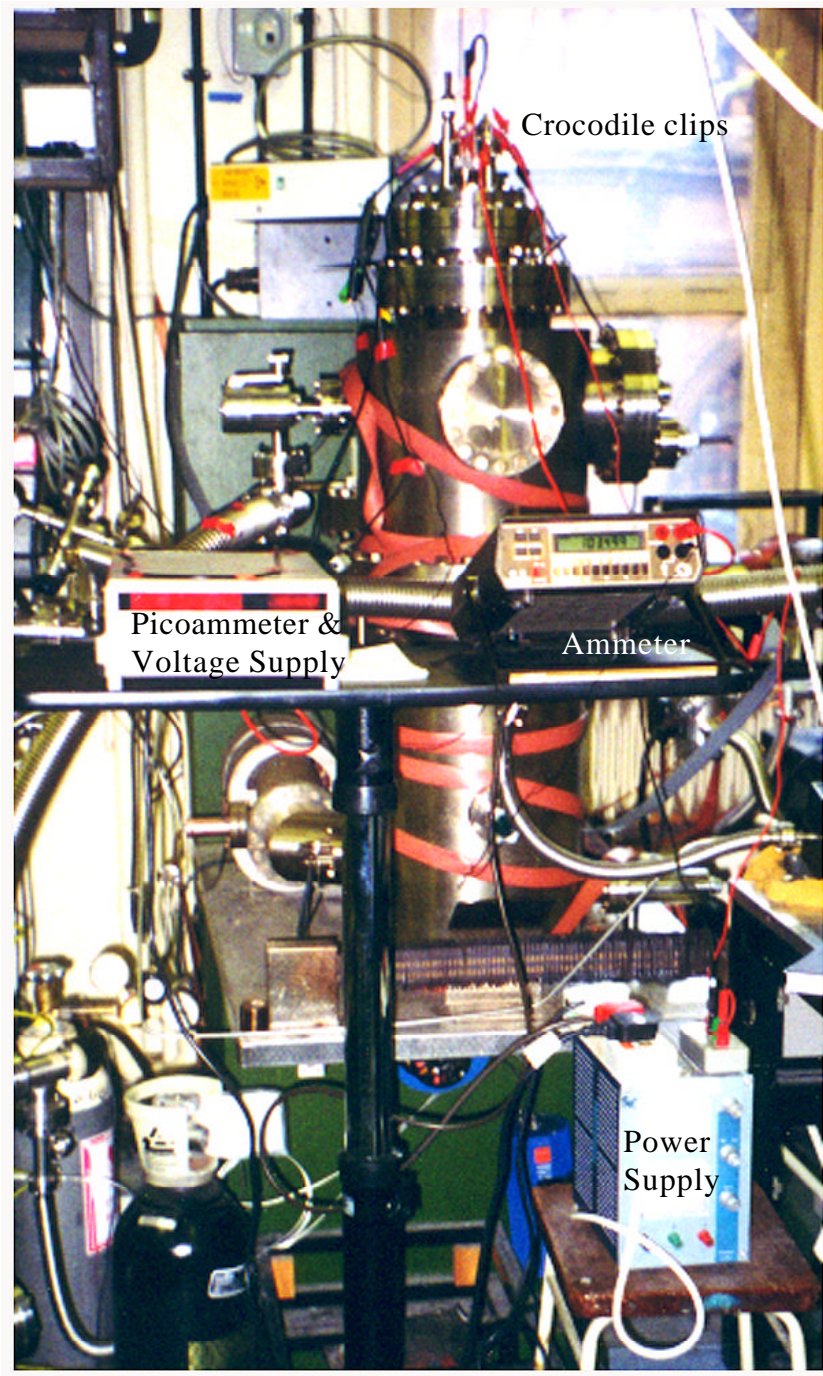


Figure 3.5 Photograph of UHV field emission measurement system using Keithley 487 picoammeter.

3.3.3 In-situ FIB Electrical Measurement System

An in-situ electrical FIB measurement system was built during the course of this project. The primary motivation for building such a system was to be able to perform unique type of experiments involving FIB milling and electrical currents. This system was

used for various experiments during this project such as: four-point resistance measurements during ion milling, application of heat to the chip in the FIB and field emission measurements. General considerations taken while designing this system were safety of the system, ease of use and flexibility. The following paragraphs discuss this system.

The safety of the FIB system was the most important consideration for the design of this system. After initial experimentation with different materials and different designs to ensure the safety of the system, finally the present set-up was decided which is relatively safe, flexible and easy to use. Figure 3.6 shows a schematic of the present set-up, in which electrical signals were provided via a vacuum feedthrough into the FIB chamber. The vacuum feedthrough was specially made from a round plate of stainless steel and an electrical socket was welded to this steel plate. Signals were provided from different instruments to the vacuum feedthrough by an electrical wire capable of carrying eighteen signals. This wire was plugged into the outside socket on the vacuum feedthrough while performing measurements, the other end of this wire was plugged into a socket in a metal box.

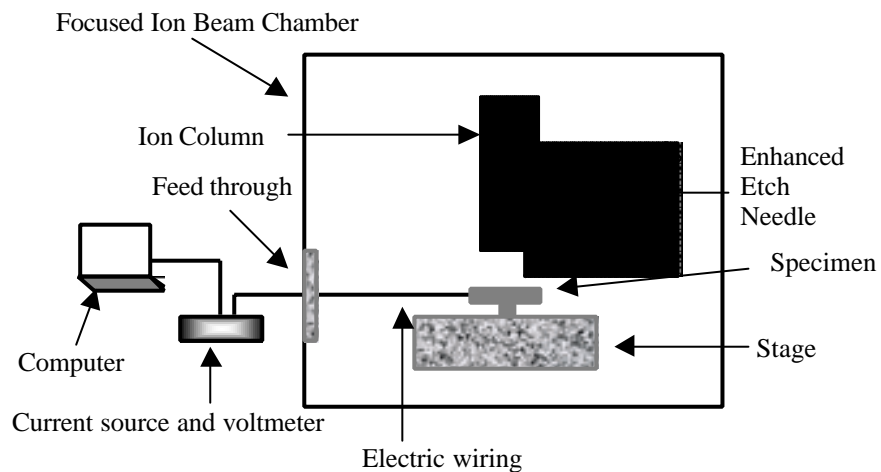


Figure 3.6 Schematic of the in-situ FIB experimental set-up.

Figure 3.7 shows a schematic of the metal box, this metal box also housed matrix boards for the selection of devices and the sockets for the incoming signals from different power supplies and measurement instruments. Laminated Cu wiring connected the sockets of different instruments with the matrix boards. The various instruments plugged into the metal box were computer controlled using Labview software.

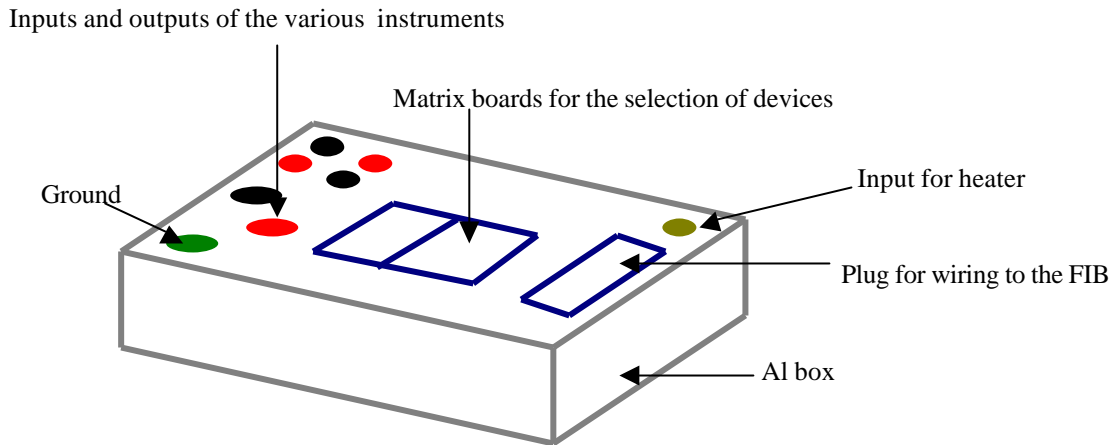


Figure 3.7 Schematic of the Al box shows different plugs and the matrix boards.

Figure 3.8 shows the wiring, plugs and sockets used inside and outside of the vacuum chamber of the FIB. Inside the vacuum chamber, wiring from the vacuum feedthrough was soldered to a socket, which was permanently fixed to the vacuum feedthrough. A plug, Cu wiring and an IC socket, which were permanently soldered to each other, connected the feedthrough to the specimen holder. This plug, the Cu wiring and the IC socket (connecting wire) were plugged in only while performing measurements.

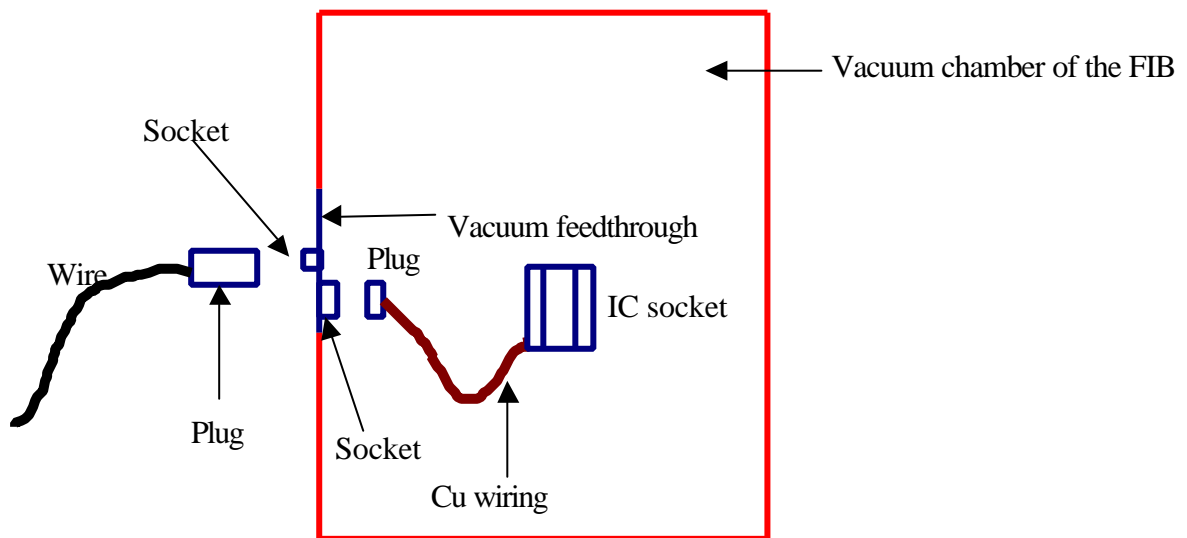


Figure 3.8 Schematic of the wiring, plugs, and sockets inside and outside of the vacuum chamber of the FIB.

A specially designed specimen holder was used for plugging into the IC socket. As the specimen holder was used in high vacuum, there were stringent requirements on the choice

of materials for the specimen holder. There were also limitations on physical dimensions and weight which can be used in the FIB system. These limitations and requirements are given below [Source: FIB manual for FEI 200 (1996)]:

- 50 mm × 50 mm × 15 mm maximum height.
- Maximum sample weight: 250 grams.
- Sample mount accommodates 15 mm thick samples with tilt eucentricity.

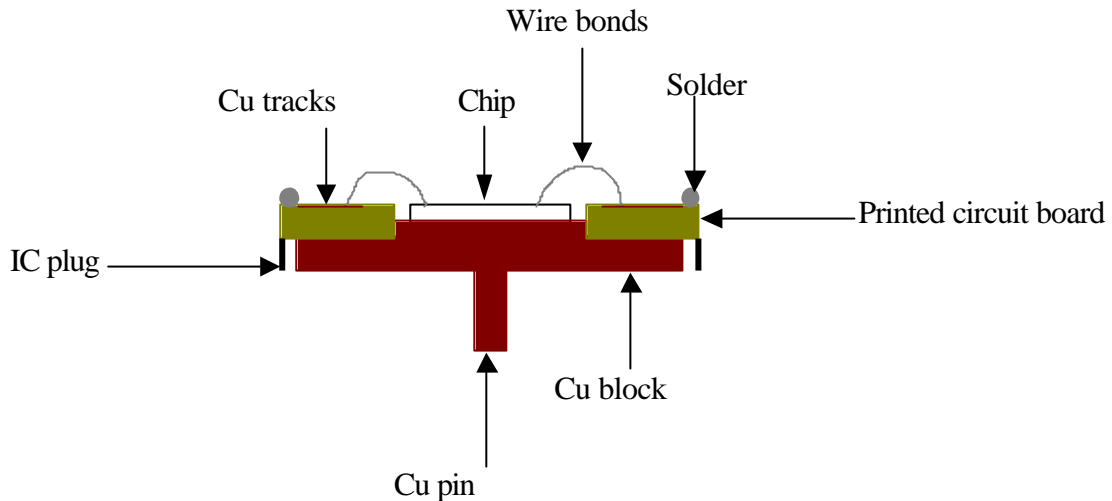


Figure 3.9 Schematic of the specimen holder (cross-sectional view) used for measurements in the FIB.

Figure 3.9 shows a schematic of the Cu specimen holder. In the upper middle part of the Cu block, the chip was glued down using silver paint. A printed circuit board surrounded the chip, which was fixed to the Cu block. The chip was wire bonded to the Cu wiring of the printed circuit board. The other end of the Cu wiring on the printed circuit board was soldered to an IC plug. Before performing measurements, one end of the connecting wire was connected to the feedthrough and the other end to the specimen holder. The bottom part of the Cu block had a Cu pin, which protruded out through the rectangular hole in the middle of the IC plug, this Cu pin fitted into the specimen holder on the stage of the FIB. The Cu pin was pushed into the specimen holder on the stage of the FIB and screw on the FIB stage was tightened to hold the specimen holder down onto the stage of the FIB.

As there was Cu wiring hanging from the IC socket inside the FIB chamber, there was limitation to the degree of rotation of the specimen holder. The specimen holder could not be rotated several times in the same direction as this would have caused winding up of

Cu wiring around the stage, which may have resulted in an accident. Baring this limitation, all other operations of the FIB could be performed normally.

The method described above was used after first few attempts. Initially a less flexible method was experimented in which the IC socket with the Cu wiring (connecting wire) was permanently soldered to the electrical feedthrough on the flange. With this measurement set-up, the electrical feedthrough was removed after each FIB session. Figure 3.10 shows the outside of the in-situ FIB measurement system.

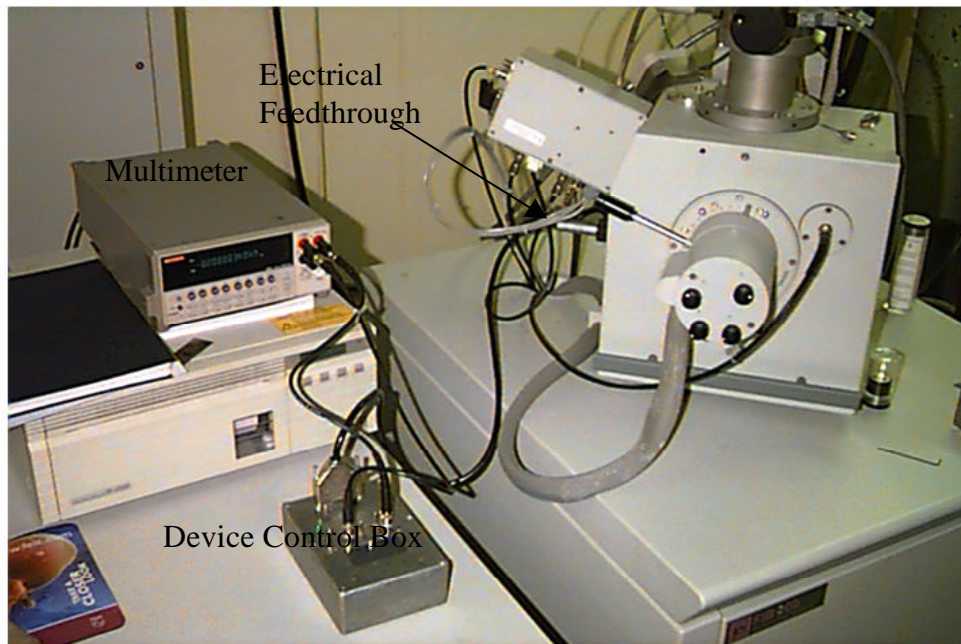


Figure 3.10 In-situ FIB measurement system.

3.3.3.1 Field Emission Measurements in the FIB

Field emission measurements were attempted in the FIB system, which required designing a system with the considerations, previously mentioned in section 3.3.1, in order to minimise the noise. All these considerations could not be taken into account while designing such a system due to measurements being performed in the FIB. However every precaution was taken to minimise the noise level. The field emission system designed for the testing of field emission devices in the FIB is discussed below and the design of the system has been compared with the design of the UHV field emission system.

As discussed in section 3.3.2, in the UHV field emission system signals were directly taken from the feedthrough wires to the measurement circuit. This avoided unnecessary noise and it was straightforward to select a particular device with the

crocodile clips as the feedthrough wires were protruding out of the flange. However, in the case of the FIB a socket on the feedthrough was used, which made it necessary to build some other type of device selection and voltage supply system. As described in the previous section signals were taken from the feedthrough on the FIB system and were fed into a socket, which was located on a metal box. The wiring in the metal box has also been described in the previous section. For the testing of field emission devices the signal line from the matrix board was connected to the socket of the triaxial cable, and then signal from the socket was carried to the picoammeter via a triaxial cable. It was attempted to minimise the length of the wiring and the number of connections wherever possible but there were still more wiring and increased number of connections than the UHV field emission system.

Another difference between the UHV and the FIB field emission measurement system was the length of the wiring and number of connections used inside the vacuum system. The wiring used inside the vacuum system in the FIB was relatively long, this was required in order to permit opening and closing of the chamber. This wiring could not be twisted as it could have damaged the FIB system. There were also some extra connections relative to the UHV system, which arose due to the connecting wire. As mentioned in the previous section an approach of fixed wiring with the flange was attempted but it was discontinued as it posed difficulties with the handling of the system.

This increased length of wiring and increased number of connections resulted in increased noise. The length of the wiring and the number of connections could not be simply reduced. One of the problems was the initial high level of current measured on changing the voltage level and then slowly damping of it. To avoid this, the observations were made by slowly increasing the voltage level. Ferrite beads were used on the 18 signals wire from the FIB chamber to the metal box. Al foil shielding was also used to cover this wire and the metal box for some measurements. After all these precautions, the noise level could be controlled below 2 pA which permitted the detection of field emission.

3.3.3.2 Heating inside FIB

In-situ electrical FIB measurement system was used to provide heating to the specimen. A heater was built in order to heat the specimens in the FIB for the following purposes:

- To observe the effect of heating on devices while performing in-situ FIB electrical measurements.
- To observe effects on the imaging properties of materials due to heating.
- To measure any enhancement, which may occur due to heating while simple ion milling or ion milling with enhanced etch.

Two different designs and different materials were experimented to select the correct materials and design for the heater. In the first design of the heater, a resistive wire was wound on a Cu screw, which was screwed into the Cu block of the specimen holder. The principle employed behind this design was that as the Cu screw heats up due to resistive heating, the Cu block will also heat up, which will eventually result in heating up of the devices. This design was discarded due to difficulties associated with the oxidation of the lamination of the resistive wire. In the second design, a commercial electric resistive heater was used for the heating of the devices. This heater was embedded into a Cu tube with a screw on it, this Cu tube was then screwed in the Cu block of the specimen holder. The wiring from the heater was soldered to the circuit board of the specimen holder to electrically connect it. A resistor glued within a cavity of the Cu block, functioned as a thermometer. Figure 3.11 and 3.12 show the specimen holder with the heater and the thermometer.

Different difficulties ranging from the selection of optimum materials, degassing of materials, melting of materials and oxidation of lamination were encountered while designing this heater. One difficulty was the heat conduction from the specimen holder to the stage of the FIB thus resulting in heating up of the stage. One solution to this problem was to use a PTFE pin on the bottom side of the Cu block (rather than the Cu pin). This Cu pin was the only physical contact between the Cu block and the stage thus the path for heat conduction. It was attempted to use a PTFE pin instead of the Cu pin, however this solution was not successful. PTFE pin could be screwed into the Cu block but when the screw in the stage of FIB was tightened to hold the specimen holder, the specimen holder could be freely rotated, as PTFE is soft. The successful solution employed an Al pin with a circular plate as head instead of the Cu pin. A circular PTFE plate was screwed into the Cu block for thermal isolation, then the Al pin with the circular head was screwed into the PTFE plate. This design achieved good thermal isolation, and the heater could be used in the FIB.

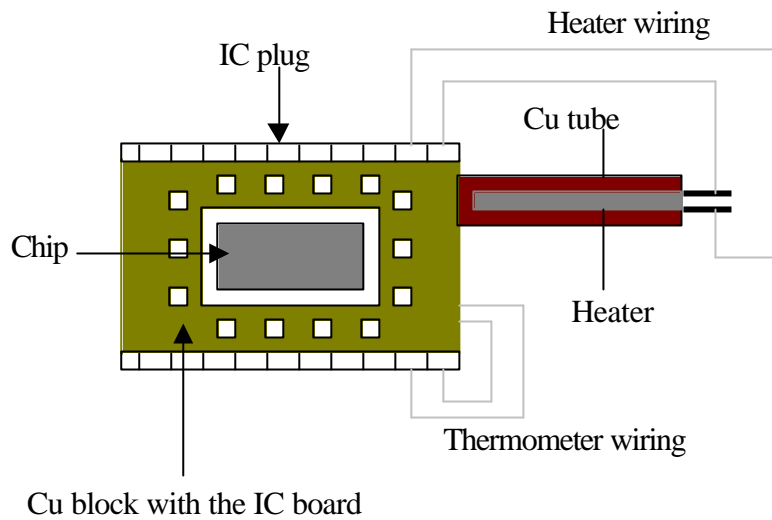


Figure 3.11 Schematic of the specimen holder with the heater (view from the top).

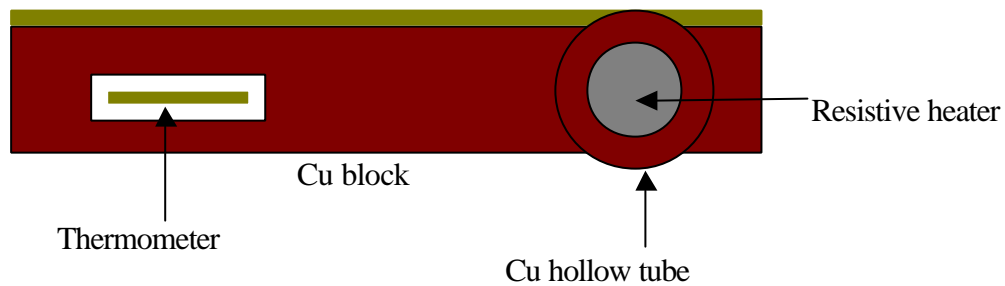


Figure 3.12 Schematic of the specimen holder with the heater (view from the side).

The heater was first degassed in the vacuum chamber of an evaporator, it was then calibrated and afterwards tested in the FIB chamber. Minor degradation of vacuum occurred at 100°C due to the heating of the stage as it started to be degassed. Image drift was observed at high magnification, this occurred due to the weak Al-PTFE (metal-plastic) connection. These problems are minor and can be removed by higher quality machining of the heater. The heater was commonly kept in a dessicator to avoid moisture absorbing into the materials. It was successfully tested several times in the FIB.

3.3.3.3 Four-Point Resistance Measurements in the FIB

In-situ FIB four-point resistance measurements were performed while ion milling metal tracks. The measurement set-up used was similar to the one used for field emission measurements. The width and length of the tracks used in calculations for these measurements were measured in the FIB. Keithley 2000 multimeter was used as a current source and for measuring the voltage. The instrument was interfaced with the computer on the FIB and the measurements were recorded with a Labview programme.

3.4 Summary

Fabrication and testing of field emission devices and other measurements such as AFM measurements involved different fabrication and measurement methods. Specimen fabrication methods used included: photolithography, sputtering, chemical etching *etc.* In order to perform different measurements two measurement systems were built: a UHV low current measurement system and an in-situ FIB electrical measurement system. Low current measurements are sensitive to various factors and their accuracy increases due to the use of high quality insulators, shielding of wires and general cleanliness of the system. An in-situ FIB electrical measurement system was built as it leads to unique type of experiments involving FIB milling and electrical currents. This electrical measurement system was used for four-point resistance measurements, field emission measurements and in-situ FIB heating. UHV field emission measurement system because of the flexibility in terms of wiring and connectors was superior to the in-situ FIB field emission measurement system. The in-situ FIB electrical measurement system has proved to be very useful and more applications of it are expected in the future.

3.5 References

1. S. A. Campell, *The Science and Engineering of Microelectronic Fabrication*, (Oxford University Press, 1996).
2. C. R. M. Grovenor, (Chapter 7), *Microelectronic materials*, (IOP publishing, 1989).
3. S. M. Sze, Chapter 5, *VLSI Technology*, (McGraw-Hill, 1988).
4. Keithley *Low Level Measurements* 5th edition.
5. P. Horowitz and W. Hill, *The Art of Electronics*, (Cambridge University press, 1997).

Chapter 4

Real Time Resistometric Depth Monitoring in the FIB

4.1 Introduction

Device fabrication at the nanometer scale with FIB encounters various difficulties. One of the major difficulties is the accurate and reproducible measurement of high aspect ratio nanometer scale FIB cuts and the accurate detection of end point. The field of superconducting devices is one such area in which researchers are facing such difficulties. The devices require FIB milling of nanometer scale high aspect ratio cuts for the definition of tunnel junction and precise definition of SQUID structures [1,2]. These applications need accurate thickness measurement and end point detection in order to fabricate devices with reproducible characteristics and to avoid excess sputter deposition. Various methods have been described in the literature to accurately measure the thickness and to detect the end point. These methods include in-situ FIB methods such as absorbed current method and ion beam excited photo-emission method [3-5]. There are also ex-situ FIB methods such as SEM, TEM and profilometer height measurement. All these methods are either very difficult, impossible or unreliable for the purpose of depth monitoring and end point detection for high aspect ratio nanometer scale cuts. A new technique employing four-point resistance measurement has been developed which monitors real depth of a thin patterned film as it is milled by FIB. This method overcomes problems associated with other methods mentioned above. The technique was calibrated using AFM for 1 μm wide cuts, the reproducibility of the technique was verified and the technique was tested for 50 nm wide and 400 nm deep (high aspect ratio) FIB cuts in Nb film.

4.2 Thickness Measurement Techniques for High Aspect Ratio Cuts

Thickness measurement techniques have been divided into two categories: general thickness measurement techniques and the absorbed current method. General thickness measurement techniques

include SEM, TEM, AFM and profilometer measurements. There are also reported in the literature methods that are in-situ FIB thickness measurement other than the absorbed current method: the ion beam excited photoemission method and the optical beam induced current method. The ion beam excited photo emission method has been demonstrated for μm size wide cuts and has not been tested for nanometer scale high aspect ratio cuts [5]. The optical beam induced current method has been demonstrated for even larger area milling [6]. The following section discusses the limitations of the general thickness measurement techniques and the absorbed current method for the purpose of high aspect ratio cuts. This is followed by discussion of the working principle of the new in-situ FIB measurement technique.

4.2.1 General Thickness Measurement Techniques

In principle, these techniques can measure thickness with nanometer scale accuracy. However, the measurements are performed outside the FIB chamber. Most of these techniques involve removal of the specimen from the specimen holder and often require special specimen preparation. Furthermore, these techniques have specific requirements, which in some cases are practically impossible to satisfy. Techniques not involving special specimen preparation include AFM and profilometer measurements. In the case of AFM, there are constraints on the specimen aspect ratio and it is practically impossible to measure nanometer scale high aspect ratio cuts. Chapter 5 discusses the limitation of the AFM technique for measurement of high aspect ratio cuts. Profilometer has a resolution of approximately 20nm; however, locating a nanometer scale feature with eye or optical microscope is a near-impossible task. Techniques involving special specimen preparation include SEM and TEM. FIB systems that have combined FIB and SEM (advanced SEM's have a resolution of approximately 1 nm), it is possible to measure milled depth in-situ. However this requires special fabrication of trenches around a high aspect ratio feature, which is time consuming and which may prove to be destructive in case of some devices. TEM can resolve atomic layers but depth monitoring using this technique will require destruction of the specific specimen to perform any type of depth measurement.

4.2.2 Absorbed Current Method, Difficulties and Limitations

The working principle of this method has been described in chapter 2. The technique is simple in principle, the stage current is measured as the ion beam mills the material. The stage current is different for different materials so it can detect end point. This simplicity leads this technique to be a standard feature in FIB machines. The technique can be used in several ways:

- To detect materials while milling through a multi-layered structure.
- To detect thin layers of oxide on the surface of materials.
- To measure milled depth after calibration.

However this method suffers from a few limitations. As the end point is detected by monitoring the change of the current signal during ion milling, a continuous electrical path is required from the area being milled to the measuring instrument. Presence of insulators and multi-layered structures complicate the information obtained, and in certain cases, no signal to the ground is possible. The method works well for areas few μm^2

in size with conducting substrates and with a simple electrical path to the ground. For milled areas with dimensions in nanometers, due to the presence of high noise level in the signal the information is unreliable. The method provides complicated information while ion milling with enhanced etch. This occurs due the presence of I_2 gas on the surface, which affects the signal level, I_2 also changes the material removal mechanism from physical mechanism (sputtering) to physical and chemical mechanism.

4.2.3 Model for Resistometric Depth Monitoring Technique

Different thickness measurement techniques were discussed in the previous sections and the discussion revealed that presently for nanometer scale high aspect ratio cuts, there is no in-situ FIB technique to measure milled depth. Measurement techniques, which were ex-situ were either very difficult or impossible for milled depth measurements for these types of structures. The information obtained from the ex-situ methods is also dependent upon the milling conditions used during the calibration of a standard. The complications and limitations involved in other methods led to the development of a new technique, which uses the new in-situ FIB electrical system. This system has been described in chapter 3.

The new method requires a metal track whose resistance can be measured. The change in resistance of the track is monitored as it is milled, which increases as the thickness of the track in the milled area decreases. The thickness fraction of the milled track can be calculated from the resistance measurements using a simple model. In order to calculate the thickness fraction milled from the resistance measurements, it is assumed that the milled structures have vertical walls and a flat bottom. Figure 4.1 shows a schematic of a milled track. The different parameters for the model are also shown in figure 4.1 where l is defined as the length of the track, w the width of the track and t the total thickness of the track. R_{track} is the initial resistance measured of the whole track and is given by equation (4.1).

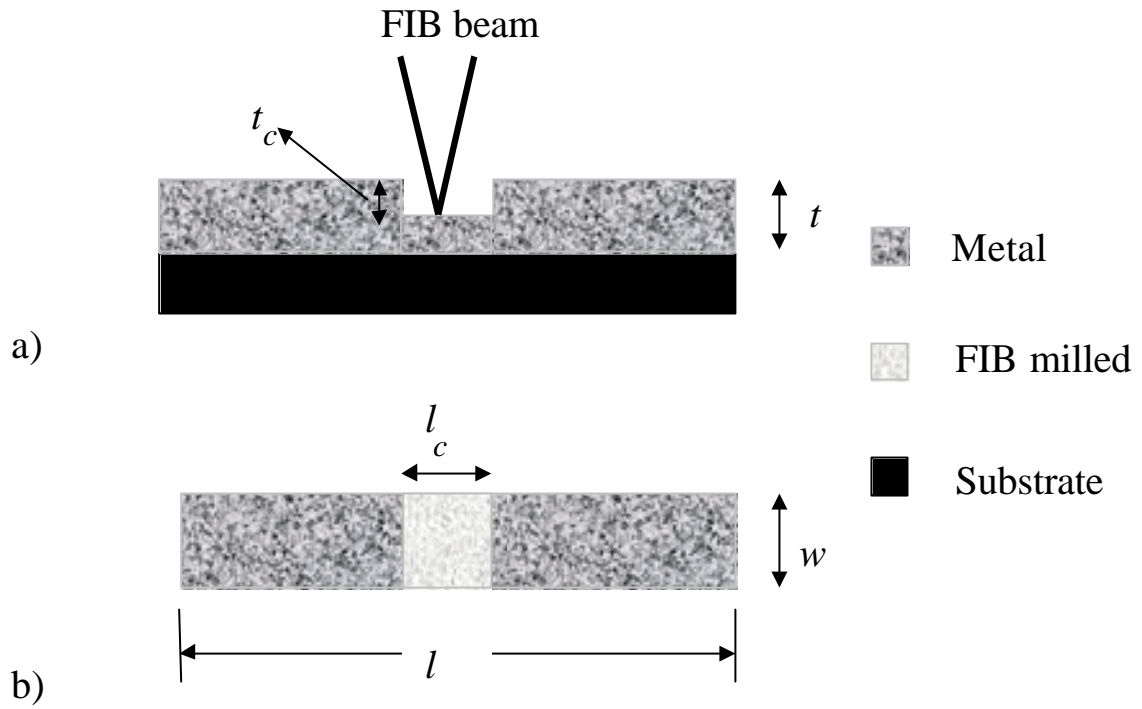


Figure 4.1 Different views of a metal track milled with the FIB;
 a) Cross-section of the metal track milled with the FIB.
 b) Top view of the milled area of the metal track.

$$R_{track} = \frac{\mathbf{r}l}{wt} \quad (4.1)$$

$DR = R_{variable} - R_{initial}$ is the resistance change of the track due to ion milling. $R_{variable}$ is the resistance of the milled portion of the track during ion milling and is given by equation (4.3). $R_{initial}$ is the initial resistance of the milled portion of the track prior to ion milling and is given by equation (4.2).

$$R_{initial} = \frac{\mathbf{r}l_c}{wt} \quad (4.2)$$

and

$$R_{variable} = \frac{\mathbf{r}l_c}{w(t - t_c)} \quad (4.3)$$

where l_c is the width of cut, t_c is the thickness milled and \mathbf{r} is the resistivity of the material.

By subtracting equation (4.2) from equation (4.3), the resistance change due to ion milling is calculated in the following way:

$$\Delta R = \frac{rl_c}{wt} \left[\left(\frac{1}{1 - \frac{t_c}{t}} \right) - 1 \right] \quad (4.4)$$

By substituting equation (4.1) in equation (4.2), the following equation is obtained:

$$R_{initial} = R_{track} \left[\frac{l_c}{l} \right] \quad (4.5)$$

The thickness fraction milled (f_t) can be expressed by substituting equation (4.5) in equation (4.4)

$$f_t = 1 - \left[\left(\frac{\Delta R}{R_{track} f_l} \right) + 1 \right]^{-1} \quad (4.6)$$

where the thickness fraction milled of the track $f_t = (t_c/t)$, the length fraction of the track milled $f_l = (l_c/l)$. Note that the equation (4.6) expresses the thickness fraction milled of the track by using only the directly measured quantities.

The model provides the framework to convert the resistance measurements to the thickness fraction milled. In-situ electrical measurements were performed and the milled depth was calculated using the above model. The milled depth calculated was then compared with milled depth measurements by AFM to discover the accuracy of the technique. Due to the limitations of the AFM technique to access high aspect ratio cuts, 1 μm wide cuts were used. Different electrical measurements were compared to verify the reproducibility of the technique. Electrical measurements were also performed on 50 nm wide 400 nm deep cuts in Nb.

4.3 Measurements

A standard four-point measurement technique was used to measure the resistance of the track by monitoring the voltage as the track was milled. The time and the size of the structure to be milled were specified on the computer and the resistance changes were measured with time. Material used was Nb, which was sputter deposited on oxidised Si substrates. Photolithography and CF_4 reactive ion etching were performed to fabricate tracks with line widths of 1 μm and 1.5 μm and thicknesses of 400 nm and 405 nm respectively. Appendix 2 shows the photolithographic mask used for the measurements. The specimens were wire-bonded onto a specimen holder with electrical contacts and then connected to the wiring on the stage of the FIB, using the holder described in chapter 3. Direct current was supplied and voltage signals were

measured using a Keithley 2000 digital voltmeter. These instruments were read by Labview software running on the FIB control computer as described in chapter 3.

4.3.1 Verification and Reproducibility of the Technique

The technique was verified by comparing the thickness measured by electrical measurements with the thickness measurements by AFM for $1\ \mu\text{m}$ wide cuts. For this experiment, Nb tracks of width $1.5\ \mu\text{m}$ and thickness $405\ \text{nm}$ were milled with $11\ \text{pA}$ beam current and enhanced etch to create pattern sizes of $1\ \mu\text{m}$ by $2\ \mu\text{m}$. Figure 4.2 shows a schematic of a Nb track with FIB milling patterns overlaid on it. Enhanced etch was used in order to avoid re-deposition of the sputtered material, which affects measurements.

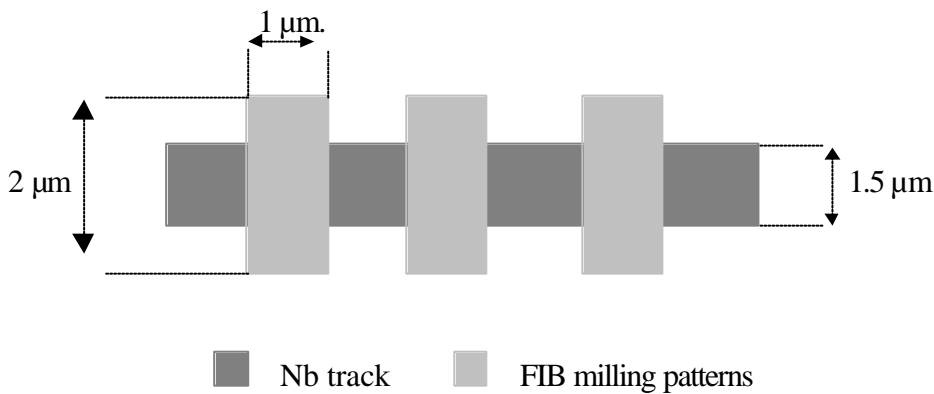


Figure 4.2 Schematic of a metal track $1.5\ \mu\text{m}$ wide with FIB milling patterns of size $1\ \mu\text{m}$ by $2\ \mu\text{m}$ overlaid on it.

Figure 4.3 shows the resistance change versus milling time for six rectangular milled structures with different milling times. The resulting resistance measurements have been displaced by $0.25\ \Omega$ to show the general trend and to separate each curve from the other. The insert in figure 4.3 shows the resistance change against milling time for longer milling time. Long milling time to remove all the Nb was selected. It was observed that the measured resistance increases steeply with milling time and with long milling time, the resistance cannot be observed using the present apparatus. After milling for 44 seconds all the Nb in the pattern area was milled away.

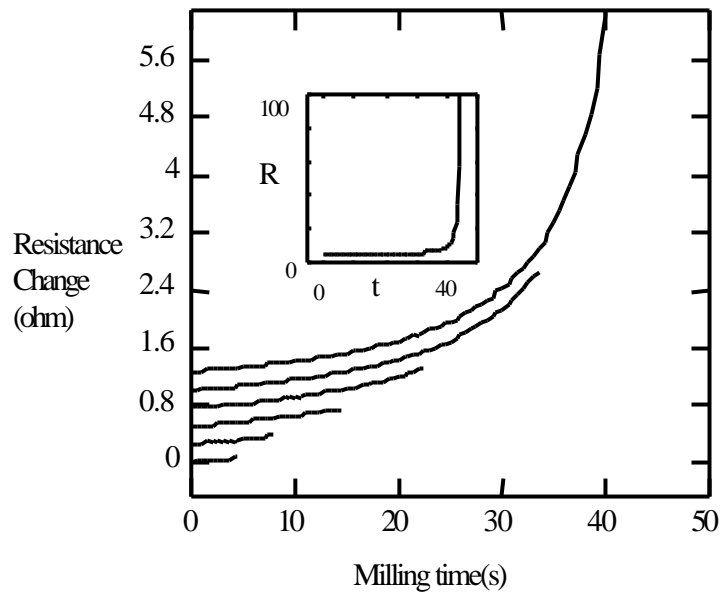


Figure 4.3 Resistance increase is measured while milling rectangular patterns $1\ \mu\text{m}$ by $2\ \mu\text{m}$ using milling times of 40 s, 33 s, 22 s, 11 s, 7.5 s and 4 s (from top). The measurements are displaced by $0.25\ \Omega$ from each other. The insert shows the resistance change up to 44 s.

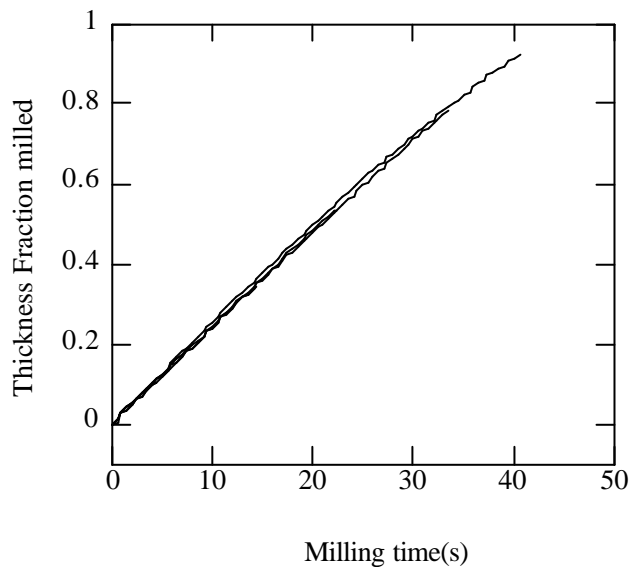


Figure 4.4 A plot of fraction thickness milled against milling times of 4 s, 7.5 s, 22 s, 33 s and 40 s. The areas milled were rectangular in size measuring 1 by $2\ \mu\text{m}$.

Figure 4.4 shows a plot of milling time versus the thickness fraction milled for milling times of 4 s, 7.5 s, 14.5 s, 22 s, 33 s and 40 s. This plot shows the reproducibility of the milling depth using this technique. A standard deviation of 7.22×10^{-3} is obtained for the thickness fraction milled after 20 s for 5 different measurements. The graph also shows the reproducibility of the measurements with this technique.

Over 0.6 thickness fraction milled, there is a slight deviation from the linear behaviour, this occurs due to the narrowing of the track as shown in figure 4.5.

Figure 4.5 is a secondary electron FIB image of a track of Nb with four rectangular milled structures of size $1\ \mu\text{m}$ by $2\ \mu\text{m}$. Decrease in the width of the track is observed with increased milling time. This decrease in width of Nb track occurs because of the enhanced removal of material sputtered out of the side-walls of the track. The initial blurring of the image at the edges of the track is attributed to re-deposition of the material during imaging prior to the rectangular milling of the track. This re-sputtered material does not interfere in any observable way with the electrical measurements.

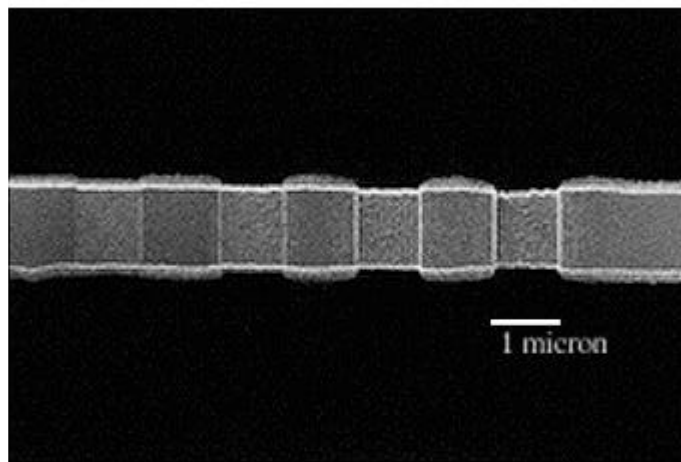


Figure 4.5 A Nb track with rectangular patterns milled of dimensions $1\ \mu\text{m}$ by $2\ \mu\text{m}$. Patterns milled with increasing time from left 5 s, 11 s, 22 s, and 33 s.

Nano-protrusions were observed by AFM in the enhanced etch milled regions, which occur due to the uneven material removal by the chemical species present during milling. The protrusions present in the milled regions stop the AFM tip reaching the bottom of the milled structures (the top of the base material). These protrusions form a highly inefficient electrical path on top of a base material. The base material effectively contributes to all of the observed electrical measurements. Hence in order to accurately measure the thickness milled, the minimum observed value in the milled region was subtracted from the average thickness of adjacent non-milled region. Figure 4.6 shows a plot of the thickness fraction milled obtained using resistive measurements versus milled depth obtained using AFM measurements. The plot is a straight line ($y = 391.1 x$ at a thickness of 391.1 nm). The plot shows that in-situ FIB resistance measurement technique accurately provides information regarding milled depth.

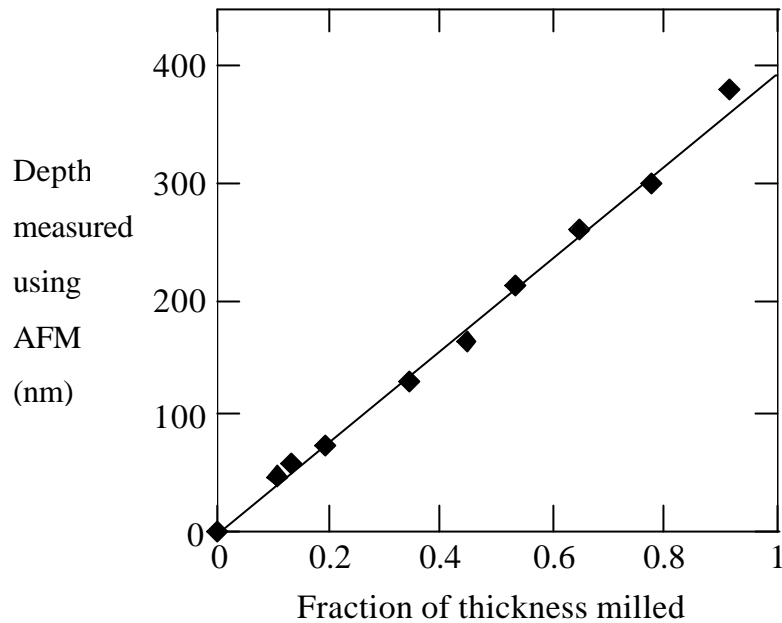


Figure 4.6 Plot of fraction of thickness milled against depth measurements by AFM. Rectangular milled structures of size $1.2\ \mu\text{m}$ by $1\ \mu\text{m}$ were used.

4.3.2 High Aspect Ratio Structures

The capability of this technique to measure thickness of high aspect ratio structures by simple ion milling and by ion milling with enhanced etch was tested. 200nm wide cuts were fabricated in a 400nm thick Nb track with simple ion milling (without I_2 enhanced etch) using 4pA beam current and milling patterns of dimensions $0.2\ \mu\text{m}$ by $1.11\ \mu\text{m}$. 50nm wide cuts were fabricated in a similar Nb track with 4pA beam current and enhanced etch by using only single pixel line. The widths of the cuts were measured by imaging in the FIB. Figure 4.7 shows a plot of the thickness fraction milled against the milling time calculated using equation (4.6). The fluctuations in the thickness fraction milled occurred due to the accuracy of the measuring instrument. The measured resistance changes are very low ($10^{-9}\ \Omega$) at the start of milling, these resistance changes increase as milling proceeds and less fluctuations are observed.

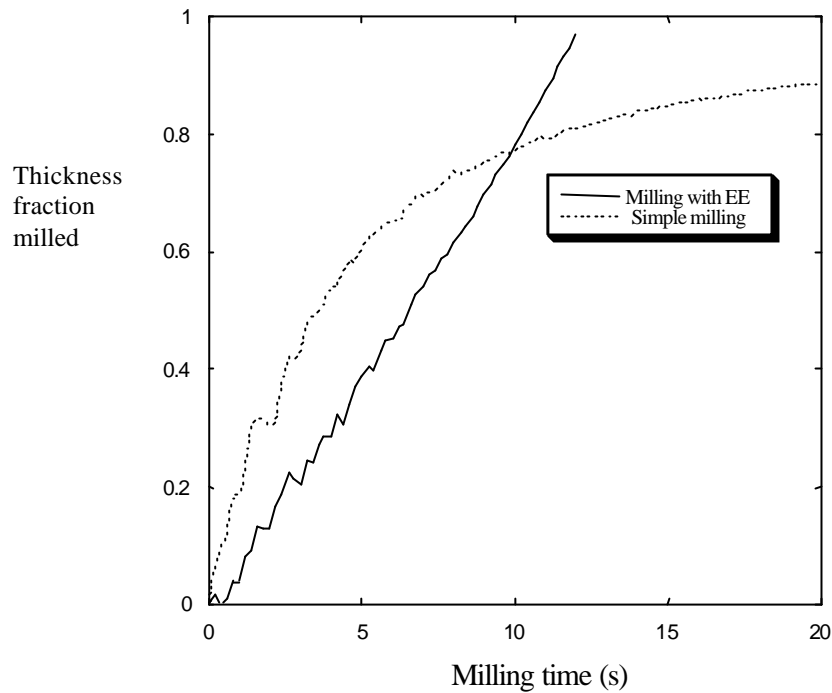


Figure 4.7 Thickness fraction milled against milling time for simple ion milling and milling with enhanced etch using 4 pA beam current. Rectangular pattern size of 0.2 μm by 1.11 μm and single pixel line scan were used respectively.

When enhanced etch is used the thickness fraction milled increases linearly up to the measured 0.95 thickness fraction. The linear behaviour shows lack of re-deposition effects and measurement up to 0.95 thickness fraction shows that a higher aspect ratio of the cut is achieved at the end point. In the case of simple ion milling, the thickness fraction milled increases linearly with milling time up to 0.5 of the total thickness and then shows non-linear behaviour. The re-deposited material changes the shape of the milled structure significantly from the ideal shape assumed in the model and it also interferes with the Ga^+ ion beam. These two effects combined together are responsible for this non-linear behaviour.

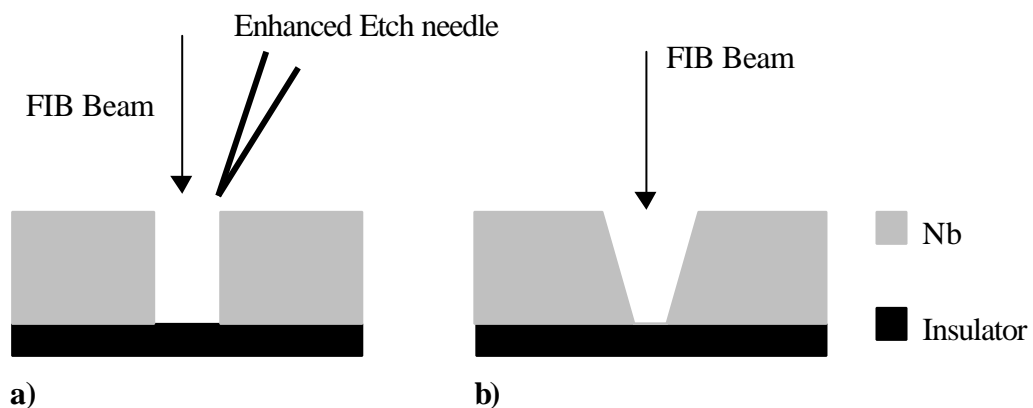


Figure 4.8 Cross-section of two different shapes of the FIB milled structure **a)** using enhanced etch **b)** using simple ion milling.

The application of in-situ FIB measurements to measure thickness provides unique information, which can also be interpreted to provide information regarding the shape of the milled structure, the uniformity of milling and other effects like narrowing. Figure 4.8 shows two structures, figure 4.8 a) is milled using enhanced etch and figure 4.8 b) is milled using simple ion milling. In figure 4.8 a) Nb is milled uniformly, there is no sputter deposited material and no narrowing. In figure 4.8 b) sputter deposition occurs and the shape of the structure changes, it becomes narrow at the bottom. The material removal rate is non-linear as it is easier to remove material when milling starts than when the structure is deeper. These two shapes will show similar results to the one's shown in figure 4.7.

Thickness measurement by this method has applications in machining using FIB which require accurate and reproducible removal of material at nanometer scale and control over re-deposition (as the end point is detected accurately, control over re-deposition is obtained). There is currently no other in-situ method available for accurate monitoring of depth for 50 nm wide and 400 nm deep cuts. In the absorbed current method the noise signal level is too high to monitor depth accurately. The ion beam excited photo emission method has not been reported to be tested for such high aspect ratio cuts. The method however suffers limitations due to the noise from the side walls of the milled structure. With ex-situ methods, AFM and profilometer, it is not possible to access the bottom of these high aspect ratio structure to measure thickness. The use of SEM to measure thickness requires formation of cavities around the track to make any possible observations and TEM requires preparation of thin sections, which makes both these techniques impracticable and destructive.

4.4 Summary

Thickness measurements of nanometer scale high aspect ratio cuts are becoming increasingly important due to new device applications using the FIB requiring them. These measurements are either very difficult or practically impossible with techniques such as AFM, TEM and SEM. The newly developed in-situ FIB electrical measurement system was used in order to overcome the difficulties encountered by other techniques. In-situ resistometric measurements on metal tracks while ion milling them were performed, these resistance measurements were converted by a simple model to thickness measurements. The reproducibility and accuracy of thickness measurements by this method were tested. Comparing the thickness data from this technique with the thickness measurements by AFM tested the accuracy of the technique for 1 μm wide cuts. A linear relationship between the fraction milled with milling time was observed for milling with enhanced etch for 50 nm wide cuts in 400 nm thick (high aspect ratio cut) track. For these cuts, the fraction milled is accurately measured to approximately 2% with the present experimental set-up.

4.5 References

1. R. W. Moseley, W. E. Booiij, E. J. Tarte, and M. G. Blamire, *Appl. Phys. Lett.* **75**, 262 (1999).
2. J. F. Walker, D. F. Moore, and J. T. Whitney, *Microelectronic Engineering* **30**, 517 (1996).
3. S. T. Davies and B. Khamsehpour, *J. Vac. Sci. Technol. B* **11**, 263 (1993).
4. F. Itoh, A. Shimase, S. Haraichi, and T. Takahashi, *Int. J. Jpn. Soc. Precis. Eng.* **27**, 209 (1993).
5. H. Yamaguchi, K. Saitoh, and M. Mizumura, *J. Vac. Sci. Technol. B* **16**, 2555 (1998).
6. N. Antoniou, M. Thompson, J. Salen, D. Casey, R. R. Goruganthu, R. Ring, J. Birdsley, and G. Gilfeather, *J. Vac. Sci. Technol. B* **17**, 2730 (1999).

Chapter 5

Direct Measurements of FIB Cut Parameters

5.1 Introduction

FIB fabrication presently includes fabricating various devices and structures including accelerometer, superconducting devices, nanostructures for biochemical analysis and micro-cantilevers [1-5]. FIB fabrication of these devices and structures involve milling with line cuts and cuts with dimensions in nanometers. The applications of the FIB technique are expected to grow in the area of the mentioned applications and related areas. There are also possible future commercial applications of the technique in mass manufacturing [6]. Some of the important factors influencing device characteristics are uniformity of the width of FIB cut along the length of the FIB milled cut and reproducibility of FIB milling. Various materials are being used for fabricating devices such as Si and Nb with different material properties and it is very important to identify the material properties, which influence the width of cut. The present study was conducted using three different materials such as Si (single crystal), Nb (polycrystalline) and $\text{Co}_{66}\text{Si}_{16}\text{B}_{12}\text{Fe}_4\text{Mo}_2$ (amorphous material).

AFM technique was selected for the present study as it is better than other methods for width measurements and as it also provides information regarding the depth and shape of the FIB cut. The major advantage of the AFM method over techniques such as FIB and SEM for these measurements is that it provides information along the whole length of the FIB cut. Section 5.2 compares three different techniques for such a study and demonstrates the capability of the AFM technique. AFM technique has been previously used to discover the width, the depth and the profile of the FIB cut in MgO for the fabrication of High T_c superconducting Josephson junctions [7]. Section 5.2 also discusses the limitations of the AFM technique particularly for depth of cut and shape profile measurements, and presents a data analysis framework, which is useful for these measurements. Section 5.3 and 5.4 present experimental scheme and results obtained from Si. Section 5.5 discusses width measurements from Si, Nb and the amorphous material.

5.2 *Comparison of Techniques, Definitions and Reliability*

This section compares three different techniques: AFM, FIB and SEM. These techniques are the different methods available for performing width and depth measurements on nanometer scale cuts. TEM is another method available for these measurements however considerable difficulty is involved in order to use this method for such an investigation. Due to this reason, the following paragraphs discuss only AFM, FIB and SEM. AFM method was used as it provides width measurements along the whole length of the cut, it also provides information regarding depth of cut and information regarding the shape of the cut for low aspect ratio cuts. This section also discusses the tip interaction with different shapes of the milled structures in order to obtain better understanding of the information provided by AFM. The last part of this section defines a framework, which is necessary for data analysis.

SEM and FIB are the other two techniques that can be used in order to determine width, depth and shape of the milled cuts. One common method used in these two techniques is to image the FIB milled profile in cross-section. This type of approach only provides information at a specific point and information along the whole length of the track is not obtained. There are other difficulties associated with measurements using these two techniques. For example, the FIB technique encounters several difficulties and limitations:

- Both the vertical and spatial resolutions of the FIB imaging technique are low for these types of measurements.
- Imaging is difficult, as it is very easy to destroy nanometer scale structures using the FIB.
- Imaging in cross-section method is
difficult, as it involves cutting of nanometer scale structures for the purpose of depth measurements.

The SEM technique faces the following difficulties for these types of measurements:

- SEM generates secondary electron signal from depth of approximately 100 nm's which results in loss of surface information [8]. Information such as deposit or re-sputtered material on the surface will be nearly impossible to image.
- Imaging in cross-section is difficult, as it involves specimen fabrication in the FIB and then imaging in the SEM. (It is particularly difficult with the present facilities in the

materials department as FEG (SEM) and FIB requires two different types of stubs and great care regarding specimen cleanliness is required.)

AFM technique provides an alternative to these two methods. It offers the following benefits for these types of measurements:

- Information can be obtained along the whole length of the milled cut.
- It provides surface information, which makes it particularly suitable for width measurements.
- No special sample preparation is required.
- The vertical resolution of the technique is well below one nanometer so it should accurately measure nanometer scale cuts.

A limitation involving work with the AFM on nanometer scale cuts arises due to the high aspect ratio of the FIB milled cuts. This occurs due to the tip not reaching the bottom of such a structure. This particular investigation used etched Si tips, the tip radius is between 5-10 nm, side angle is 17° , front angle is 25° and back angle is 10° (This information is provided by Veeco Ltd., the supplier of the tip.). In order to consider the limitations of this technique for the purpose of these measurements, the front and the back angles are important. Figure 5.1 shows a 3-dimensional sketch of the tip, along with sketches of the different angles of the tip. As the AFM tip moves towards the milled structure with milled structure lying perpendicular to the direction of the motion of the tip, the side angle is the angle of the tip as viewed from the milled structure. The front angle and the back angle of the tip are the angles viewed from the side of the milled structure as the tip moves across the milled structure. Figure 5.2 shows cross-sectional views of two types of structures along with an AFM tip, two different types of structures are shown to facilitate understanding of information obtained from AFM. Figure 5.2(a) shows a case where the AFM tip interferes with the vertical walls of the structure to provide inaccurate information. The profile of the FIB cut is imaged as asymmetric due to the interaction of the AFM tip with the vertical walls of the structure. As drawn the figure shows that AFM tip measures accurately the width and depth of the structure. The figure shows the approximate angles of the AFM tip, for simplicity the tip radius of 5 nm to 10 nm is not drawn. Calculations show that AFM tip should measure depth and width of structures with aspect ratio of approximately 1.5. For such a structure, the vertical structure will be imaged as triangular in shape with walls deviating 10° and 25° from the vertical as the back and the

front of the tip interacts with the walls of the structure. For higher aspect ratio structures, the AFM tip will not be able to access the bottom of the structures. Figure 5.2 c) shows a structure, which has a triangular cross-section, the structure will be imaged as symmetrical as shown in figure 5.2 d). The variation in the angle Ω results in false or correct information obtained while performing measurements with AFM on such a structure. If Ω is higher than 65° then interference from the front angle of the AFM tip will occur thus resulting in an asymmetrical shape. If Ω is higher than 80° then interference from the back angle will also occur, which should also result in an asymmetrical shape. However, if the angle Ω is lower than 65° then a symmetrical shape of such a structure should be observed.

The discussion so far has established that AFM is the best method available for the width and depth measurements for low aspect ratio FIB milled cuts. A data analysis framework is required to analyse data. This framework requires definition of parameters such as the width of the cut, the depth of the milled structure, the height of the sputtered material and the length of the sputtered material. These parameters have practical use in the field of nanofabrication with the FIB. The first step for data analysis requires flattening using the AFM software, section analysis provides width and depth information for analysis after flattening. Figure 5.3 shows an actual section analysis of a FIB cut, the measured milled structure is approximately 30 nm deep and 100 nm wide. The structure is symmetrical around the center, and the bottom part of the structure is flat. Other shapes of the structures were also observed as discussed in section 5.4, however this shape has been selected in order to build a framework for analysis. This shape is selected as a standard shape for analysis because it is symmetrical and shows a flat bottom part of structure thus an indication of the correct depth. Figure 5.4 shows a sketch of a shape used for data analysis, it also defines the different milling parameters. Due to the presence of the sputtered material, the ends of the milled structure are higher than the original Si surface without FIB milling. Another method for data analysis will be an attempt to fit a gaussian density distribution function and extract information. However, this method is not practical because of the presence of the sputtered material and because not all shapes of the structure observed were symmetrical. The width of the cut (W_c) is measured from one side of the milled structure to the other side from the original Si surface (thus excluding the sputtered material). The depth of the milled structure (D_m) is the milled depth by the FIB from the

original Si surface to the bottom of the milled structure. The angle θ is defined as the angle from the bottom part to the top part of the milled structure. The height of the sputtered material (H_r) is the height measured from the top of the sputtered material to the level of the original surface. A better estimate of H_r , is equal to half of the sum of the heights of the sputtered material from both sides of the milled structure. The length of the sputtered material (L_c) is measured from inside the milled structure from where it starts to the distance where the sputtered material does not contribute to the measured height. This parameter is very difficult to measure and at times arbitrary, so it is not probed in detail.

5.3 Experimental Scheme

Experiments were performed using three beam currents (150 pA, 70 pA and 11 pA), however only data from 150 pA and 70 pA beam currents was analysed. Errors occur in the data obtained from 11 pA beam current due to fluctuations in the beam current and the reproducibility of data from this beam current (low beam current) is also susceptible to the alignment of the FIB column. As these errors can be particularly large at low beam currents, data from 11 pA beam current is not discussed in section 5.4. Table 5.1 shows the three beam currents used for milling along with their milling spot sizes.

Table 5.1 Beam currents used for FIB milling and the corresponding milling spot size [Source: FIB manual for FEI 200 (1996)].

Beam current (pA)	Milling spot size (nm)
150	35
70	25
11	15

All experiments were performed using Si.mtr (silicon material file) and this milling file uses 50% overlap and 1 μ s dwell time. Experiments were performed using four different magnifications, which result in different actual overlaps of the FIB milling spot thus it is a method to test the reproducibility of the technique. The difference between the overlap as specified in the material files and actual beam overlap is explained below.

Table 5.2 Various magnifications used for the FIB milling and the corresponding pixel resolution.

Magnification	Pixel spacing (nm)
10,000×	7.4
12,000×	6.1
15,000×	4.9
20,000×	3.7

Table 5.2 shows different magnifications and the corresponding pixel spacing used while performing these experiments. For the calculation of the pixel spacing equation 5.1 is used.

$$\text{Pixel spacing} = (\text{HFW})/\# \text{ of Pixels} \quad (5.1)$$

Where HFW means horizontal full width of the screen and # of pixel equals to 4096 due to the use of a 12 bit analogue-to-digital card. (Information provided by FEI technical staff.) The actual beam overlap can be calculated by knowing the method by which FIB calculates the horizontal displacement in order to achieve the beam overlap as specified in the material file. In order to calculate the horizontal displacement which the beam spot size has to move, FIB first calculates a target step size using equation 5.2, which depends on the material file and the milling spot size.

$$\text{Target step size} = [1 - (\% \text{overlap}/100)] \times [\text{Milling spot size}] \quad (5.2)$$

After calculating the target step size, then it chooses the horizontal displacement depending on the pixel spacing. The method of choosing the horizontal displacement is clarified with the help of examples. If the target step size is 12 nm and pixel size is smaller than this value then the value of the horizontal displacement cannot be more than the value of the calculated target step size. For example, if the pixels are 5 nm apart there will be a two pixel step displacement equal to 10 nm spacing. However, if the pixels are 7 nm apart there will be a one pixel step displacement equal to 7 nm spacing. In cases where pixel size is bigger than the calculated target size then there is one pixel step displacement. For example, if the pixels are 18 nm apart there will be one pixel step displacement equal to 18 nm.

The actual overlap is calculated using equation 5.3.

$$\text{Overlap \%} = [1 - (\text{horizontal displacement} / \text{spot size})] \times 100 \quad (5.3)$$

(The information regarding the calculation of overlap was provided by FEI technical staff.)

Table 5.3 shows the actual beam overlaps for different magnifications and beam currents for Silicon material file (50% overlap and 1 μs dwell time).

Table 5.3 Actual beam overlaps calculated for different magnifications and beam currents for Si material file (50% overlap).

Beam current	Actual Beam Overlap (%)				
150 pA	57.7	65.1	58.0	57.7	50.2
70 pA	70.4	51.6	60.8	55.6	53.6
11 pA	50.6	59.3	67.3	50.6	61.3
Magnification	10,000 \times	12,000 \times	15,000 \times	20,000 \times	25,000 \times

Experiments were performed on chips of size approximately 10 mm \times 10 mm. These chips were glued to SEM stub with silver paint before FIB processing. High beam current (6.6 nA) was used in the FIB to first fabricate markers on the chips, these markers were visible with the optical microscope, under low magnification. High beam current was also used to fabricate grids with a number of square boxes close to the markers, the square boxes in grids had dimensions of 15 μm \times 15 μm . This particular dimension was selected as it makes the AFM measurements simple to perform. 5 μm long structures with different milling times were milled with FIB line cuts in each box of the grid. The structures were milled in the order of milling time, starting from the lowest milling time and finishing at the longest milling time. Magnification was varied across the grid, while beam current was varied down the grid. Figure 5.5 shows a sketch of the marker, the grid and the milled lines for Si, similar grids were used for other materials. This figure is drawn using Si as an example, the figure shows that during the fabrication of the grid, the naturally grown SiO_2 has been removed down to Si between the different square shaped box structures. So there is no possibility of any charge during milling in one box affecting milling in another box. Astigmatism (non-circular beam) in the beam was removed whenever the beam current

was changed, astigmatism was also tested whenever enhanced etch was used. Astigmatism was removed by first fabricating a hole in the specimen in the spot mode and then observing the milled structure. If the milled structure was circular in shape, it was assumed that astigmatism was removed. After FIB milling specimens were removed from the SEM stub using acetone. Specimens were then inspected under an optical microscope for any deposit on the surface.

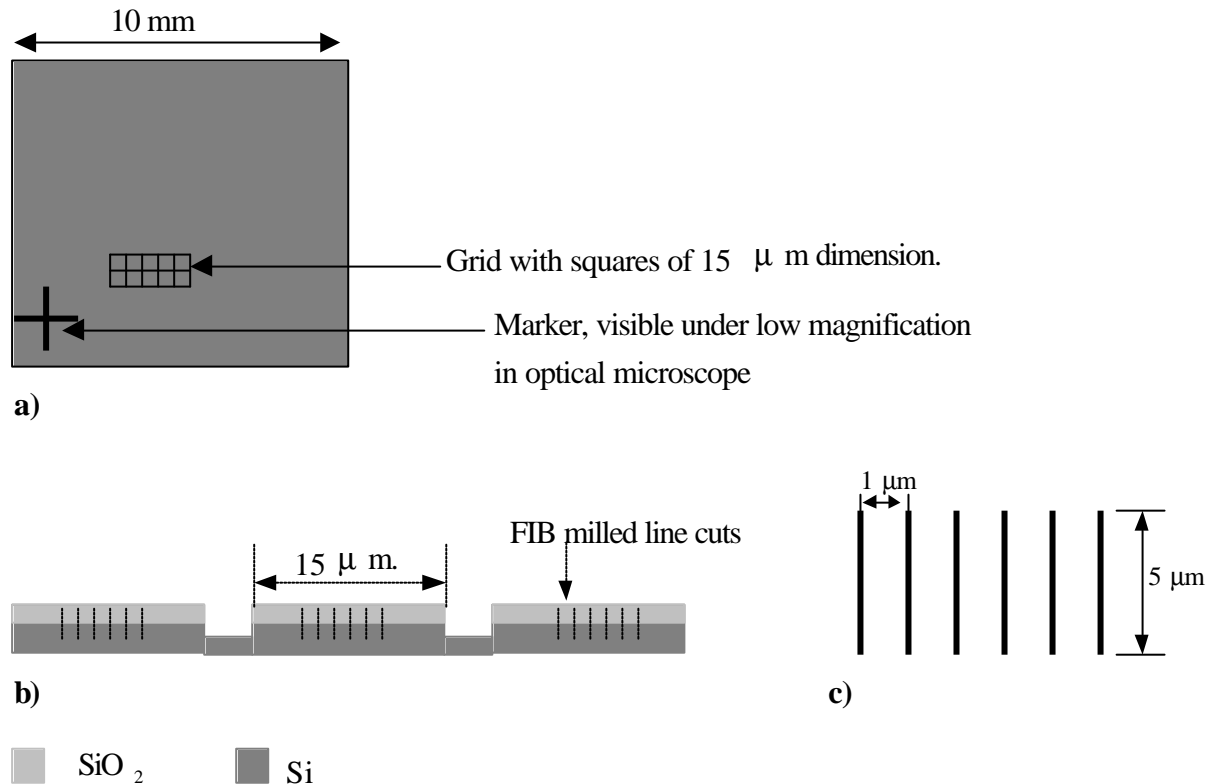


Figure 5.5 Schematic of the experimental scheme used (not drawn to scale), the SiO₂ can be as thick as 2.5 nm [9]. **a)** Schematic of the chip, marker and grid structure. **b)** Cross-section of the grid structure. **c)** Top view of the milled structures in a box of the grid.

If further cleaning was needed specimens were cleaned in an ultrasonic bath with acetone and then AFM measurements were performed. There are different measurement errors present, which include errors while obtaining data from the AFM software, fluctuations in the beam current and measurement errors in the AFM measurements itself. These errors are unavoidable, for example fluctuations in the beam current are inherent to the technique. The effects of errors due to AFM measurement and errors while obtaining

data from the AFM software are low as a number of readings were averaged to obtain any particular data point.

Table 5.4 summarises the milling times used to fabricate cuts. A deeper understanding of the milling file used is obtained by understanding the various trends in the table. Table 5.4 shows the following trends:

- A linear increase of milling time as the nominal milled depth increases with the same beam current.
- In order to achieve the same nominal milled depth with a lower beam current, the total dosage of Ga⁺ ions decreases.
- The term (milling time × beam current)/milling spot size, which is the Ga⁺ ion dosage per unit area, increases linearly with the beam current and is the same for the same nominal milled depth for different beam currents.

Table 5.4 Milling times used for FIB milling, along with the different beam currents. The last row of the table shows the nominal milled depth corresponding to different milling times. (Information obtained from the FIB work station).

Beam current	Milling time(s)					
150 pA	0.77	1.64	2.45	3.28	4.10	4.91
70 pA	1.17	2.37	3.52	4.69	5.88	7.13
11 pA	3.40	6.81	10.22	13.63	17.04	20.45
Nominal milled depth (nm)	10	20	30	40	50	60

These trends show that the material file has been designed while taking into consideration the factor of Ga⁺ ion dosage per unit area. This information is useful for designing new material files.

5.4 Results and Discussion

5.4.1 Measurements of FIB Cuts in Si

Si is an important material in the field of applications regarding FIB. Si has this importance due to the use of the FIB in the semiconductor industry and its application in

research areas such as applications in MEMS and nanostructures for biological applications [1,4,5]. Experiments were performed using both simple ion milling and ion milling with enhanced etch on Si. Results from only two beam currents 70 pA and 150 pA are discussed as difficulties were encountered while analysing data with 11 pA beam current (discussed in section 5.3). AFM images and section analysis were obtained for all the different magnifications and beam currents experimented. The study was performed using Si with the naturally occurring oxide, the oxide was not removed as it is not commonly removed in applications such as nanostructures for biochemical analysis [4].

5.4.1.1 150 pA Beam Current (Simple Ion Milling)

Figure 5.6 (a) shows a height image of the Si surface with six milled structures for magnification 12,000 \times . Figure 5.6 (b) is a section analysis through the FIB cuts fabricated on Si. In the image, the milling time increases from the left of the figure towards the right. The following paragraphs present and discuss different information obtained from such images for example the depth of the milled cut, width of the cut *etc.*

The contrast on figure 5.6 (a) shows the height variation and the white areas are approximately 3-4 nm higher than the darker areas. The width of cut is in the range of 100 nm while the milled depth varies from approximately 10 nm to 40 nm. The width of the cut is larger than the milling spot size because atoms eject from the surface due to atomic collision cascades triggered by the incident ions. An incident ion hits the surface of the material at a particular point and the momentum transfers to a few atoms, which eject from different points on the surface. Figure 5.6 (b), shows an increase in the milled depth as the milling time increases. Comparison of different section analysis across the same

milled structure showed the measured milled depth variation of 3-4 nm. The variation in the width of cut is approximately 3-4 nm along the 5 μm length of the milled structure. This observation shows that in a single-crystal Si, the width of cut remains approximately constant along the length of the structure. The variation of the milled depth and different shapes of the structures are discussed in the last part of this section.

Figure 5.7 shows 6 AFM cross-sections associated with the 6 milled depths obtained from section analysis performed on FIB milled line cuts using 150 pA and magnification 15,000 \times . Symmetrical shapes were purposely selected that show a flat bottom of the structure as it demonstrates that AFM is measuring the correct depth and the shape of the milled structure. Any slight deviation from symmetry has occurred during the process of obtaining the AFM cross-sections. The last part of this section discusses structures that did not show a flat bottom. Figure 5.7 shows an increase in the milled depth as milling time increases. The angle θ between the flat bottom part of the structure and the top of the milled structure increases from the lowest depth milled to the highest depth milled of the cuts. Figure 5.7 f) provides a value of θ of approximately 30 $^\circ$. The width of the cut increases with the milling time from approximately 85 nm to 105 nm, and the depth of cut from approximately 8 nm to 37 nm. It was attempted to plot the height of the sputtered material against milling time. Due the presence of high value of noise as the height of the sputtered material is in the order of a few nm (a technique of averaging a number of readings was also used), and due to variation in the height of material close to the sputtered material this could not be done. The length of the sputtered material is in the range of 100 nm, this imposes limits on the proximity of the FIB cuts before material from one milled structure will start to interfere with the other milled structure.

Figure 5.8 shows a plot of the milled depth as measured by AFM versus milling time for the four different magnifications. Five readings were averaged to obtain every data point in order to improve the accuracy of the data. There is saturation in milled depth occurring as milling time increases in the case of magnification 10,000 \times . The milled depth increases approximately linearly with the milling time for magnifications 12,000 \times and there is a slight deviation from linearity in the case of magnification 15,000 \times . Measurements from magnification 20,000 \times show a linear increase in milled depth,

however the measured milled depth is very much lower as compared with measurements from magnifications 12,000× and 15,000×. The reasons for the variation in the milled depth are explained in the later part of this section with the help of AFM cross-sections.

Figure 5.9 is a plot of the width of cut against milling time for the four magnifications. Width of cut measurements for magnification 10,000× show a higher width of cut than width of cut measurements for magnifications of 12,000× and 15,000×. Width of cut measurements for all these three magnifications show an increase in the width of cut with milling time. Width of cut measurements for magnification of 20,000× first shows an increase in the width of cut, which after further milling changes to decrease in the width of cut. Ga precipitation due to low solid solubility of Ga in Si has resulted in the as observed measurements. This is discussed in detail in the later part of this section with the help of AFM cross-sections.

In the literature, beam drift due to the presence of Ga precipitation has been reported [10]. TEM observations showed a dark core under the region from where beam drift occurred for line dosages of 2.2×10^{11} ions cm^{-1} . The core was observed 30 nm underneath the Si surface from where the beam drifted. Energy filtered images in the study indicated that the core mainly consisted of Ga, interspersed with a little Si. The dark core as observed in TEM was fairly constant in depth (20-30 nm). The resultant shape of the milled structure due to beam drift was a flat plateau along a milled structure. The Ga core occurred under the flat plateau region from where the beam drift occurred. The core was associated with low solubility of Ga in Si, which resulted in Ga precipitation [10]. Another study showed a distorted profile of a milled structure in Si, a step was observed inside the milled structure. The distortion within the milled structure occurred due to beam drift [4].

In order to analyse the possibility of Ga precipitation resulting in the as observed results, the solid solubility of Ga in Si and ion dosages which can result in Ga precipitation needs to be considered. Exposure of a square window with dimension $10 \mu\text{m}$ for one second with 150 pA beam current result in ion dosage of 10^{15} ions cm^{-2} . Thus a single image of the area to be milled can result in Ga precipitation as Si has low solid solubility of Ga of $9 \times 10^{18} \text{cm}^{-3}$ at 500°C [11]. Ga precipitation affecting the results is a real possibility as milling was performed with line dosages in the order of 10^{13} and 10^{14} ions

cm^{-1} , and in the previously reported work line dosages of 10^{11} ions cm^{-1} resulted in beam drift [4,9].

The results are explained below in the order of distortion from an ideal structure, which is assumed to occur without any beam drift. In order to explain in detail the reasons for different shapes observed for different magnifications. The following factors need to be considered:

- Focusing was performed in some of the boxes in the grid, using an advanced feature of the FIB. In this advanced feature rather than imaging the whole computer screen, a window can be defined on the computer screen and the beam is focused in the defined window.
- A single image of the area to be milled can result in Ga precipitation as Si has low solid solubility of Ga of $9 \times 10^{18} \text{cm}^{-3}$ at 500°C [11].

Focusing should result in Ga precipitation in the particular region, as milling was not performed in the same region where beam was focused, this should not affect measurements. A possible mechanism by which Ga from the focused region can affect the measurements is by diffusion. As nanolithographic application of SiO_2 has been reported in the literature [12], if any long range Ga diffusion was occurring lithography will not work. Due to this reason, the probability of this mechanism affecting the results is low.

The high sensitivity of Si to precipitate out Ga seems the likely cause. Imaging of the specimen surface where structures were fabricated was avoided as much as possible. However at times it was unavoidable as it was necessary to know where milling was being performed. Focusing in the grid structure was also necessary as displacements of approximately $50 \mu\text{m}$ on a sloping specimen can result in different results. During finding the area where to perform milling, the dosage of Ga slightly varied between the boxes, thus resulting in different observed results.

Magnification 15,000

In the case of observations, from magnification $15,000\times$ two types of structures were observed, symmetrical structures with flat bottom parts and structures, which were symmetrical except at the bottom part. Figure 5.7 shows symmetrical structures with flat bottoms. As most of the Ga^+ ions are concentrated in the middle part of the symmetrical

structures, precipitation of Ga is expected to occur in this part and more Ga precipitation should occur as milling time increases. It was observed that as milling time increases flat bottoms of the structures became less common. Bottom parts of the structures as observed for magnification 12,000 \times (figure 5.10) became more common. This observation supports that Ga precipitation which starts in the middle part of the structure results in different shapes.

In milled depth measurements for magnification 15,000 \times , there is a slight deviation from linearity. The deviation may have occurred due to fluctuations in the beam current. An increase in width of cut with milling time occurs due to the spread of Ga⁺ ions within the beam. As milling time increases the number of ions milling a specific area increase thus increasing the milled width with time. In the literature, increase in width of structure (MgO) with milling time is reported [7].

Magnification 12,000 \times

Figure 5.10 shows shapes of structures obtained from FIB milled structures with 150 pA beam current and magnification 12,000 \times . The structures are asymmetrical in shape, the angle θ of the milled structures is lower or equal to 30° and the width is similar to one obtained for magnification 15,000 \times . It is reasonable to assume that AFM tip provides correct information regarding the shape and depth of these milled structures because in the case of magnification 15,000 \times , structures with θ of 30° and similar depth and width are correctly measured. Milled structures with flat bottom which are symmetrical can be observed for the first three milling times for this particular magnification. As milling time increases, symmetry disappears along with the flat bottom part of the structures. These observations again support that with longer milling time more Ga precipitation occurs and in this particular case results in asymmetrical structures. For this particular magnification, milled depth increases approximately linearly with milling time and an increase in width of cut with milling time is observed. For magnifications 12,000 \times and 15,000 \times the actual beam overlap parameters are 65% and 58%, this possibly results in different width of cuts and depths milled for these two magnifications.

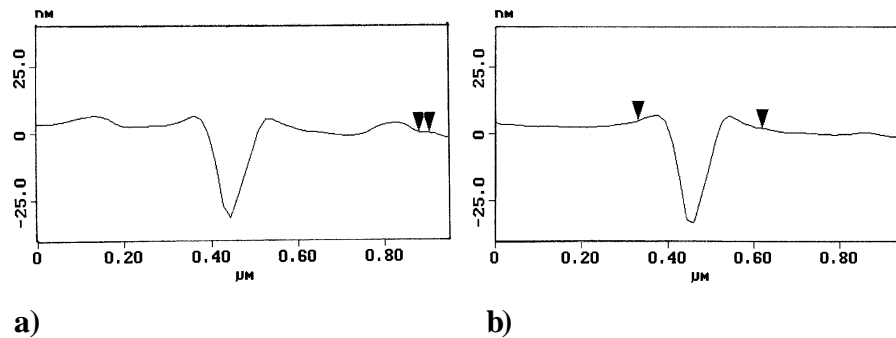


Figure 5.10 AFM section analysis of FIB milled structures using 150 pA beam current and 12,000 \times magnification. **a)** Asymmetric structure with a triangular bottom part. **b)** Asymmetric structure with a sloping flat bottom part.

Magnification 10,000 \times

In the case of observations from magnification 10,000 \times , similar bottoms of the structures as shown for magnification 12,000 \times were observed. In this case the effect is more severe and increase in milled depth starts to decline. Figure 5.11 shows an AFM section analysis of FIB milled structure using 150 pA beam current and magnification 10,000 \times . These observations again support the possibility of Ga precipitation, which becomes more severe with increased milling time.

Saturation in depth milled is measured for the last three readings and one reading shows a lower milled depth than the saturation depth in figure 5.8, this possibly has occurred due to beam current fluctuations. A variation in the width of cut is measured in the first few readings and the last few readings as shown in figure 5.9. This possibly occurs due to beam current fluctuations or it may be the case that Ga precipitation affects the width measurements for the last few readings.

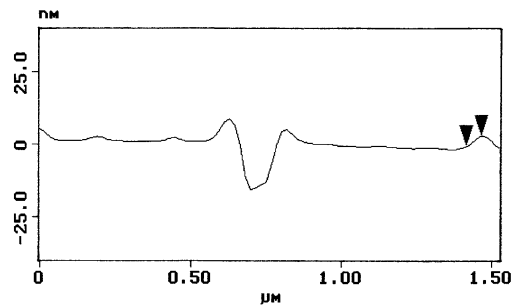


Figure 5.11 AFM section analysis of FIB milled structures using 150 pA beam current and 10,000× magnification.

Magnification 20,000

Figure 5.12 shows two AFM cross-sections of structures milled with 150 pA beam current (magnification 20,000×). As milling time increases an approximately flat plateau forms alongside a triangular cross-section. The width of cut measurements as shown in figure 5.9 decrease with milling time. This particular observation occurred as the framework used for data analysis does not take into account any flat plateau which forms along the milled structure. In the first few measurements as the flat plateau is still forming, the shape is assumed as triangular (with one angle much steeper than the other) so an increase in width of cut was measured. However, in the last few readings as the flat plateau had already formed, the data analysis framework breaks down. As the width of cut measurements due to the framework only included the triangular shape, this resulted in the as shown width of cut decrease in figure 5.9. On the contrary, if the width of the plateau is also added in the last few measurements, an increase in the width of cut with milling time is observed. The last three readings for width of cut including the width of the plateau increase from 107 nm to 112 nm. In this case, Ga cluster formation results in the as observed results, as the effect is most severe it has resulted in low depth milled. At the end of this section different possible mechanisms are discussed that can result in low milled depth and distortions in the shape of the milled structures.

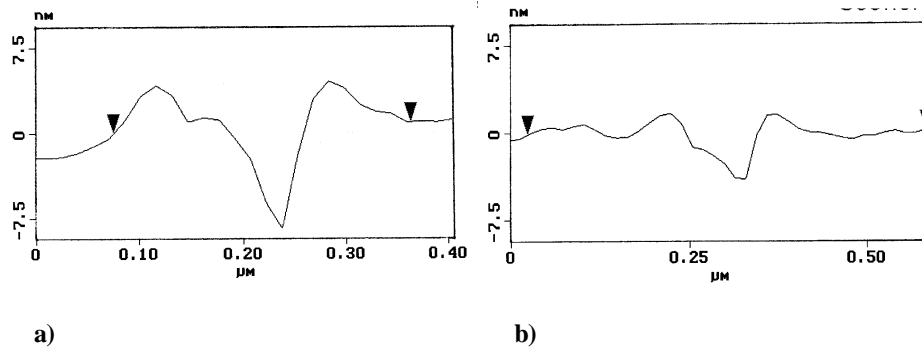


Figure 5.12 AFM section analysis of FIB milled structures using 150 pA beam current and 20,000 \times magnification.

a) Milling time = 0.77 s

b) Milling time = 4.91 s.

Mechanisms

Possible mechanisms by which Ga precipitation can result in the as observed measurements are magnetic effect and electrostatic effect. It is unlikely that drift is magnetic in nature as both Ga and Si are non-magnetic materials. The mass of ions is another factor, which undermines this mechanism. The high mass of ions relative to electrons is the principle reason for using electrostatic lenses than magnetic lenses in the FIB.

The other possible mechanism is electrostatic charge building up in the precipitate rich areas. In the previous work, Ga clusters that resulted in beam drift were observed to be 30 nm underneath the Si [10] and Si above the clusters was amorphous. The actual working of the mechanism may be that the incoming Ga ions lose most of their energy in the Ga precipitate under the Si due to the presence of electrostatic charge and the Si above the clusters having a loose structure. This will lower the sputter yield of the incoming Ga ions thus resulting in lowering the depth milled. Shape distortions of the FIB milled cuts are also expected due to the presence of a non-uniform precipitate. Figure 5.13 shows a schematic of FIB milling of Si and Ga precipitation. As Ga is interspersed with Si, which may change its electrical properties, this seems a probable mechanism. Ga precipitation below the surface of Si also explains that a diffused profile of the cut does not occur, which should have occurred if charge was present on the surface.

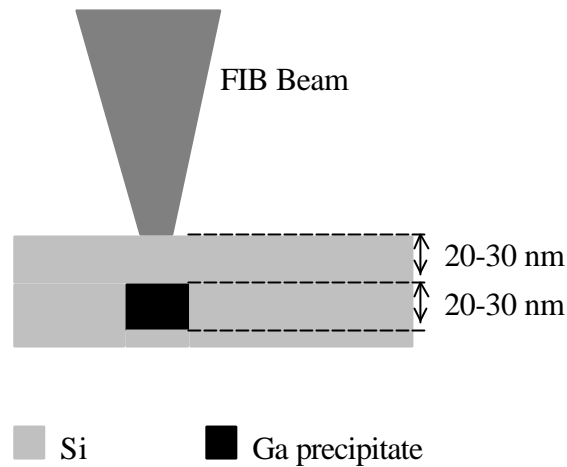


Figure 5.13 Schematic of FIB milling of Si and Ga precipitation. Ga precipitate is shown as having rectangular cross-section only for the purpose of explanation.

5.4.1.2 70 pA Beam Current (Simple Ion Milling)

Simple ion milling was performed using 70 pA beam current with magnifications of 10,000 \times , 12,000 \times , 15,000 \times and 20,000 \times . Figure 5.14 shows an AFM cross-section of a FIB milled cut using 70 pA beam current. The shape of the AFM cross-sections for this beam current are similar to the one shown in figure 5.12 for the case of 150 pA and magnification 20,000 \times . Ga precipitation results in the as observed results; as the plateau observed are not as pronounced in shape as in the case of figure 5.12 b) so beam drift due to Ga cluster formation is not as extreme as in the case of 150 pA beam current and magnification 20,000 \times .

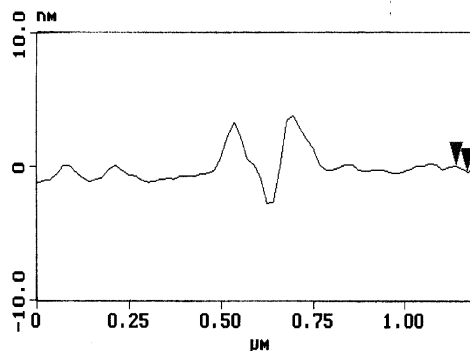


Figure 5.14 AFM cross-section of a FIB milled cut using 70 pA and magnification 10,000 \times .

Figure 5.15 shows depth measurements for this beam current. Every data point shown in figure 5.15 is an average of three readings, this was done in order to improve accuracy. The graph shows variation in milled depth from 2.5 nm to 6 nm for all the four magnifications, this milled depth is comparable to depth milled for 150 pA beam current and magnification 20,000 \times . Ga cluster formation as in the case of 150 pA and magnification 20,000 \times has resulted in the lower milled depth of the structures.

Figure 5.16 shows the width measurements for these beam currents. Width variation of approx. 10 nm was observed so in order to improve the accuracy of the data, an average of five readings was taken to plot every data point shown on the graph. Magnification 20,000 \times results in lower width of cut than other measurements. It has possibly occurred due to fluctuations in the beam current. Width of cut measurements for this beam current does not show a trend of increase in width with milling time which was observed for some width of cut measurements for the case of 150 pA beam current. The presence of Ga precipitates is possibly the major factor, which is resulting in the observed trend of low variation of width of cut.

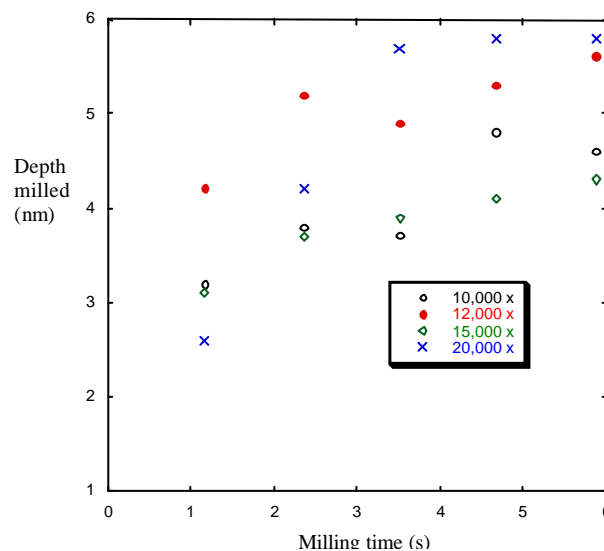


Figure 5.15 Depth of cut against milling time for four magnifications for 70 pA beam current.

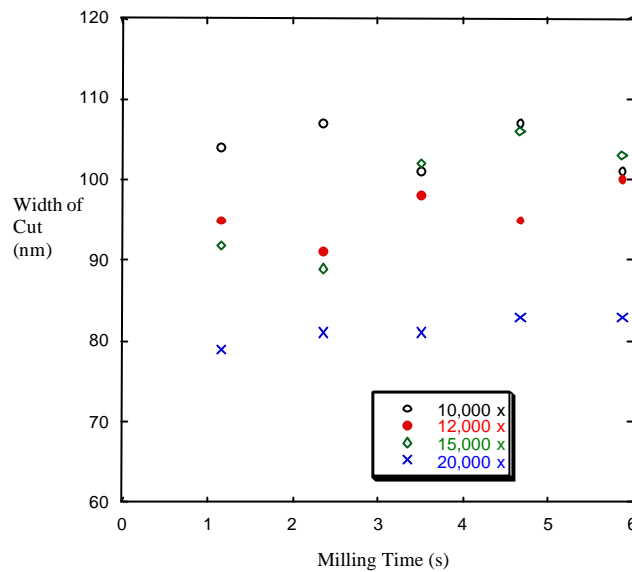


Figure 5.16 Width of cut against milling time for four magnifications for 70 pA beam current.

5.4.1.3 150 pA Beam Current (Enhanced Etch)

Figure 5.17 shows a height image and a section analysis after ion milling with enhanced etch, the milling time increases from the left of the image to the right. The figure shows an initial formation of a deposit and then subsequent milling of it. The width of the deposit ranges approximately between 150 to 250 nm. Figure 5.18 shows a cross-section of a structure milled using the longest milling time with 150 pA EE and magnification 20,000 \times . The shape of the bottom part is different in different cross-sections for example triangular in some cases, however one common observation that can be made is the variation of angle θ . The angle θ is steeper at the bottom part of the structure than in the upper part of the structure. The variation of θ is in the order of a few degrees, however as θ itself is in the region of 5° to 9° the variation is in the order of 10's of %. This variation in θ occurs, as a deposit is present in the upper part of the structure and removal of it results in a wider upper part. Shapes of structures as shown in figure 5.10 were not observed in the case of enhanced etch milled structures, which shows that in this case Ga cluster formation does not occur. Ga cluster formation is also not expected in the case of enhanced etch as Ga forms volatile products with I_2 which are pumped out of the vacuum system.

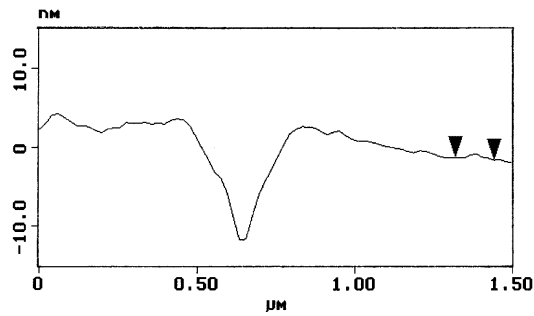


Figure 5.18 AFM cross-section of a FIB milled cut using 150 pA beam current and enhanced etch and magnification 20,000 \times .

Figure 5.19 shows a plot of depth milled for three different magnifications, a variation in the milled depth of a few nm's is observed. Every data point shown in figure 5.19 is an average of three readings, this was done in order to improve accuracy. Due to software related problems data from magnification 15,000 \times could not be analysed, however as magnification 10,000 \times , 15,000 \times and 20,000 \times has similar overlap parameters this does not affect the discussion. Figure 5.17 b) shows the section analysis, in which for the first three readings milling occurs within the deposit and then subsequently milling occurs in Si. The milled depth has been measured from the milled depth within the deposit for the first few readings and then milled depth within Si, which has resulted in first negative milled depth and then positive milled depth. Figure 5.19 shows an increase in the milled depth with milling time for magnification 12,000 \times and 20,000 \times . The milled depth increases approximately linearly with a rate of 3.2 nms⁻¹. An increase in milled depth is observed for the first three readings for magnification 10,000 \times and then no further increase occurs. Magnification 10,000 \times and 20,000 \times has similar beam overlap parameters, the difference in the milled depth has possibly occurred due to fluctuations in the beam current; as the deposit in the case of magnification 10,000 \times was observed to be much less uniform as compared to the cases of magnification 12,000 \times and 20,000 \times . The milling of this non-uniform deposit seems to be affecting the milled depth for the last three readings. However, it is expected for longer milling time, this observed decrease in milled depth will disappear as suggested by measurements from magnification 12,000 \times and 20,000 \times .

Figure 5.20 shows a plot of width of cut against milling time. As a variation in width of cut in the order of 10's of nm was observed, so in order to improve the accuracy

five readings were averaged to obtain each data point. This figure only shows data from the last three depth milled readings as in the first three depth milled readings milling is occurring in the deposit. The width of cut increases with milling time and for magnification 12,000 \times for the last two readings it is approximately constant, which shows that increase in width of cut is occurring due to the removal of the deposit.

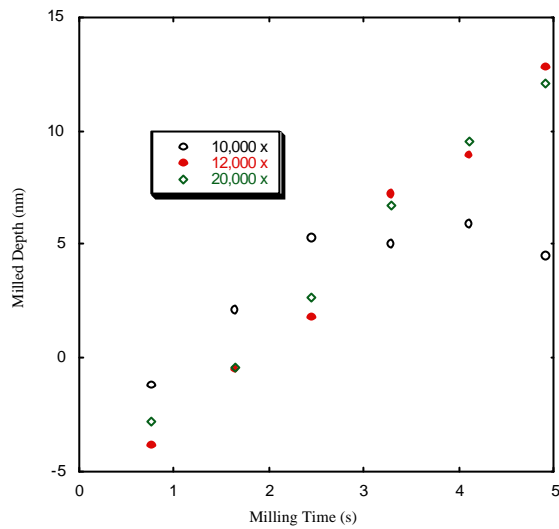


Figure 5.19 Milled depth versus milling time for four magnifications using 150 pA beam current and ion milling using enhanced etch.

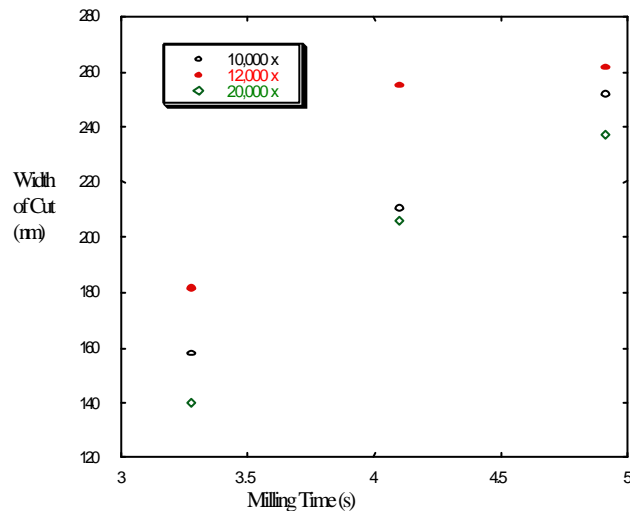


Figure 5.20 Width of cut versus milling time for four magnifications using 150 pA beam current and ion milling using enhanced etch.

Due to the presence of naturally occurring SiO_2 on the surface of Si a deposit is formed on the surface when ion milling is performed with I_2 . The composition of the deposit can not be analysed with EDX analysis as the area from which X-ray signal is generated is in the order of μm , while the deposit width and height is in the order of nm's. The deposit is expected to contain the following atomic species Si, O, Ga and I. In order to find out the exact proportions of the different atomic species and structural properties of the deposit, a technique such as EELS (electron energy loss spectroscopy) should be used.

Figure 5.21 helps to gain better understanding of the observed measurements. The width of the deposit is wider than the width of cut as measured with 150 pA beam current (simple ion milling). This possibly occurs because the generated secondary electrons decompose volatile products formed during enhanced ion milling of SiO_2 . Thus resulting in the formation of deposit further away from the area where milling is being performed. Figure 5.21 assumes that most of the volatile products are present in the area where material removal occurs during simple ion milling.

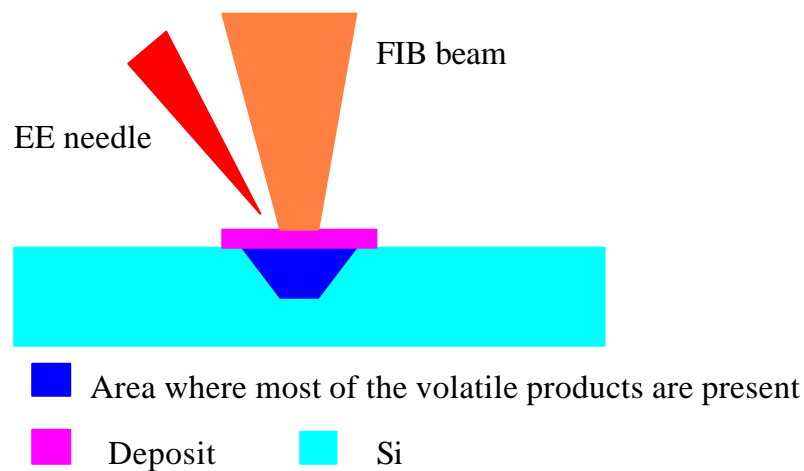


Figure 5.21 Schematic shows deposit, Si *etc.* while FIB milling of Si using enhanced etch.

The deposit formed on the surface of Si during enhanced etch milling has possible applications for FIB lithography. By first forming this deposit on the surface of Si by using low milling times, the specimen can be further processed for example in a reactive ion etching equipment to fabricate nanoscale lines in Si. Chapter 8 discusses this application of the deposit.

5.4.1.4 70 pA Beam Current (Enhanced Etch)

Figure 5.22 shows an AFM cross-section of a structure milled using enhanced etch with 70 pA and magnification 10,000 \times . Similar observations as in the case of milling with 150 pA and enhanced etch were made. There is a variation of angle θ along the structure, which occurs due to the milling of the deposit on the surface.

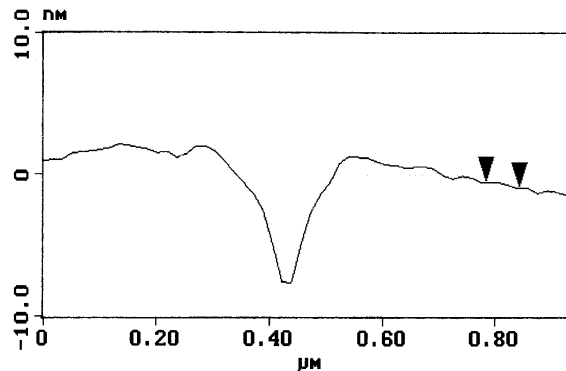


Figure 5.22 AFM cross-section of a FIB milled cut using ion milling using 70 pA with enhanced etch and magnification 10,000 \times .

Figure 5.23 shows the depth milled measured for 70 pA beam current with enhanced etch against milling time for different magnifications. A variation in the milled depth of a few nm's was observed as in the case of 150 pA beam current and enhanced etch so in order to improve the accuracy of the data obtained, three readings were averaged to obtain every data point. A deposit was observed with all the magnifications used with 70 pA beam current, this deposit was milled with increased milling time. Figure 5.23 shows a linear increase in the milled depth with milling time, the milled depth rate is higher for magnification 12,000 \times and 15,000 \times and is equal to 2.2 nm s^{-1} . Fluctuations in the beam current are a possible cause of variation in the milled depth, which has resulted in the formation of less uniform or more uniform deposit.

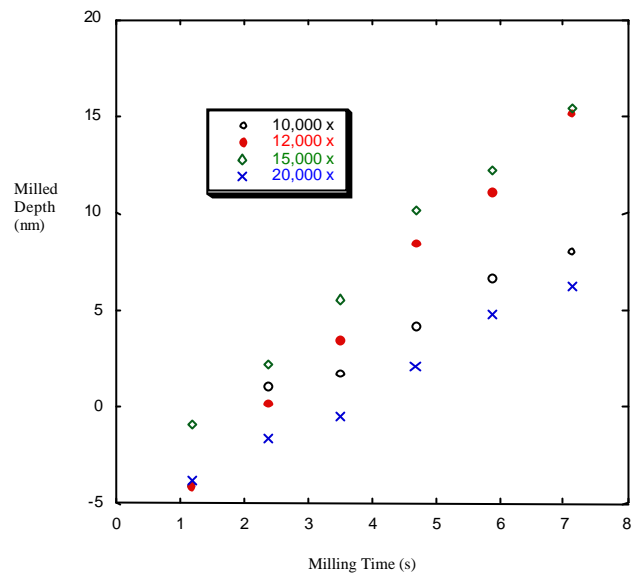


Figure 5.23 Milled depth versus milling time for four magnifications using ion milling with enhanced etch with 70 pA beam current.

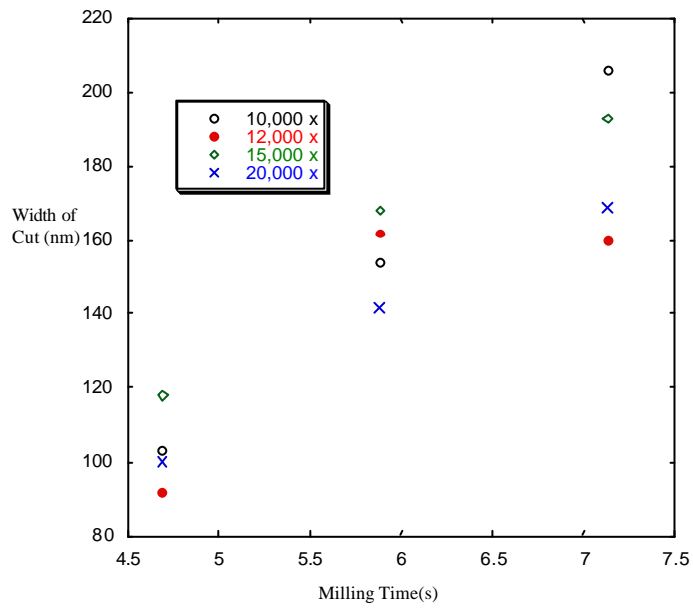


Figure 5.24 Width of cut against milling time for four magnifications using ion milling with enhanced etch with 70 pA beam current.

Figure 5.24 shows a plot of width of cut against milling time. As a variation in width of cut in the order of 10's of nm was observed so in order to improve the accuracy, five readings were averaged to obtain every data point. This figure only shows data from the last three milled depth readings as in the first three milled depth readings milling is occurring in the deposit. The graph shows a decline in increase in the width of cut with milling time. The width of cut for magnification 12,000 \times stays approximately constant for the last two readings. This again shows that the increase in the width of cut is occurring due to the presence of deposit on the surface, as less and less deposit is present on the surface increase in width of cut declines.

5.4.1.5 Comparison Enhanced Etch Milling and Simple Ion Milling (Si)

Figure 5.25 shows AFM cross-section of FIB milled cuts using simple ion milling and enhanced etch with 150 pA beam current. The figure shows the difference in the shape of the milled profile using simple ion milling with 150 pA (magnification 15,000 \times) and ion milling with 150 pA and 70 pA using enhanced etch. Variation of the angle θ is observed in the case of enhanced etch, which is minimal in the case of simple ion milling. This variation occurs due to the formation of a deposit and then subsequent removal of it. The formation of the deposit and the subsequent milling of it result in reducing the mill rate. The milled depth can be possibly improved by using a different material file, which uses a longer dwell time as discussed in the later part of this section.

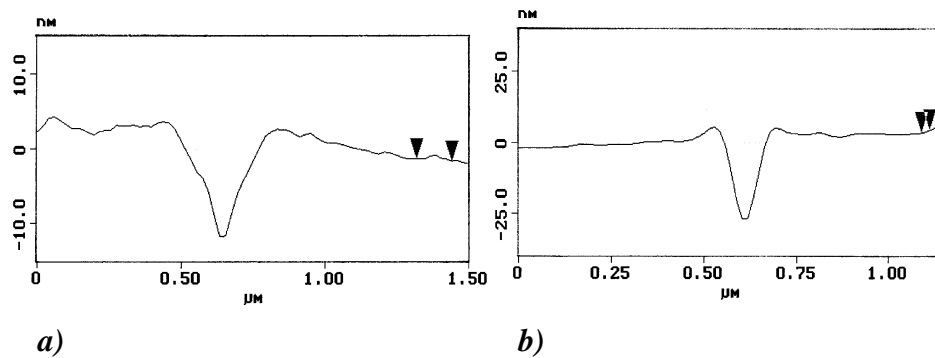


Figure 5.25 AFM cross-sections of FIB milled cuts using *a)* Simple ion milling with 150 pA beam current, magnification 15,000 *b)* Ion milling with enhanced etch using 150 pA beam current.

Milled depth rate with 150 pA (simple ion milling) magnifications 12,000 \times and 15,000 \times is approximately 8 nms⁻¹ (8 nm with bombardment of 9.3×10^8 ions). The highest milled depth rate with 150 pA and 70 pA beam current using enhanced etch rate is 3.2 nms⁻¹ and 2.2 nms⁻¹, which is equal to milled depth of 3.2 nm and 2.2 nm with bombardment of 9.3×10^8 and 4.3×10^8 Ga ions respectively. These milled depth rates show that milled depth rate is lower while using enhanced etch than simple ion milling. As the width of cut is approximately twice in the case when using enhanced etch than simple ion milling, the material removal rate is much higher than as suggested by the milled depth rates. Enhancement was calculated by assuming a triangular cross-section of the milled depth profile. Table 5.5 shows enhancement achieved over simple ion milling using a triangular cross-section in the calculation.

Table 5.5 Enhancement achieved using enhanced etch over simple ion milling.

Beam current (pA)	Enhancement
150	0.8
70	1.2

These are low values of the enhancement achieved, these occur due to two possible reasons: the presence of deposit on the surface and the dwell time. The milling of the deposit interferes with the milling of the Si, which slows down the milling for the first three readings and also seem to affect the milling for the last three readings. The

enhancement achieved using enhanced etch also depends on the size of the structure and milling file used. It is recommended in the FIB manual (1996), to use longer dwell times for small structures such as vias. The material file used for milling single pixel line cuts had a dwell time of 1 μs , which is higher than dwell time of 0.2 μs used for milling large structures with enhanced etch. It may be possible to achieve a higher enhancement with dwell time of 10 μs or even higher.

5.4.2 Width Measurements in Different Materials

Uniformity of the width of FIB cuts is important for different devices and structures such as the channels milled in Si for biochemical analysis [4], and junction length in superconducting devices. A study was conducted on two other materials to determine the important materials properties, which influence the variation of the width of cut. Polycrystalline Nb and an amorphous material ($\text{Co}_{66}\text{Si}_{16}\text{B}_{12}\text{Fe}_4\text{Mo}_2$) were used for this purpose.

The discussion of the results from these materials is only limited to width measurements with 150 pA (simple ion milling). This limitation occurs due to a number of reasons:

- Presence of deposit on the surface of Si when enhanced etch is used.
- The amorphous material forming reactive products due to the use of enhanced etch.
- High milled depth variation in Nb (simple ion milling) due to the presence of grains.

Figure 5.26 shows AFM photographs at high magnification showing the uniformity of FIB cut along the length of the milled structure. Single crystal Si and the amorphous material show uniform width along the length of the structure with variations less than 3-4 nm. Polycrystalline Nb shows a wide variation in the width of cut, with the width of cut

ranging from less than 100 nm to over 200 nm. Figure 5.26 shows that presence of grains in a material result in variation in the width of cut.

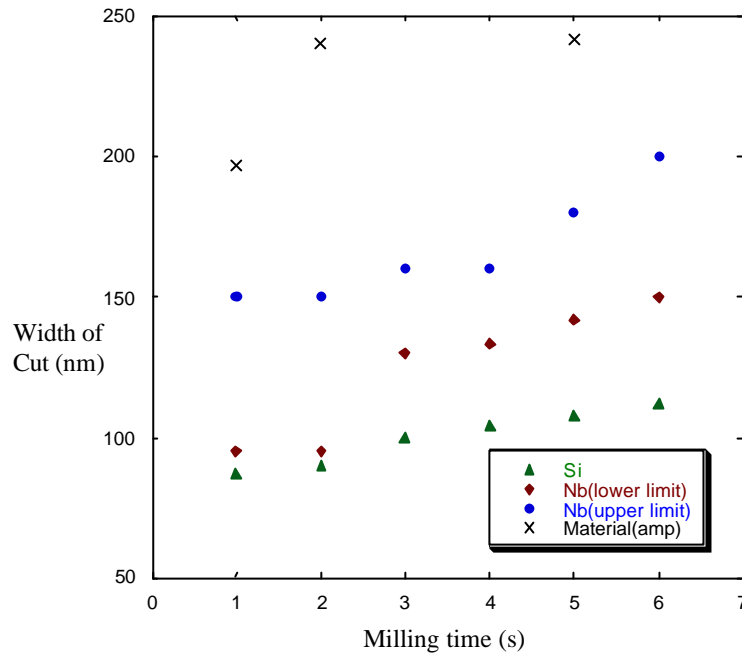


Figure 5.27 Width variation with milling time for Si, Nb and an amorphous material.

Figure 5.27 shows a plot of the width of cut versus milling time for these materials (magnification 12,000 \times). The width of cut is highest for the amorphous materials and lowest for Si. Both Si and the amorphous material do not have grains present within the material, which results in low variation of the width of cut. Nb shows a wide variation in the width of cut, which occurs due to the presence of grains. The graph also shows that the width of cut varies from material to material with the same milling spot size. The incident Ga^+ ions sputters the two materials differently thus resulting in different width of cuts. Figures 5.26 and 5.27 show that improved width of cut variation along the length of the cut can be achieved by using single crystal material or amorphous material. These results are also important for commercial applications for devices fabricated with FIB as fabricating a device with an amorphous material may be cheaper than fabricating a device with single crystal material. These results also demonstrate the need of future work in this field which should be focused to isolate the factors that determine the width of cut in materials for example the bonding strength, the internal structure *etc.*

5.5 Summary

Direct measurements were performed on FIB single pixel line cuts fabricated on three materials in order to identify both the material and technological factors, which influence different parameters such as width of cut. A comparison of different techniques show that AFM technique is best suited for width measurements, it is also suitable for measuring depth of the milled structures and shape of these cuts for low aspect ratio nanometer scale FIB cuts. Different beam currents and magnifications (overlap) were used to mill line cuts, difficulties were encountered ranging from fluctuations in the beam current, beam drift due to Ga cluster formation, different materials forming reactive products with enhanced etch *etc.* Comparison of the width of cut measurements of different material show that the presence of grains results in variation in the width of cut.

5.6 References

1. D. F. Moore, J. H. Daniel, and J. F. Walker, *Microelectronics Journal* **28**, 465 (1997).
2. C. H. Chen, I. Jin, S. P. Pai, Z. W. Dong, C. J. Lobb, T. Venkatesan, K. Edinger, J. Orloff, and J. Melngailis, *Appl. Phys. Lett.* **73**, 1730 (1998).
3. R. W. Moseley, W. E. Booiij, E. J. Tarte, and M. G. Blamire, *Appl. Phys. Lett.* **75**, 262 (1999).
4. C. J. Humphreys, L. C. I. Campbell, I. Marshall, M. J. Wilkinson, P. Camilleri, A. Manz, *Proc. 5th Int. Symp. Advanced Phys. Fields*, edited by K. Yoshiharo (Tsukuba, Japan 2000) p. 41.
5. R. J. Young, *Vacuum* **44**, 353 (1996).
6. J. F. Walker, D. F. Moore, and J. T. Whitney, *Microelectronics Journal* **30**, 517 (1996).
7. N. Yutani, K. Suzuki, and Y. Enomoto, *Jpn. J. Appl. Phys.* **38**, 1375 (1999).
8. P. J. Grundy and G. A. Jones (Chapter 5), *Electron Microscopy in the Study of Materials* (Edward Arnold, 1976).
9. C. R. M. Grovenor, (Chapter 6), *Microelectronic materials*, (IOP publishing, 1989).
10. L. C. I. Campbell, D T Foord and C J Humphreys, *Inst. Phys. Conf. Ser. No 153*, 657(1997).
11. Ryssel H and Ruge I, *Ion Implantation* (John Wiley & Sons, 1986).
12. K. D. Choquette and L. R. Harriot, *Appl. Phys. Lett.* **62**, 3294 (1993).

In order to establish that Ga precipitation is the only reason that results in the as observed measurements all other expected possibilities that may affect measurements are discussed. There are a number of expected reasons that can affect measurements and these are:

- Re-sputtering effects due to different beam overlap parameters for different magnifications.
- Beam drift due to the presence of electrostatic charge, as naturally grown SiO_2 is present on the surface.
- Fluctuations in the beam current.
- Ga precipitation affecting measurements as Ga has low solid solubility in Si.

These different possibilities are analysed in the following paragraphs.

For magnification 10,000 \times and 20,000 \times as the actual beam overlap for both these magnifications is 58%, the depth milled measurements should have been similar to the one for magnification 15,000 \times .

This is not the case so it can be assumed that re-sputtering effects can not explain the wide variation in the depth milled and width variation between different magnification. However, the variation in the actual beam overlap parameters can explain less drastic effects as the slightly different widths of cut and the milled depth of structures for magnification 12,000 \times and 15,000 \times .

, Depth milled and width of cut of structures for magnification 10,000 \times and 20,000 \times should have been similar to the one's for magnification 12,000 \times and 15,000 \times as the actual beam overlap for both these magnifications is 58%. Difference in overlap parameter possibly explains variation in width of cuts and depth milled for magnification 12,000 \times and 15,000 \times , however it does not explain measurements obtained from magnification 10,000 \times and 20,000 \times .

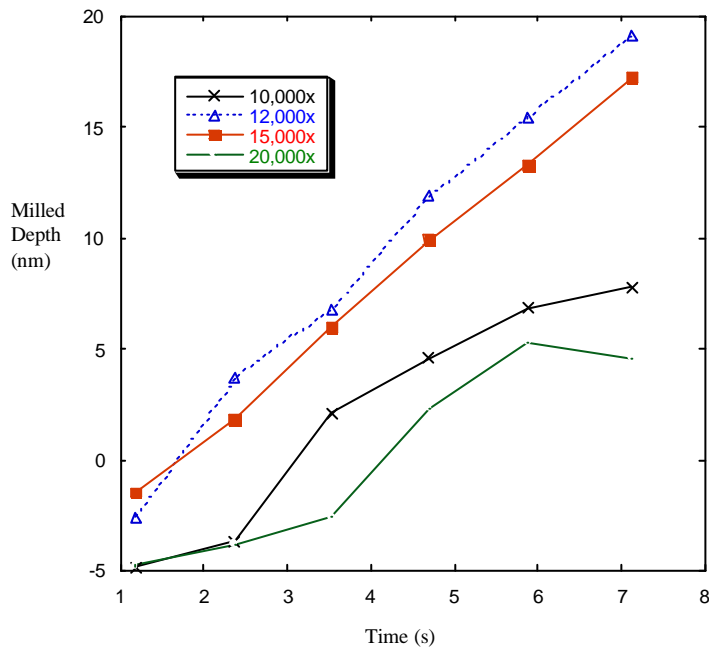
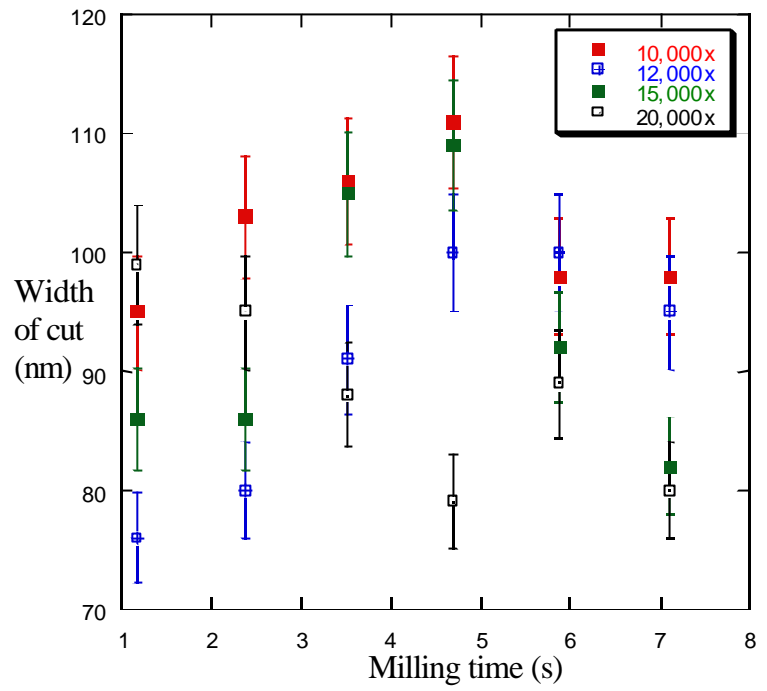
The second possibility is charge building up on the surface thus resulting in beam drift as naturally grown SiO_2 as thick as 2.5 nm is present on the surface [10]. Charging is

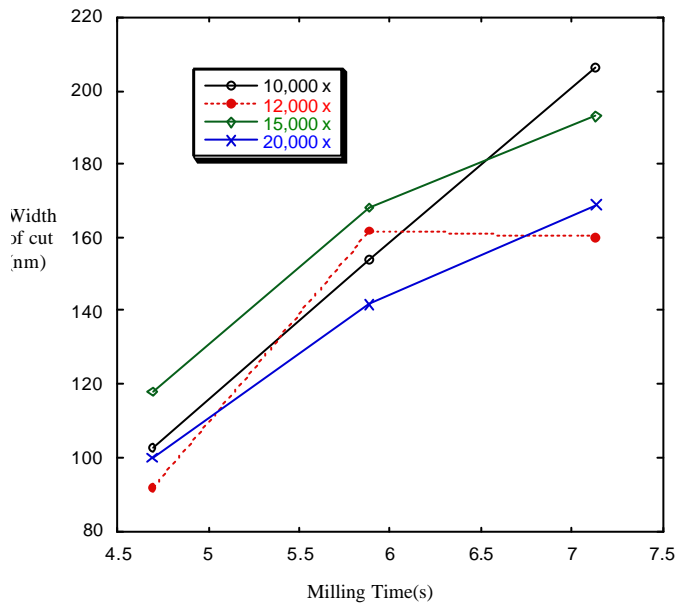
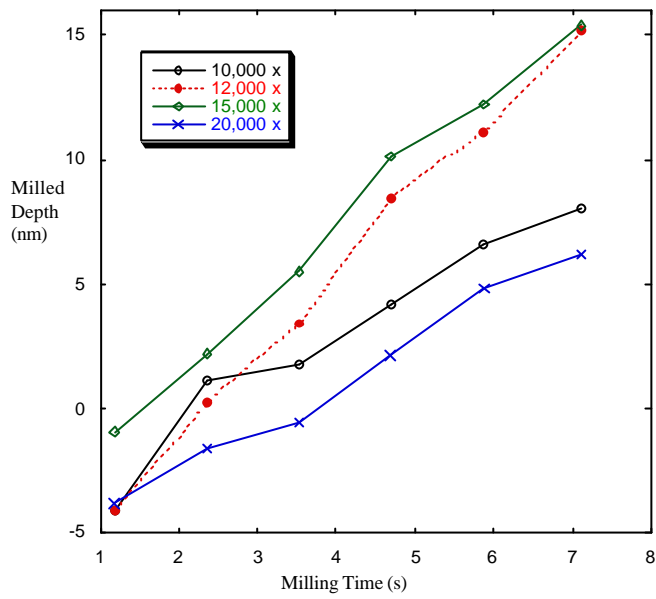
The second possible mechanism by which the observed structures can be explained is the low mill rate of the Ga precipitates. If such a mechanism occurs, Ga precipitates should be directly exposed to the ion beam. As Ga implantation to a depth of 10's of nm is common in materials, Ga precipitation should occur in the range of 10's of nm below the

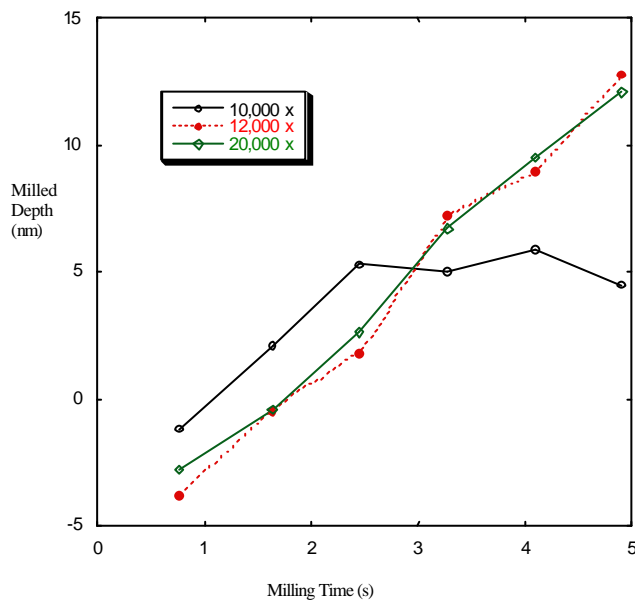
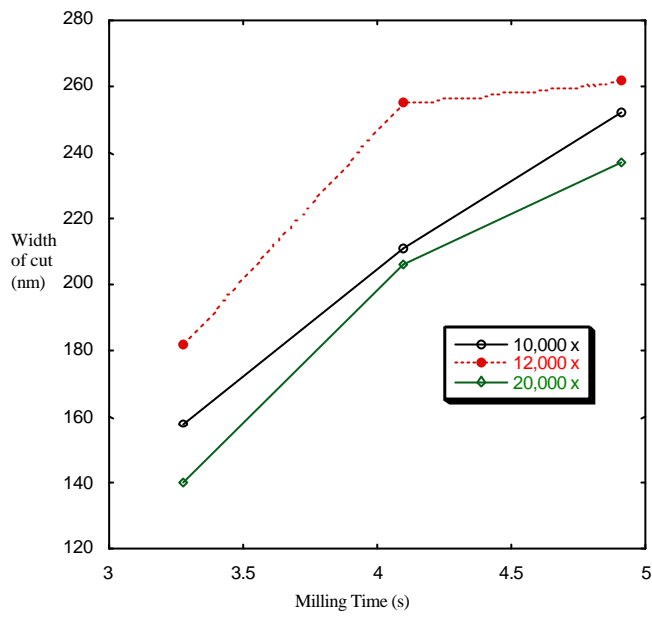
original surface, so depth milled in the order of 10's of nm should be observed. However in the case of magnification 20,000× much lower depth milled is observed.

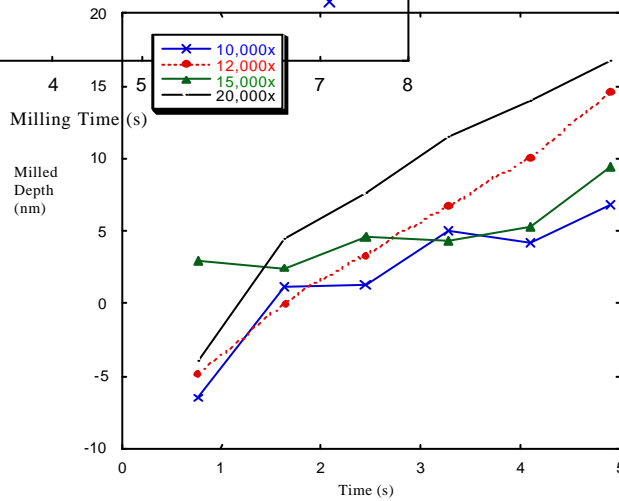
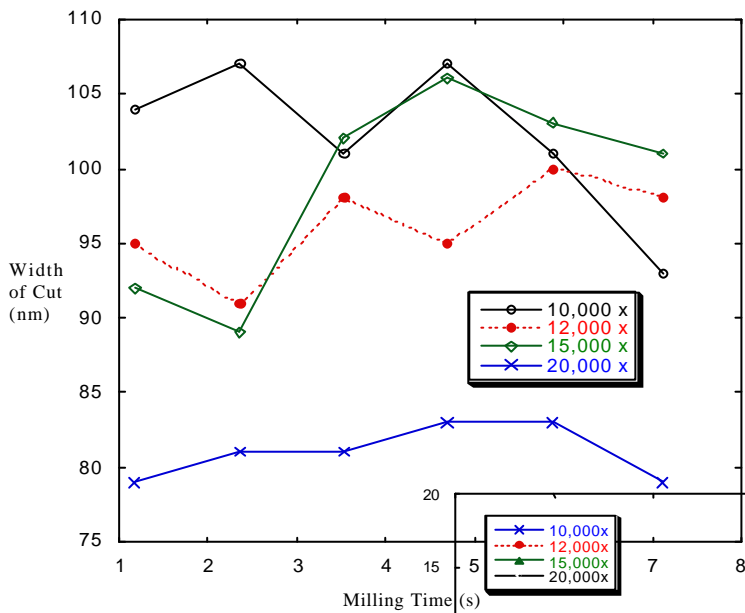
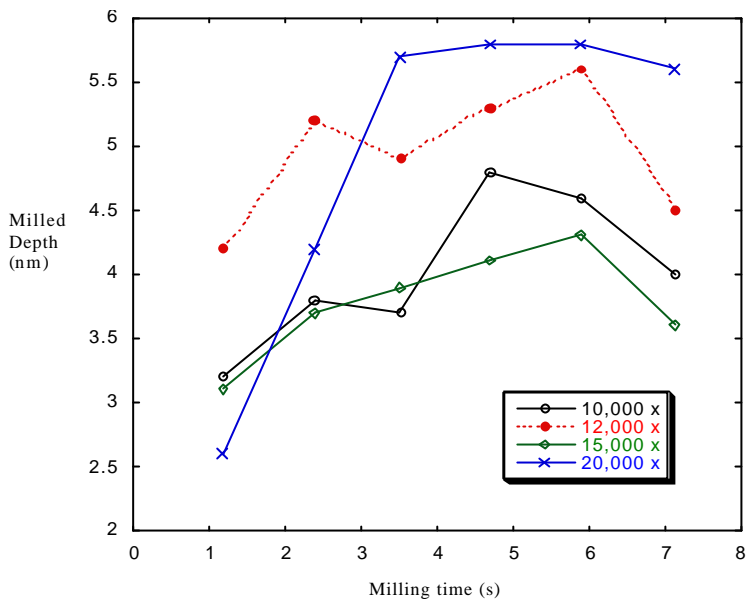
commonly observed in insulating specimen and as SiO₂ is present on the surface of Si, initial expectation may be that it is causing charging and thus resulting in beam drift. SiO₂ has an electric break down strength of $8 \times 10^6 \text{ Vcm}^{-1}$ [10] which can only support approximately 2 V on the surface before breaking down. This can also not be a significant effect to explain measurements as symmetrical AFM cross-sections of structures milled using magnification 15,000× and magnification 12,000× were observed, which can not be explained due to beam drift because of SiO₂. Therefore, charging due to SiO₂ can not explain the as observed measurements.

The third possibility is fluctuations in the beam current, the fluctuations are inherent in the FIB beam current and there is no possible method to remove them. These usually add or subtract a few pA from 150 pA beam, however fluctuations can be 10's of pA. Fluctuations in the beam current may result in different overlaps thus different milled depths but large differences in milled depth and asymmetrical shapes (discussed later in the section) can not be explained due to fluctuations in the beam current.









Chapter 6

Lateral Field Emission Device Fabrication using the FIB

6.1 Introduction

Field emission device fabrication using the FIB is in its early stages of development. FIB processing offers several advantages for on-chip fabrication of lateral field emission devices (in the plane of the chip surface). These advantages include the use of various materials for devices, increase in the sharpness, control over geometry of cathode and reduced anode-to-cathode spacing. These advantages lead to lowering of the turn-on voltage, which is a requirement for fabricating useful field emission devices [1].

Preliminary work showed that it is possible to fabricate sharp Si field emission devices with tip radius below 100 nm with the FIB. This preliminary work was extended and field emission devices were fabricated for electrical testing. Initial measurements showed a leakage current in the order of μA 's from the anode to the cathode of these devices; this was eliminated by modifying the fabrication process. The modified fabrication process utilises the advantages, which FIB offers for the fabrication of field emission devices. Various materials were experimented to fabricate devices as low work function of the material, low sputtering rate and high chemical stability are critical factors for successful field emission devices [2].

The sharpnesses of the devices were measured using FEG SEM and tip radius approximately 50 nm was achieved with Cr using the FIB. Two geometric shapes of the field emission devices were commonly fabricated: rectangular and triangular. Rectangular devices with anode-to-cathode spacing less than 100 nm can be easily fabricated using the FIB. FIB sharpening combined with sacrificial removal of metal may lead in the future to tip radius less than 10 nm.

6.1.1 Applications Difficulties and Fabrication Processes

Field emission is the extraction of electrons out of the surface of a material on the application of high electric fields, which has a history of roughly a century. Wood reported the first observations in 1897 [3]. It was another 30 years before Fowler and Nordheim derived

their equation to explain the phenomenon. In the 1940's and 50's Müller performed pioneering work in the fields of field emission, field emission microscopy and field ion microscopy. During the 1950's, Dyke and co-workers attempted to build useful devices from field emission such as high frequency diodes *etc.*[4]. In the 1960's Spindt, Shoulders and Brodie developed methods to build field emission arrays for displays using microelectronics technology [3,5]. The field emission phenomenon has generated considerable interest, as devices/displays fabricated using this phenomenon are relatively temperature independent and radiation resistant [source: www.pixtech.com]. The field has greatly benefited from developments in vacuum technology and microelectronics technology. Presently there are a number of commercial applications of field emission, today field emission displays are a commercial reality and manufactured using microelectronics technology [5]. Microscopy has greatly benefited from field emission, and field emission tips for both SEM's and TEM's are commercially available. Intensive research work is being carried out to produce other useful devices such as pressure sensor, high frequency devices, high current density devices, and better displays [6-11]. Recently there have been interesting developments in this field in which two different technologies have been combined, for example the development of a pressure sensor required combining field emitter technology with Si membrane technology [6]. In future, this innovative approach will generate more applications of devices using the phenomenon of field emission.

A number of difficulties have resulted in slow progress in the development of new applications using field emission. Difficulties encountered in this area include arcing of the devices, poisoning of the devices and unstable emission (arcing and poisoning are explained in chapter 7, section 7.1) [3,4,12]. Along with these operational difficulties, the requirements for the observation of the phenomenon are very stringent. These requirements are as follows:

- A sharp point required for the enhancement of the electric field.
- UHV required for operation.
- A clean and smooth surface for stable emission and to avoid poisoning.
- A robust material to avoid arcing.

Due to these difficulties and requirements, different researchers focus on one or two aspects of field emission. In general, current research in the field of field emission involves areas such as the fabrication of devices that operate at lower turn-on voltages, production of high field emission currents and stable field emission [1,13].

Materials are of great importance for this field, as properties of the materials determine the ultimate sharpness and smoothness of the surface, the turn-on voltage and arcing [2]. Low work function of the tip material leads to low turn-on voltage of the field emitter and low sputtering rate minimises the occurrence of arcing. A number of materials for example Au, Si, Nb, Pt, Ni, Cr, carbides, nitrides and carbon have been used to fabricate field emitters by various techniques [2,14-21]. Carbides and nitrides lower the turn-on voltage and make the tips robust. Carbon, a new material introduced in this field has resulted in low turn-on voltage and is also robust towards arcing [21]. Field emission tips built with more than two materials have also been fabricated, for example by sputtering of thin films of low work function material on the fabricated field emission tip or by depositing small carbon particles on the tip. The experimentation of new materials is relatively new in this area [2]. The application of field emission for flat panel displays renewed interest in this field and presently drives research in this area [5].

Flat panel displays use the vertical type of emitters, this has resulted in most research work performed on this type of emitter; the lateral type of emitters are also common but are mostly for device applications [1,22-27]. Figure 6.1 shows the most common type of vertical field emitter known as Spindt emitter [5]. In a field emission display, the electrons shoot out of the hole in the gate of the field emitter and strike a screen covered with phosphor to illuminate it. Important considerations for display applications are high emission current, low turn-on voltage and low incident of arcing. The vertical type of field emitter structure is relatively easy to fabricate for diode (two electrodes) on a chip, however the triode (three electrodes) is very complicated to fabricate on chip [12]. The other type of emitter as mentioned above is the lateral field emitter, which is schematically shown in figure 6.2. The use of the lateral type of emitter for displays has also been explored, but presently most uses of the lateral type of field emitter structure are in the fabrication of triode or higher order devices on chips [25]. The applications of the lateral devices due to this reason are different

from the common use of this technology. Multiple-electron-beam lithography and applications requiring focusing of electron beams are the most important applications concerning these devices [28-30]. Presently it appears that these applications will be the greatest driving force for development in this area.

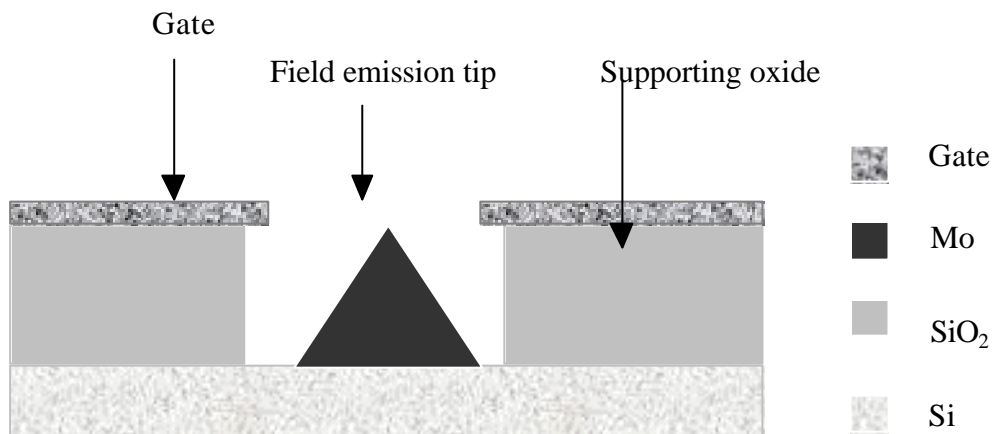


Figure 6.1 Schematic shows cross-section of a vertical type of field emission structure (Spindt emitter).

6.1.2 FIB and Field Emission

Both vertical and lateral type of field emitters can be fabricated with the FIB, different materials such as Pt, Ni, Cr and Si have been used for this purpose [22,26,27,31]. FIB technology offers substantial advantages for the fabrication of lateral field emission structures.

Figure 6.2 shows a lateral type of device, which can be fabricated using FIB. The advantages for fabrication of lateral field emission structures with the FIB are as follows:

- Ease of fabrication for field emission devices consisting more than two electrodes.
- Anode-to-cathode spacing down to 10's of nm.
- Control over sharpness of the tip (discussed in detail in section 6.2.1).
- Ease of fabrication of different geometric shapes of the anode and cathode.

Previous work in the field reports a lateral field emission device fabricated with FIB [22,26], however the device fabricated has the following limitations:

- The fabrication process uses HF, which imposes constraints on the use of materials.
- The study did not investigate the influence of the FIB fabrication parameters on device variable such as sharpening, anode-to-cathode spacing *etc.*

This work overcomes the limitations of the previous reported work and attempts to establish the FIB technique as a viable method for lateral field emission device fabrication.

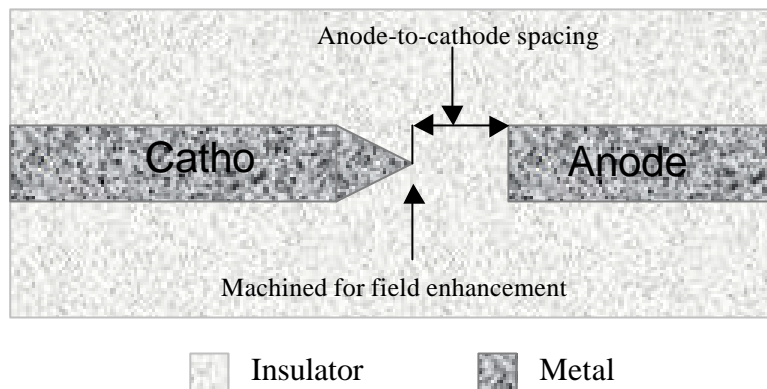


Figure 6.2 Schematic shows planar view of a lateral field emission device.

6.2 Fabrication Process for Field Emission Device

The fabrication process developed throughout the project. Preliminary work was performed to observe the sharpness of field emission tips and different methods to improve the sharpness. Successful observations below 100 nm of the tip led to further developments from building sharper tips to fabricating a field emission device. After selection of suitable materials and overcoming different fabrication related difficulties a successful field emission

device was fabricated. The following sections discuss the work done on the FIB fabrication of the lateral field emission device. Figure 6.3 shows with the help of a diagram the different steps involved during fabrication.

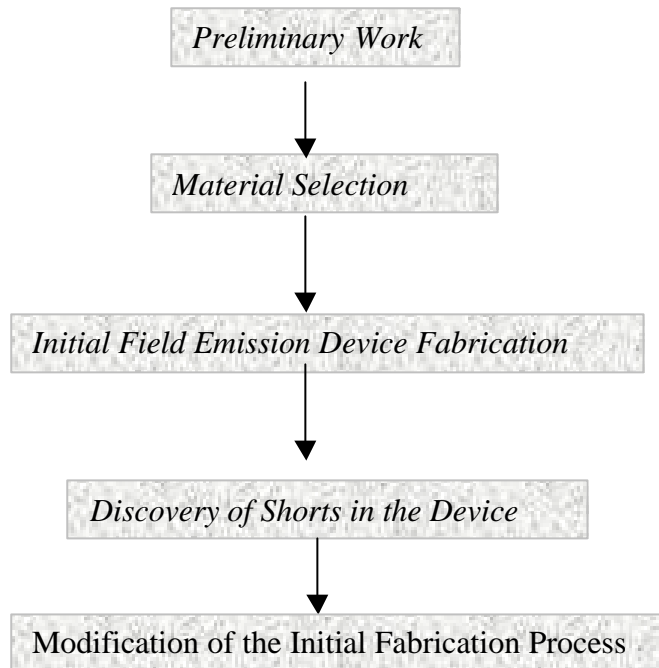


Figure 6.3 Process flow diagram shows the different steps involved during fabrication.

6.2.1 Preliminary Work

As discussed in the chapter 1, FIB offers the unique advantage of oblique cuts in the field of nanofabrication, this can be used to sharpen field emission tips. Preliminary work explored this particular advantage. Oblique cuts were used to mill sharp tips in Si with

approximately 50 nm of Al sputtered on it as sacrificial layer. Figure 6.4 shows a SEM image of the structure after fabrication. The tip sharpness is approximately 100 nm and the edges of the tip are rounded. Figure 6.4 shows that it is possible to fabricate sharp tips for field emission with the FIB. Sacrificial Al layer on Si was later dissolved in KOH solution, which resulted in a tip sharpening; figure 6.5 shows a SEM image after removal of the sacrificial layer. This improvement in sharpness occurs due to the absorption of Ga ions from the periphery of the beam (Gaussian distribution) into the sacrificial layer and later removal of this layer. This sacrificial layer can also be used in other researches involving FIB, where damage to the structure is important.

6.2.2 Materials Selection for Field Emission Device

Selection of suitable materials is of crucial importance for successful operation of field emission devices. The choice of substrate is the first selection to be made. There were three different types of substrates available: oxidised Si, Si coated with Si_3N_4 and silica. Initially all these substrates were used as no particular advantage of any substrate was observed, silica was selected due to being relatively cheap. After the selection of a suitable material for the substrate, suitable material for field emission was selected. Literature survey revealed that Cr and Nb had been used for the fabrication of lateral field emission devices with the FIB [22]. These two materials were initially selected for fabrication due to their ease of sputtering.

6.2.3 Initial Field Emission Device Fabrication

The first step in device fabrication involved sputter deposition of the field emission material Cr or Nb on the substrate. After sputter deposition, lithographic processing was performed which left a pattern of photoresist on the substrate similar to the lithographic mask shown in Appendix 1. The third step of the processing involved reactive ion etching, which etched away the exposed metal thus leaving metal tracks on the insulating substrate after removal of the photoresist. FIB processing was performed on these metal tracks to fabricate the field emission devices. FIB processing involved laying the required pattern on the metal track and milling the track by either simple ion milling or ion milling with enhanced etch.

The difficulties encountered while performing FIB processing and results from the electrical testing of these devices are summarised below:

- Charging of the insulator during FIB processing resulted in continuous image shifting. Charging occurs due to the interaction of the accumulated charge on the specimen surface and the Ga⁺ beam. This accumulated charge discharges sporadically and can damage the detector.
- Electrical testing in the air showed a leakage current in μA range, which occurs due to Ga⁺ implantation into the substrate surface.

The continuous shifting of image results in the loss of control on the FIB fabrication. Shorting is even worse as it makes the device useless. Leakage current in μA range is acceptable in large scale integration (LSI) but for the purpose of field emission where commonly observed current is in the range of nA, this leakage current was unacceptable.

6.2.4 Modification of the Device Fabrication Process

Due to the presence of leakage current and shifting of image the device fabrication process was modified. There are a number of methods to eliminate leakage current and charging. The idea of depositing a conductive layer before fabrication of field emission devices and then latter removal of it was discarded, as it only eliminates charging but does not eliminate leakage current. In the literature this problem has been reported and the authors eliminated leakage current by etching into the substrate material (SiO₂) after FIB processing [22,26]. This approach imposes limitations on the use of materials as the authors report the use of HF. The reported process also does not take into account the flexibility, which the FIB technique offers in controlling device parameters such as anode-to-cathode spacing, sharpness *etc.* Below a process developed during the course of the project is reported, which can be used with various materials. This reported process eliminates both shifting of image during FIB milling and leakage current. As image shifting during FIB milling is eliminated, the FIB technique can be used for field emission device fabrication in a better way.

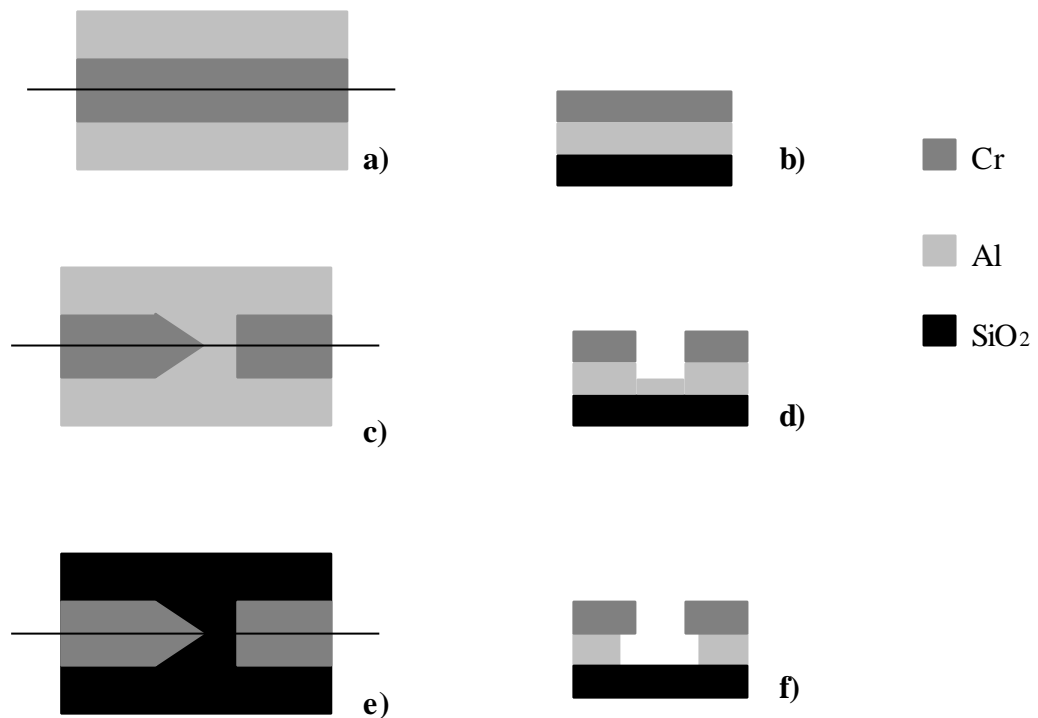


Figure 6.6 Planar and cross-section views of the central part of the chip after sputter deposition of Cr and removal of the photoresist. The black line shows the area from where cross-sections are taken. **a)** Planar view shows Cr and Al layers before FIB milling. **b)** Cross-section view before FIB milling. **c)** Planar view after FIB processing. **d)** Cross-section view after FIB processing. **e)** Planar view after removal of Al with KOH. **f)** Cross-section view after removal of Al with KOH.

In the modified fabrication process a conductive material (Al) was first deposited on an insulating substrate. Al was selected as it dissolves in a weak alkaline solution (in this case KOH). This was the most important criterion in its selection. Other important selection parameters included the ease of sputtering of Al and its common use for FIB milling. Photolithography was performed on Al for the liftoff process using the mask shown in Appendix 1, followed by deposition of field emitting layer. It should be ensured that the field emitting metal should not dissolve in weak KOH solution. After metal deposition by magnetron sputtering the photoresist was washed off with acetone. Figure 6.6 shows the

modified fabrication process after removal of the photoresist. FIB fabrication was used to form lateral field emission structures in the middle part of the chip. During FIB fabrication, all the Ga implantation occurred in Al and no implantation in the substrate occurred as Al was underneath the field emitting layer. Al was later dissolved; the Al layer first dissolved from the areas which were directly exposed to the KOH solution, it dissolved relatively slowly from underneath the field emitting material. By using correct thickness of different materials and careful timing of the process all the Al which was directly exposed was dissolved. This left Cr field emission devices supported by Al. This modified fabrication process resulted in the elimination of leakage current and removal of image shift during fabrication.

As already mentioned in section 6.2.2 two materials, Nb and Cr, were initially selected for fabrication. Due to changes in the fabrication process, a new criterion of dissolution in KOH was introduced. During the later stages of the project, Au was also experimented, it was selected for field emission devices due to its noble character. Table 6.1 summarises the factors for selection, which range from ease of sputtering (related to fabrication) to field emission testing reported in literature. High melting point is important as low melting point can result in localised melting during operation, thus device failure. The FIB milling rate is also important as low ratio of the FIB milling rate of field emitting material to Al can lead to leakage current. Cr satisfied all the requirements for successful device operation.

Table 6.1 Summary of criteria used for material selection.

Material	Reported Field Emission	M.P	Sputtering	KOH Dissolution
Cr	Yes	High	OK	No
Au	Yes	High	Sticking problems	No
Nb	Yes	High	OK	Yes

6.2.5 Final Structure of the Field Emission Device

The selection of suitable materials and appropriate thickness are crucial factors for the success of the modified fabrication process. Appropriate thickness of both Al and the field emitting material is required to ensure that Ga does not implant into the substrate. The thickness of these materials depends on the FIB milling rates of these materials. During FIB fabrication a pattern is laid over the Cr track and part of this pattern also lays directly over some Al on the sides of the Cr track. During milling, the directly exposed Al should not be completely milled away as that will result in direct Ga implantation into the substrate. Ga should not also indirectly implant into the substrate in this area, this may happen due to the penetration of Ga into the Al layer and then implanting into the substrate without milling away all the Al. As the fabrication process is flexible a buffer zone was added to ensure that no Ga implants into the substrate. Figure 6.7 shows a cross-section of the Ga implantation into the various materials during FIB fabrication.

In order to calculate the correct thickness of the various materials involved during fabrication, the following factors need to be considered:

- Etch rate of field emitting material.
- Etch rate of Al.
- Mechanical strength of the field emitting material.
- Width of the track.
- Thickness of the buffer zone.

A 250 nm thick Cr layer was found to have sufficient mechanical strength. Al layer thickness between 600 nm to 900 nm was found sufficient, this created a buffer zone of several hundred nanometers. The thickness of different materials present in different samples varied and needed appropriate changes to milling conditions. The thickness of different materials was confirmed every time by EPD before milling of field emission devices. Figure 6.8 is an EPD graph with different labels on it showing the extent to which Al has been removed. As it has been previously discussed the X-scale on this graph measures depth in μm 's of Si, the labels on the graph are reasonably correct for the purpose of fabrication. The structure after fabrication was tested in air for leakage current. No leakage current was

observed so it was assumed that Ga implantation did not occur into the substrate. Energy dispersive spectroscopy (EDS) analysis was performed to find out the composition of the material between the anode and cathode. Si and oxygen were observed in the case of silica substrate. Figure 6.9 shows a FIB image of a fabricated device, metal deposit (Cr) is observed near the device. This occurred due to the use of a particular fabrication pattern, which is discussed in section 6.3.1. Figure 6.10 shows a FIB image of a device after fabrication. Cr metal from on top of the Al has been partly removed to reveal the structure of the device.

6.3 *Field Emission Device Variables*

The developed device fabrication process leads to control over different device variables such as the materials, the sharpness of the tip, the anode-to-cathode spacing and the shape of the device. This section discusses the experiments performed in order to test the flexibility, which the new fabrication process provides for different device variables.

6.3.1 **Sharpening of the Field Emission Device**

The radius of the tip is defined as the sharpness of the device. Figure 6.11 shows a 2-D diagram of a field emission tip to clarify the definition of sharpness. This parameter is useful as it provides information regarding the emission area. Sharpening of the device lowers the turn-on voltage of the device. Due to this reason, some researchers assume that it is the most significant factor to fabricate useful devices [1]. The assumption arises because most of the field emission device fabrication involve traditional methods such as photolithography and wet chemical etching. By using photolithography and chemical etching it is difficult to fabricate device with anode-to-cathode spacing less than 1 μm [1]. For researchers employing traditional methods, the only method to lower the turn-on voltage is to increase the sharpness and hence it is the most significant factor for them. However, this is not the case when fabricating field emission devices with the FIB. By using FIB, anode-to-cathode spacing can be easily decreased below 1 μm thus reducing the turn-on voltage. This capability of the FIB to lower the anode-to-cathode spacing below 1 μm decreases the relative importance of the sharpening factor. However, the sharpening factor is still an important factor to reduce turn-on voltage, this effect was observed and is discussed in chapter 7. Due to these reasons, a study

was conducted to measure sharpness by SEM technique. Sharpness as measured in SEM can be compared with the information obtained from Fowler Nordheim characteristics and leads to better understanding of the working of field emission devices.

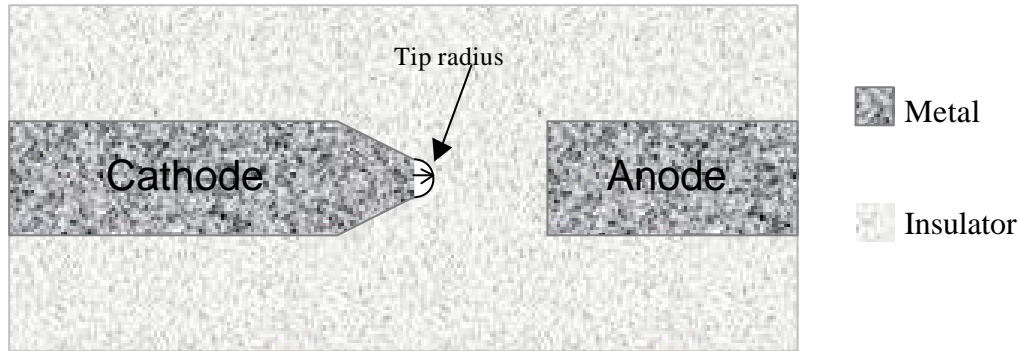


Figure 6.11 Schematic shows planar view of a lateral field emission device and the corresponding tip radius (sharpness).

SEM helped to isolate factors significantly affecting sharpness from insignificant factors. TEM technique is an alternative for this type of study but it was not used for this project as it is time consuming. SEM technique has a few constraints imposed on it due to its operating principle. The electrons from the SEM source needs a path to the ground that can only be provided in the present case by sputtering/evaporating a conductive layer on the completed device, which reduces the sharpness of the ultra-sharp devices. An incomplete device (before removal of Al) can be used for measuring sharpness, this will not require a sputtered film. However, this approach was not used as incomplete devices may have different sharpness due to the chemical processing and cleaning steps involved during fabrication. SEM investigation revealed that several factors contribute to the ultimate sharpness achieved. Factors include the one associated with the condition of the FIB source and beam alignment, which were not in direct control. Factors that were studied and identified to affect sharpness are:

- Beam current and magnification
- Enhanced etch
- Tilt angle

- Milling sequence

The following sections discuss these factors in detail.

Beam Current and Magnification

Variation in beam current is one of the simplest methods to decrease or increase the sharpness of the field emission device. In order to fabricate the sharpest field emission device with a particular beam current, a high enough magnification should be selected as discussed in chapter 5. Logically the lower the beam current the sharper the field emission tip obtained, this occurs due to lower beam currents having smaller milling spot size. However, in practice this can not be done due to the time constraint involved.

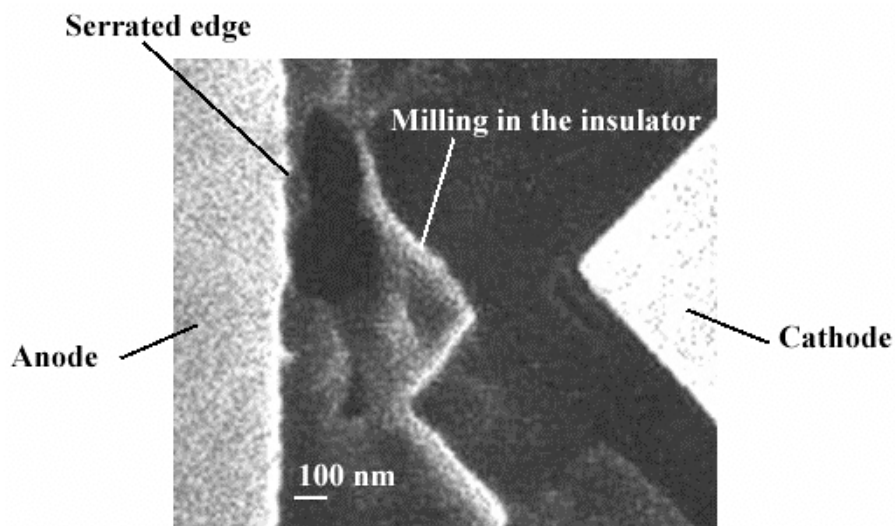


Figure 6.12 SEM image of a field emission device fabricated using simple ion milling, device milled with 70 pA and then sharpened with 4 pA beam current.

In order to fabricate sharp tips in limited time a strategy of first defining the field emission device by a higher beam current and later sharpening it with a lower beam current was used. Figure 6.12 shows a device, which was fabricated first using 70 pA and then sharpened using 4 pA. The device has sharpness of less than 50 nm. The distance between the anode and the cathode was defined using 350 pA beam current. Due to the application of this beam current a

serrated edge of the anode (Cr) is observed. Serrated edge is not observed on the cathode as it was sharpened using 4 pA beam current. No electrical measurements were performed on this particular device.

Enhanced Etch

Enhanced etch is another method by which field emission devices can be sharpened. This method provides another advantage, which is much cleaner surface of the insulator after processing as less sputtered material re-deposits when using enhanced etch. Figure 6.13 shows a SEM photograph of a device, fabricated using simple ion milling with 150 pA and figure 6.14 shows a SEM image of a device fabricated using 150 pA with EE. Figure 6.14 shows much cleaner surface of the insulator between the anode and the cathode due to the use of enhanced etch as it resulted in lack of re-deposition effects. The sharpness of this device was observed to be approximately 40 nm. The sharpness of the device fabricated by 150 pA beam current (simple ion milling) was measured as approximately 100 nm. No electrical measurements were performed on both the devices.

Device Angle(θ)

Figure 6.15 describes the term device angle with the help of a diagram, this term is simply defined as the angle of the cathode. This was the only sharpening factor, which was studied using electrical measurements (see chapter 7).

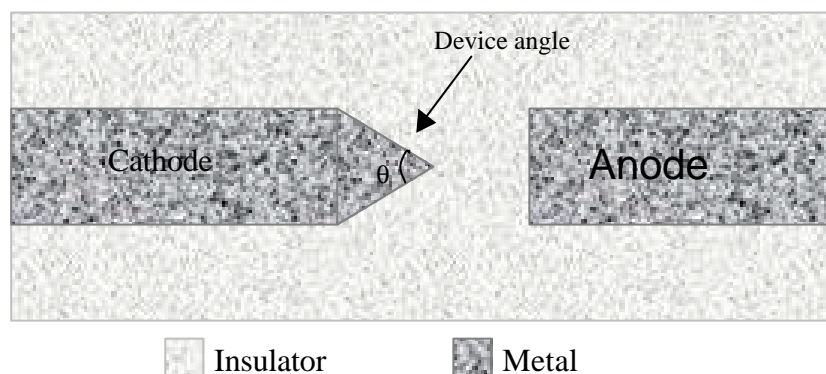


Figure 6.15 Schematic shows planar view of a lateral field emission device showing device angle.

Milling Sequence and Overlap

Two different patterns were used in order to mill the shape of the devices in the FIB. Device was milled in the middle part of the Cr track. Due to difficulties related to photolithography, the track width in this region varied from 4.5 μm to 6 μm . This variation in width resulted in difficulties in the fabrication process, as a standard shape could not be laid over the Cr track for milling. Each device required adjustments in the pattern size before fabrication. The two patterns used for milling field emission devices, overlap of sub-patterns such as patterns for defining anode to cathode spacing and for defining the shape of the device and the corresponding re-sputtering effects are discussed below.

Pattern 1

Figure 6.16 shows the milling sequence used during the early stages of the project, as the FIB machine could not mill triangles. Before milling the Cr track was aligned horizontally as seen on the computer screen by rotating it. In this horizontal position, a vertical cut was fabricated which defined the anode-to-cathode spacing. Then the specimen was rotated from this horizontal position to a fixed angle (half of device angle) and a milling cut was fabricated. After defining this milling cut, the specimen was rotated to the other side of the horizontal position and another milling cut was defined (half of device angle). These rotation movements and milling cuts were performed several times in order to define a field emission device. As FIB could only mill rectangular cuts, a number of millings cuts for defining the shape of the device were required in order to minimise overlap of these cuts with the cut milled to define anode-to-cathode spacing. Overlap was minimised as this can result in shorting the device. The milling was performed sequentially moving from the outside of the track to the inside. This removed the re-deposited material left from the previous steps. If this sequential milling was not used re-deposited material blunted the tip.

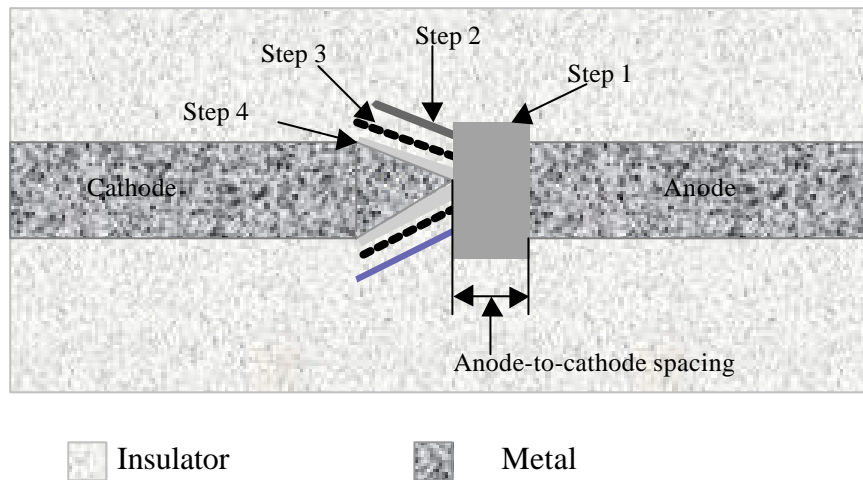


Figure 6.16 Schematic shows planar view of a lateral field emission device showing the different steps of a fabrication process.

Pattern 2

Software developments led to ease in the fabrication of field emission devices as triangular patterns could be defined. Two triangles along with a rectangular pattern were used to fabricate devices during the middle and final part of the project. The rectangular pattern was first defined to avoid sputtered material re-depositing on the tip. This step as in the case of pattern 1 defined the anode-to-cathode spacing and then the two triangular patterns defined the cathode, figure 6.17 shows schematically this device fabrication process. Figure 6.18 shows a blunted tip fabricated by first milling the cathode and then defining the anode-to-cathode spacing.

Tilt

Tilt adds another dimension to the fabrication process and it was incorporated into the fabrication process by adding an additional step to the normal fabrication using pattern 1 or pattern 2 as described earlier in this section. Specimen was tilted after normal fabrication and line cuts were fabricated to sharpen the tip. This strategy cut down milling time and provided control over the re-deposition of sputtered material. SEM observation showed that tilting increased sharpening as compared with normal ion milling (without tilting). This occurs as

tilting fabricates a shape like a ship's hull rather than a 2-D triangle. Tip sharpness of around 50 nm was observed using tilt angle of 45° with 350 pA. This is an increase of 100 % in sharpness over ion milling with 150 pA beam current without tilt.

Sacrificial Layer

The working principle of this layer has been explained in section 6.2.1. It was attempted to fabricate sharper tips using 50 nm of Al as sacrificial layer. Due to this extra Al and relatively high thickness of Al (under the Cr) deposited on the substrate during sputtering the dissolution time to remove all the Al in KOH increased substantially which resulted in Cr removal from the insulating substrate. No further attempts were made to obtain sharper tips by this method, as difficulties were being encountered measuring the sharpness of the emitters in the SEM and due to difficulties involved in electrical measurements. However, the method seems very promising as tips were significantly sharper in the case of Si due to the use of Al sacrificial layer (section 6.2.1).

Summary

Different factors were identified which affect sharpening of the field emission device. The use of appropriate beam current, enhanced etch and tilting are some of the most significant factors. Enhanced etch added complexity to the fabrication process due to the higher enhanced etch rate of Al compared to Cr. Work done on sharpening of the tips provided insight about the working of the FIB technique and increased understanding about important issues such as re-deposition of sputtered material.

6.3.2 Anode-to-cathode Spacing of Field Emission Device

The FIB technique can be used to change anode-to-cathode spacing, device spacing was decreased commonly to 100 nm. However this limits the possibility of fabricating different shapes. The re-deposition of the sputtered material becomes crucially important when anode-to-cathode spacing is reduced for triangular devices to below 500 nm as it shortens the anode to cathode. Simple rectangular cuts and line cuts were used to fabricate field emission devices with anode-to-cathode spacing below 100 nm.

6.3.3 Geometric Shapes of Field Emission Device

FIB can fabricate different shapes of the field emission device. This results in flexibility in the area of field emission for studying the emission properties of different shapes of devices. Two shapes of the cathode were commonly fabricated: triangular and rectangular. Triangular shape of the cathode was used to enhance the electric field at the tip. Difficulties were faced with this shape when it was attempted to lower the anode to cathode spacing to less than 500 nm due to re-sputtering effects. Presently this shape involves at least three FIB cuts and more material removal is needed to fabricate a triangular shaped device relative to fabricating a rectangular shaped device. Rectangular shape of the cathode leads to simplicity in fabrication process as it involves only one FIB fabrication step. This simplicity also results in lowering the anode to cathode spacing without shorting the anode to cathode with the re-sputtered material. This shape is suitable for studying the dependence of anode-to-cathode spacing on field emission properties.

Figure 6.19 shows a shape, which may possibly increase the emission area. In a normal triangular field emission tip, as the electric field is enhanced due to the shape and the distance between the anode to the cathode is shortest between the end of the triangular tip and anode so electron emission occurs from the tip. In figure 6.19 the distance between the anode and cathode is constant, by using a high beam current, serrated edges of the cathode can be fabricated as shown in figure 6.12, which may lead to increased emission area.

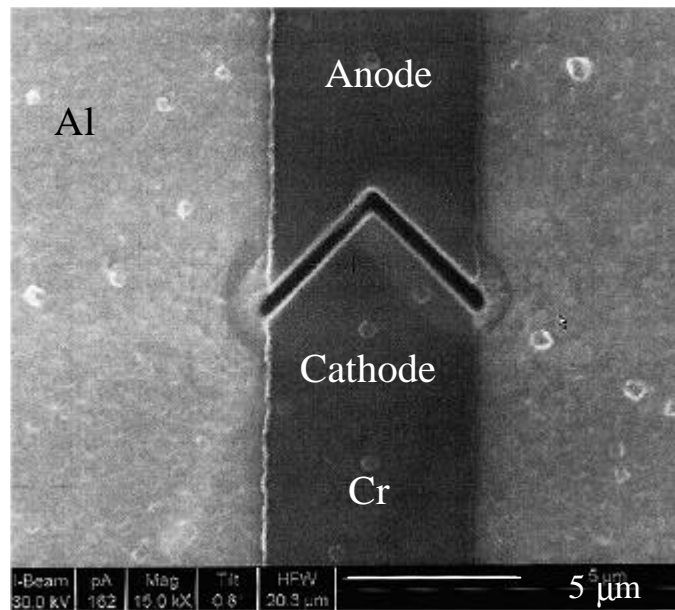


Figure 6.19 FIB image of a field emission device, which can be used to increase emission area.

6.4 Summary

Field emission has a history of approximately 100 years and presently there are commercial applications of the phenomenon. Most notable commercial application is the field emission display. A new lateral field emission device using Cr as field emission material was fabricated using the FIB. FIB offers a number of advantages to this area such as use of various materials, anode-to-cathode spacing below 100 nm and device sharpening. Different difficulties were encountered during the measurement and fabrication of field emission devices, which resulted in slow progress in this field. Ga ion implantation into the surface while fabricating the device with the FIB shorted the device. This difficulty was overcome and modification of the device fabrication process resulted in no leakage current. Device sharpening was observed with an advanced SEM and devices with tip radius below 50 nm were fabricated. FIB was used to vary different parameters of the device such as sharpening, anode-to-cathode spacing *etc.*

6.5 References

1. M. Yun, A. Turner, R. J. Roedel, and M. N. Kozicki, *J. Vac. Sci. Technol. B* **17**, 1561 (1999).
2. J. Ishikawa, H. Tsuji, Y. Gotoh, T. Sasaki, T. Kaneko, M. Nagao, and K. Inoue, *J. Vac. Sci. Technol. B* **11**, 403 (1993).
3. F. Charbonnier, *J. Vac. Sci. Technol. B* **16**, 880 (1998).
4. W. P. Dyke and J. K. Trolan, *Phys. Rev.* **89**, 799 (1953).
5. I. Shah, *Physics World* Vol. **10** No. 6, 45 (1997).
6. S. H. Xia, J. Liu, D. F. Cui, J. H. Han, S. F. Chen, and L. Wang, *J. Vac. Sci. Technol. B* **15**, 1573 (1997).
7. D. Nicolaescu, V. Filip, and F. Okuyama, *Rev. Sci. Instrum.* **68**, 4615 (1997)
8. J. P. Calame, H. F. Gray, and J. L. Shaw, *J. Appl. Phys.* **73**, 1485 (1993)
9. J. M. Kim, J. P. Hong, J. W. Kim, J. H. Choi, N. S. Park, J. H. Kang, J. E. Jang, Y. S. Ryu, H. C. Yang, B. I. Gorfinkel, and E. V. Roussina, *J. Vac. Sci. Technol. B* **15**, 528 (1997).
10. B. Gorfinkel, and J. M. Kim, *J. Vac. Sci. Technol. B* **15**, 524 (1997).
11. E. I. Givargizov, V. V. Zhirnov, N. N. Chubun, and A. N. Stepanova, *J. Vac. Sci. Technol. B* **15**, 450 (1997).
12. H. H. Busta, *J. Micromech. Microeng.* **2**, 43 (1992).
13. E. R. Holland, M. T. Harrison, M. Huang, and P. R. Wilshaw, *J. Vac. Sci. Technol. B* **17**, 580 (1999).
14. P. R. Schwoebel, C. A. Spindt, and I. Brodie, *J. Vac. Sci. Technol. B* **13**, 338 (1995).
15. J. T. Trujillo, A. G. Chakhovskoi, and C. E. Hunt, *J. Vac. Sci. Technol. B* **15**, 401 (1997).
16. W. A. Mackie, T. Xie, and P. R. Davis, *J. Vac. Sci. Technol. B* **17**, 613 (1999).
17. T. Xie, W. A. Mackie, and P. R. Davis, *J. Vac. Sci. Technol. B* **14**, 2090 (1996).
18. M. Endo, H. Nakane, and H. Adachi, *J. Vac. Sci. Technol. B* **14**, 2114 (1996).
19. V. V. Zhirnov, G. J. Wojak, W. B. Choi, J. J. Cuomo, and J. J. Hren, *J. Vac. Sci. Technol. A* **15**, 1733 (1997).

20. S. P. Bozeman, S. M. Camphausen, J. J. Cuomo, S. I. Kim, Y. O. Ahn, and Y. Ko, *J. Vac. Sci. Technol. A* **15**, 1729 (1997).
21. Z. Feng, I. G. Brown, and J. W. Ager III, *J. Mater. Res.* **10**, 1585 (1995).
22. Y. Gotoh, T. Ohtake, N. Fujita, K. Inoue, H. Tsuji, and J. Ishikawa, *J. Vac. Sci. Technol. B* **13**, 464 (1995).
23. A. Kaneko, I. Sumita, H. Kimura, J. Matsuura, and Y. Kondo, *J. Vac. Sci. Technol. B* **13**, 494 (1995).
24. J. Shieh, R. Ren, T. Shieh, D. P. Klemmer, and C. Chen, *J. Vac. Sci. Technol. B* **11**, 501 (1993).
25. J. A. Oro and D. D. Ball, *J. Vac. Sci. Technol. B* **11**, 464 (1993).
26. Y. Gotoh, K. Inoue, T. Ohtake, H. Ueda, Y. Hishida, H. Tsuji, and J. Ishikawa, *Jpn. J. Appl. Phys.* **33**, L63 (1994)
27. J. Ishikawa, T. Ohtake, Y. Gotoh, H. Tsuji, N. Fukayama, K. Inoue, S. Nagamachi, Y. Yamakage, M. Ueda, H. Maruno, and M. Asari, *J. Vac. Sci. Technol. B* **13**, 452 (1995).
28. J. Park, J. D. Lera, M. A. Yakshin, S. S. Choi, Y. Lee, K. J. Chun, J. D. Lee, D. Jeon, and Y. Kuk, *J. Vac. Sci. Technol. B* **15**, 2749 (1997).
29. C. Schoessler and H. W. P. Koops, *J. Vac. Sci. Technol. B* **16**, 862 (1998).
30. I. Honjo, Y. Endo, and S. Goto, *J. Vac. Sci. Technol. B* **15**, 2742 (1997).
31. M. Takai, T. Kishimoto, M. Yamashita, H. Morimoto, S. Yura, A. Hosono, S. Okuda, S. Lipp, L. Frey, and H. Ryssel, *J. Vac. Sci. Technol. B* **14**, 1973 (1996).

Chapter 7

Lateral Field Emission Device Measurements

7.1 Introduction

Electrical testing of the field emission device was performed both in the UHV and in-situ in the FIB. This required building of two new measurement systems, which have already been discussed in chapter 3. Initial electrical measurements in both the systems were noisy, which were later successfully controlled.

Two of the major difficulties encountered while testing of the devices are poisoning and arcing. Poisoning results in the non-operation of the device and arcing destroys the device during operation [1,2]. Poisoning occurs due to poor cleanliness of the tip, which affects the work function of the material for example, due to the formation of oxides on the surface. Different methods such as the use of high quality materials, cleaning the tip surface with plasmas and partial melting of the tip can overcome poisoning. Device failure during operation occurs due to a number of possible reasons for example ionisation of gas close to the field emission tip and then bombardment of the tip with these ions thus destroying it, and poor heat removal away from the field emission tip area thus failing it. The new in-situ FIB system was utilised for low level current measurements in order to address poisoning of devices by removing some material from the tip and then testing it in-situ in the FIB. Material was successfully removed from the field emission tip without shorting the anode to the cathode. A new resistive heater was used to heat up the devices to 100°C in the FIB for some of the field emission tests. Heating removes any adsorbed gases from the surface of the field emission tip, thus it can possibly increase device operation success rate. SEM and EDX analysis were used to study devices failed both in HV (FIB) and UHV, which helped to understand the device failure mechanisms. UHV testing of the devices showed field emission in the picoampere range. Measurements showed device operation of one device at a turn-on voltage of 57 volts.

7.2 Field Emission Theory

Field emission is defined as the emission of electrons from the surface of a condensed phase into vacuum, under the action of a high electrostatic field. For a material with a work function of approximately 4.5 eV an applied field of approximately 10^7 Vcm^{-1} is required for field emission [3]. These high electric fields are reached at reasonable voltages by field enhancement. Machining the emitters into sharp points achieves field enhancement by exploiting the field enhancement factors of shapes of high curvature [3]. Figure 7.1 shows a micromachined lateral field emitter structure in which a dielectric film supports gate (anode) and collector (cathode) electrodes.

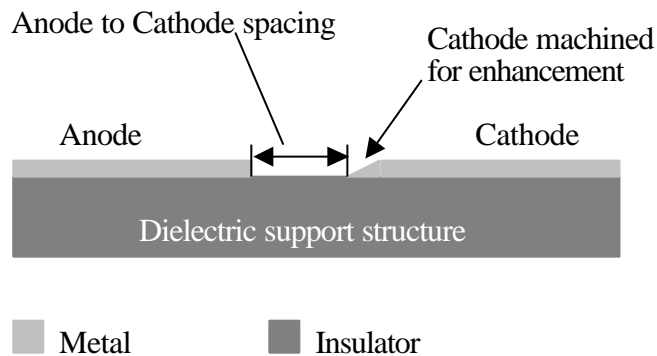


Figure 7.1 Schematic shows cross-section of a lateral field emission device.

Without field enhancement, the dielectric support structures would break down, since their dielectric strength is below $5 \times 10^6 \text{ Vcm}^{-1}$ and a field of at least 10^7 Vcm^{-1} is necessary for field emission [3]. Figure 7.2 shows the energy barrier between a metal and vacuum for two different electric field regimes. The example of thermionic emission clarifies the difference between field emission and thermionic emission and increases understanding. Thermionic emission occurs in a metal when due to heating a sufficient number of electrons acquire kinetic energies greater than or equal to $f + \mu$. f is the work function and corresponds to the energy difference between the fermi level (μ) and field-free vacuum near the surface. In thermionic emission, there is no deformation of the energy barrier. Electrons that acquire sufficient thermal energy from heating can overcome the barrier. However in field emission,

electric field deforms the barrier so strongly that unexcited electron can leak through the barrier. Fowler and Nordheim derived an equation to explain the phenomenon of field emission. The theory has the following assumptions:

- The model is planar.
- Free electron model.
- Classical image correction.
- WKB (Wentzel-Kramers-Brillouin) approximation.

The following sections discuss these assumptions and then present a mathematical derivation. The model calculates the field emission current for temperature approximately equal to 0 K.

7.2.1 Image Force

Image force lowers the height and decreases the width of the barrier which electrons have to overcome to escape into vacuum. Figure 7.3 shows the affect of image effect on potential energy barrier. If a free electron is situated at a distance x , the attractive force that it experiences by its electrical image induced within the metal may be expressed as equation 7.1

$$F = \frac{-q^2}{16\pi\epsilon_0 x^2} \quad (7.1)$$

where q is the electronic charge ϵ_0 is the permittivity of free space and x is the distance from the metallic plane.

The variation of potential energy barrier as a function of x due to this effect is plotted in figure 7.3 a). With the external applied electric field, the potential energy modifies and it is shown in figure 7.3 b) Due to the presence of this image force, the barrier height and width decreases and therefore the tunnel current between the electrodes increases. An image charge lowering contribution term $v(y)$ to the work function is added in the Fowler Nordheim (F-N) equation. The variable y is a non-dimensional function of the applied electric field and it has been calculated by Fowler and Nordheim as:

$$y = \frac{3.79 \times 10^{-4} E^{1/2}}{\mathbf{f}} \quad (7.2)$$

where E is the field at the tip and \mathbf{f} is the work function of the metal. $v(y)$ is calculated from this term and is reported in the literature [4].

7.2.2 Wentzel-Kramers-Brillouin (WKB) Approximation

WKB approximation is an approximate treatment of one dimensional quantum mechanical barrier. The approximation is valid only when the wavelength $\lambda = h/p$ is very short in the classical region and when the potential function changes smoothly, then the index of refraction of the wave varies slowly. Near the classical turning points the approximation breaks down, connectors (Airy function) connects the WKB approximation in the classical and non-classical regions [5]. By using this approximation, a transmission coefficient T can be found as:

$$T = \exp \left\{ \frac{1}{\hbar} \int_{x_1}^{x_2} \sqrt{2m[V(x) - e]} dx \right\} \quad (7.3)$$

where $x_1 \leq x \leq x_2$ is the barrier region, $V(x)$ is the potential energy of the barrier and e is the energy of the particle approaching the barrier

7.2.3 Fowler Nordheim (F-N) Equation

This equation considers the case of a potential barrier in the case of field emission. The wave function is oscillatory outside the barrier and has exponential character in the non-classical region. Due to the external applied field, the potential at the barrier takes the form as shown in figure 7.4 [6-8]. The figure shows the potential barrier across the metal vacuum interface without the image force effect. This potential barrier has a finite width and electrons can escape. The variation of field emission with work function and applied field is easily obtained from equation (7.3). The X-axis has been taken normal to the metallic surface. The electron energies can be expressed mathematically as follows:

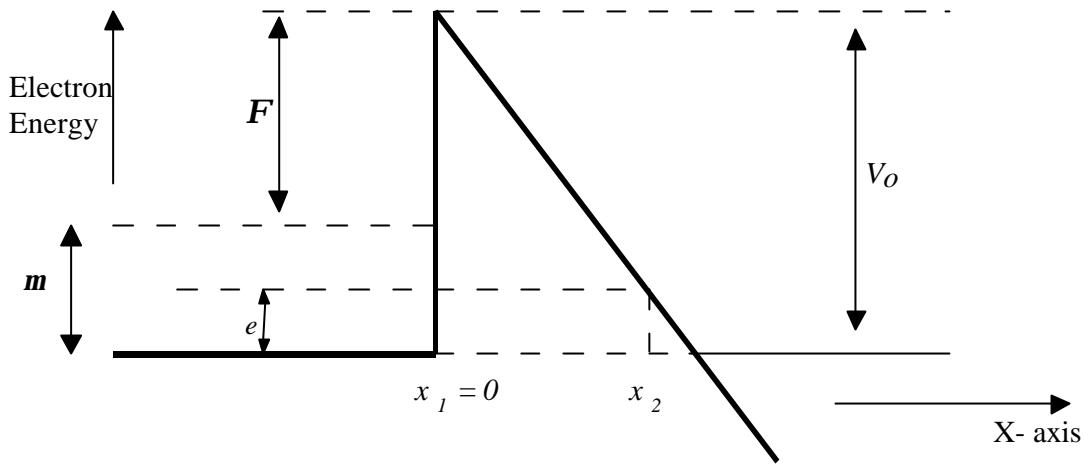


Figure 7.4 A potential energy diagram at the metal/vacuum interface. The diagram shows the different parameters used in the mathematical derivation.

$$\begin{aligned}
 \text{Potential energy} \quad & e_x = \frac{1}{2} m v_x^2 = \frac{p_x^2}{2m} \\
 & V(x) = 0 \text{ for } x < 0 \quad \text{and} \\
 & V(x) = V_o - qEx \text{ for } x > 0
 \end{aligned} \tag{7.4}$$

The electronic tunnelling probability across this electronic barrier is calculated by putting $x_1 = 0$ and $x_2 = V_o - e_x$ in equation (7.3). Therefore, the transmission probability across this barrier is:

$$Z = T^2 = \exp \left[-\frac{4}{3} \left\{ \frac{2m}{\hbar} \right\}^{1/2} \cdot \frac{(V_o - e_x)^{3/2}}{qE} \right] \tag{7.5}$$

Now bearing in mind that the incident carrier density lying within an interval $dp_x dp_y dp_z$ is given by $(2/h^3) dp_x dp_y dp_z$. The number of carriers incident on the barrier surface per unit area and per unit time reduces to $(2/h^3) (p_x/m) dp_x dp_y dp_z$. Hence, the conventional tunnelling current density appearing across the cathode surface follows to be:

$$J = \frac{2q}{m\hbar^3} \int Z(p_x) p_x dp_x dp_y dp_z \quad (7.6)$$

where $Z(p_x)$ is the transmission probability in the x-direction.

The net tunnelling current density is obtainable by integrating equation (7.6) for electrons whose momenta vary between 0 and p_o where $p_o^2 = p_x^2 + p_y^2 + p_z^2 \leq 2m\phi$. Using cylindrical polar co-ordinates $dp_y dp_z = p_\perp dp_\perp d\mathbf{q}$ where $p_\perp = (p_o - p_x)$, equation (7.7) is obtained as:

$$\begin{aligned} J &= \frac{2pq}{m\hbar^3} \int_0^{p_o} Z(p_x) p_x dp_x \int_0^{p_o-p_x} p_\perp dp_\perp \int_0^{2\pi} d\mathbf{q} \\ &= \frac{2pq}{m\hbar^3} \int_0^{p_o} Z(p_x) p_x (p_o^2 - p_x^2) dp_x \end{aligned} \quad (7.7)$$

But $Z(p_x) = Z(p_o - p_x)$ decreases rapidly with increasing p_x . Therefore it can be presumed without any significant error that $(p_o^2 - p_x^2) = (p_o + p_x)(p_o - p_x) \approx 2p_o p_\perp$ (where $p_o \sim p_x$). In addition, it is noted that

$$(V_o - e_x)^{3/2} = [(V_o - e) + e_\perp]^{3/2} = \left[\mathbf{f} + \frac{(p_o - p_x)^2}{2m} \right]^{3/2} = \mathbf{f}^{3/2} + \frac{3}{2} \left(\frac{\mathbf{f}^{1/2} p_o p_\perp}{m} \right) \quad (7.8)$$

By combining 7.5, 7.7 and 7.8, the following equation is obtained:

$$J = \frac{4pq p_o^2}{m\hbar^3} \cdot \exp \left[-\frac{4}{3} \cdot \left(\frac{2m}{\hbar^2} \right)^{1/2} \cdot \frac{\mathbf{f}^{3/2}}{qE} \right] \int_0^\infty \exp \left[-2 \cdot \left(\frac{2m}{\hbar^2} \right)^{1/2} \cdot \frac{\mathbf{f}^{1/2} p_o p_\perp}{mqE} \right] p_\perp dp_\perp \quad (7.9)$$

where, for convenience, the upper limit of p_x has been extended to infinity, because electrons with very large component of perpendicular energy would hardly be able to tunnel out. On integrating equation (7.9) the following equation is obtained:

$$J = \frac{q^3 E^2}{8\pi h f} \exp \left[-\frac{4}{3} \left(\frac{2m}{\hbar^2} \right)^{1/2} \cdot \frac{f^{3/2}}{qE} \right] \quad (7.10)$$

The current of an emitter is given by $I = \alpha J$, where α is the emitting area per tip in cm^2 . It is customary to express the field at the tip by $E = bV$, where b is the field enhancement factor in cm^{-1} , which varies with the shape of the emitter. By using these two terms for current of an emitter and electric field and adding the image correction factor equation (7.11) is obtained:

$$I = a \left(\left\{ \frac{1.54 \times 10^{-6} (bV)^2}{f} \right\} \exp \left(\frac{-6.87 \times 10^7 f^{3/2} v(y)}{bV} \right) \right) \quad (7.11)$$

This equation can be rewritten as:

$$\ln \left[\frac{I}{V^2} \right] = \ln \left[1.54 \times 10^{-6} \frac{ab^2}{f} \right] - \frac{6.87 \times 10^7 f^{3/2} v(y)}{bV} \quad (7.12)$$

Thus, an experimental plot of $\ln(I/V^2)$ against I/V is expected to yield a straight line plot with a slope proportional to $f^{3/2}/b$ and an intercept proportional to b^2/f . From the plot, field emission area and field enhancement can be obtained by assuming a suitable value for the work function.

7.3 Field Emission Measurements

Filed emission devices were tested for field emission both in the FIB chamber and in the UHV. An electrical power source applied voltage and different electrical circuits performed current measurements. The measurement system and different circuits used for measurements are described in chapter 3. Field emission tests were performed in the FIB to address poisoning of the devices. FIB offers the unique possibility of in-situ cleaning of the field emission devices by ion milling and in-situ testing. Field emission was observed in UHV in the picoampere range. The emission range is surprisingly low even though the tip radii observed in the FEG machine are relatively large (approximately 50 nm). Electrical measurements showed device operation of one device at a turn-on voltage of 57 volts.

7.3.1 In-situ FIB Experiments on Field Emission Device

Poisoning and unstable behaviour of field emission devices occurs due to various reasons. Localised deposit of an impurity on the field emission tip is one of the major reasons. In practice, the removal of this deposit is performed by different methods such as plasma cleaning of emitters or localised melting of the tip *etc.* In-situ FIB electrical measurement system offers the possibility of cleaning the tips by locally removing some material and then testing. Emitters can be cleaned using ion milling and then tested in some other equipment, however, this method exposes tips to air. This is particularly important for materials that form surface oxides with atmospheric gases. As the emitters were fabricated using Cr which has a native oxide film, the removal of some material with the FIB reveals Cr without an oxide layer, and in-situ testing of these emitters will result in new knowledge about the emitter properties. This advantage of the FIB led to testing of these devices in-situ in the FIB after cleaning.

The cleaning and testing of the devices poses various difficulties, the difficulties encountered during in-situ FIB testing ranged from construction of a low level current measurement system to device failure because of arcing in high vacuum. The electrical measurement method used for these observations has been discussed in chapter 3. As FIB operates in high vacuum, Cr field emission device operation in high vacuum caused device arcing. Failed devices were observed using both FIB and SEM, and materials analysis was performed on these devices. Different reasons have been provided in the literature for device failure; SEM observations support two mechanisms these are discussed in section 7.3.2.

7.3.1.1 Measurements

Material was successfully removed from the cathode without shorting the device. This was performed using line cuts, however low level current measurements in the FIB posed various difficulties (discussed in chapter 3). Along with the measurement difficulties, observation of failed devices were commonly made. A spike of relative high current was observed with the failure of the device. The devices seemed to fail by the initial formation of plasma in high vacuum, followed by spraying of molten metal from the anode to the cathode (Section 7.3.2

discusses this in detail). A number of different experiments were performed to stop this failure of devices:

- A new heater was designed to operate inside the FIB, the devices were heated and tested at approximately 100°C. Heating removes any adsorbed gases on the surface, which is a possible cause of arcing.
- The tip area was scanned with Ga ion beam to remove any adsorbed gases.
- Cuts were fabricated to generate a new surface for emission, these cuts removed the oxide from the surface of Cr and also removed any adsorbed gases which can cause arcing.
- Pt metal was deposited on top of the tip to make it more robust.
- It was attempted to anodize Al underneath the Cr in order to minimise the exposed metal thus increasing the success rate. Anodization is a promising new method in this field.
- Devices were cleaned using Ar ion milling to remove any material deposit occurring due to chemical processing.
- Devices were cleaned using O₂ plasma to remove any organic deposit from the surface.

These preliminary experiments showed that material removal from the tip before in-situ FIB testing did not short the anode to the cathode (no leakage current was observed). Considerable technical knowledge was gained while performing these experiments.

7.3.2 Arcing and Poisoning

While performing field emission experiments, failure of devices occurred along with successful operation of devices. An in depth study of failed devices was conducted in order to design devices with a high success rate. This study was used during the course of this project to design better devices and resulted in two new ideas to improve device performance: anodization and chemical displacement (discussed in chapter 3). These two ideas may prove to be highly valuable for the area of field emission.

Table 7.1 summarises the results of devices both measured inside the FIB chamber and in the UHV. The first row is for devices tested in the UHV chamber and the second row for the devices tested in the FIB chamber. Table 7.1 shows that the quality of the vacuum is one of the most significant factors affecting the number of failed devices. This relationship

between the vacuum conditions and failed devices is further strengthened by the observations of failed devices in the FIB and SEM. Table 7.1 does not show a relationship between the number of poisoned devices and the vacuum conditions.

Table 7.1 Relationship of device performance with the vacuum conditions used for testing of field emission devices.

No. Tested	No. Successful	No. Failed (during operation)	No. Poisoned	Vacuum
20	5	11	4	10^{-7} to 10^{-9} mbar
29	0	22	7	10^{-6} to 10^{-7} mbar

All the devices, which failed in the FIB, showed a typical shape. Figure 7.5 shows a FIB image of such a device. The main features of this typical shape are:

- A white contrast from anode-to-cathode, which is in the shape of arcs.
- Destruction of both the anode and cathode.
- Cathode is more severely destroyed than the anode.
- No white contrast directly between the anode and cathode.

The white contrast observed in the FIB was imaged in advanced SEM and it was discovered to be composed of tiny droplets of 10-20 nm size (figure 7.6). These droplets were very difficult to image in the SEM and were observed to have a preferential shape and seem to fly sideways. EDS analysis was performed on different regions of the failed device and the tiny droplets were discovered to be a mixture of Al and Cr. No Al/ Cr could be detected

directly in between the anode and cathode. No droplets of metal were observed where the electric field strength was strongest (in between the anode and cathode).

Inside the FIB chamber the devices are in high vacuum and the number of gaseous molecules close to the surface of the cathode are higher than as compared with devices tested in UHV. During operation of the devices in the FIB chamber the gaseous molecules close to the sharp edges of the cathode bombard it and ionise some material. This ionised material due to the electric field bombards the other electrode and generates more material. This process continues until the metal droplets, which falls to the sides (figure 7.5 and figure 7.6), shorten the anode to cathode. Because of this shorting the electric field drops which stops this arcing process. No material in between the anode and cathode was observed, as the electric field was strongest in the area, which resulted in the preferential removal of material from this area.

Device failure in the UHV was also studied and figure 7.7 shows a FIB image of a failed device. This is one of the devices from chip # 56, which failed during operation, no field emission characteristics of this device are reported in this report. This image shows that the device failure occurred from the tip of the field emission device. The image also confirms that field emission occurs from the tip of the field emission device. The image shows localised damage and the damage occurs only where the electric field is highest. In the case of UHV testing of the devices the device failure mechanism is different, device failure occurs due to localised melting of the material. The localised melting of the material occurs due to insufficient removal of heat away from the field emission tip.

Figures 7.6 and 7.7 provide important information regarding the different reasons of failure. In the case of UHV testing device failure occurs due to insufficient removal of heat away from the field emission tip. Consequently in UHV, the use of materials that are better thermal conductors may improve device success rate. In the case of HV testing (inside the FIB), device failure occurs due to ion bombardment. Therefore in HV, materials with high resistance to sputtering may result in increasing device success rate.

7.3.3 Testing of the Field Emission Device in UHV

Field emission devices were successfully tested in UHV. Two different substrates were used, namely SiO_2 and Si_3N_4 , while performing these measurements. The field emission devices were prepared using pattern # 1 for fabrication (see chapter 6 for detail). Table 7.2 summarises information regarding substrates, milling pattern *etc.* Both chips were examined using optical microscope before and after electrical measurements for any broken tracks, broken devices, particles on top of the device *etc.* Failed field emission devices were studied with the help of the FIB and SEM.

Table 7.2 Summary of the different conditions used during fabrication and measurements.

Chip#	Substrate	Thickness of Cr (nm)	Beam Current (pA)	Milling sequence	Device angle	Pressure (m bar)
34	Si_3N_4	110	350	1	72°	1×10^{-9}
56	SiO_2	140	350	1	60°	1×10^{-9}

7.3.3.1 Measurements on Chip # 34

Figure 7.8 shows electrical characteristics of four similar devices. Data was recorded from 15 volts to 135 volts for all these measurements. Two different geometrical shapes of field emission devices were fabricated on this particular chip: a triangular shape and a rectangular shape. The rectangular shape did not show any field emission characteristics, however it showed a leakage current increasing from 1.7 pA at 15 volts to 4.6 pA at 135 volts. This leakage current was subtracted from the emission characteristics of the devices that operated hence providing more accurate data. As the rectangular device did not show device characteristics similar to the device characteristics shown by the triangular devices, it is reasonable to assume that the observed electrical characteristics are not due to effects such as doping of Si_3N_4 *etc.*, and field emission is being observed. The case for the field emission is further supported by the observation that not all the triangular shapes fabricated on this chip showed field emission characteristics; two did not operate.

In figure 7.8, the curve is divided into two parts for discussion. The first part has been taken from zero to 85 volts. Generally, a slow increase in current is observed along with some fluctuations. The second part starts from around 85 volts up to the limits of the observation; an exponential increase in current is observed. The lower values of current in the first part of this curve may have occurred due to contacts for example re-sputtered material, crocodile clips and the screw type of contacts used inside the UHV system *etc.* Various factors discussed in chapter 3 may also have resulted in noise. The second part of the curve shows a diode-like behavior, which is commonly associated with field emission.

According to Fowler Nordheim theory, a plot of $\text{Log}(IV^2)$ versus I/V should be linear. Measurements above 85 volts were taken in to account while plotting figure 7.9. The plot is non-linear, this could have occurred due to a number of possible reasons. As there is leakage and noise current present in the measurements these are possible causes of this deviation from linearity. Another possible reason is the assumption of a planar model during the derivation of Fowler Nordheim theory. It is possible that the emission area is very small so the assumption of the planar model is not correct for these measurements.

7.3.3.2 Measurements Chip # 56

Figure 7.10 shows FIB image of the device on chip # 56, which showed field emission characteristics. The image shows that the device has serrated edges, however the emission does not occur from the serrated edges, as failure in one of the devices from this chip occurs from the field emission tip (figure # 7.7).

Figure 7.11 shows electrical characteristics of the device shown in figure 7.10. This graph shows two parts: in the first part from zero to 57 volts, there is no increase of current as voltage is increased. In the second part above 57 volts, there is an exponential increase in current. In this particular observation, no background noise and leakage current was observed which indicates absence of any re-deposited material forming any current paths, good electrical contacts and other possible sources of noise for example due to vibrations of wires *etc.* being absent. Figure 7.12 shows Fowler Nordheim plot, which is linear. The value of β

factor is $2.98 \times 10^5 \text{ cm}^{-1}$ assuming field strength at the tip of around $3 \times 10^7 \text{ Vcm}^{-1}$ and α factor equal to $1.6 \times 10^{-6} \text{ cm}^{-2}$.

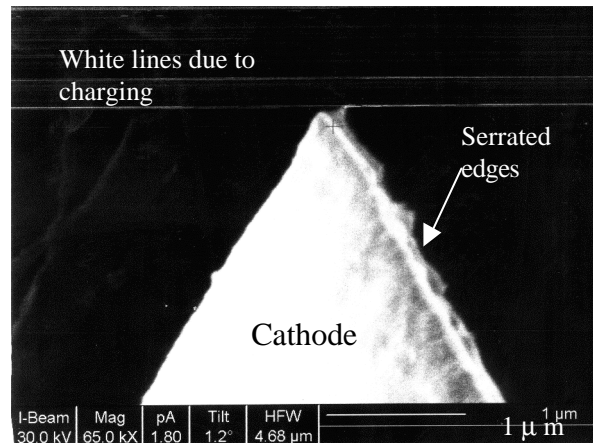


Figure 7.10 FIB image of the device which showed field emission characteristics on chip # 56. Image was taken after performing field emission measurements.

7.3.3.3 Comparison and Discussion

Figure 7.13 compares the electrical characteristics of devices from both chips. The plot shows that the turn-on voltage of device on chip # 56 is approximately 27 volts lower than the turn-on voltage from device on chip # 34. This is a very significant improvement in the turn-on voltage which has occurred due to the sharpening of the device as the device angle decreased from 72° in chip # 34 to 60° in chip # 56. The plot also clearly shows the effects due to re-sputtered material, noise and leakage in the device from chip # 34. After turn-on the increase in current is more drastic in device on chip #56. The calculated value for β factor from device on chip # 56 are in agreement with those reported by another researcher [9] for tip radii in the range of 50 nm. Observations of the field emission current from chip # 56 showed a very erratic behavior. Sudden surges of current were observed at around 60 volts. These surges possibly occurred due to the localized ionization of some material from the tip due to the presence of surface deposits or oxides.

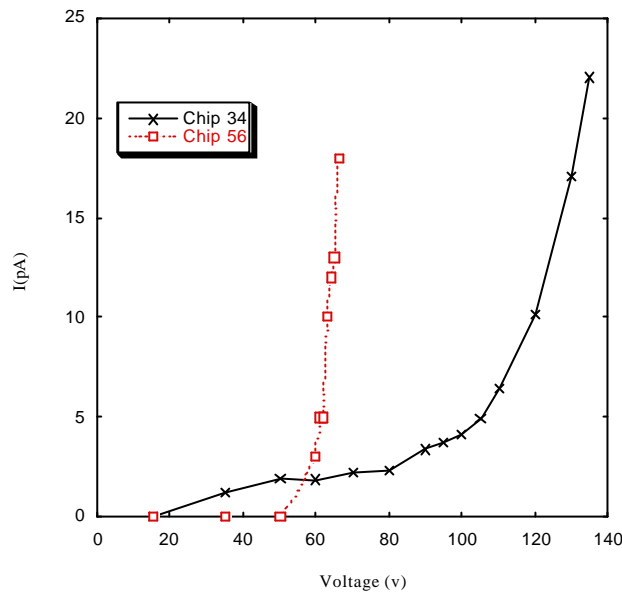


Figure 7.13 Electrical characteristics of a device each from chip # 34 and 56.

Comparison of figures 7.9 and figure 7.12 (Fowler Nordheim plots) shows that in the case of chip # 34 the plot is non-linear, while in the case of chip # 56 a linear plot is observed. The non-linearity in the case of chip # 34 was discussed in section 7.3.3.1 and different possible causes were identified: leakage current, noise and the assumption of planar model breaking down. The thickness of Cr used in the case of chip # 34 is 110 nm while it is approximately 140 nm for chip # 56. It is possible that even though the device angle in the case of chip #56 is smaller relative to chip # 34 but due to decreased Cr thickness for chip # 34 has resulted in an overall decrease in the emission area. This decreased area has resulted in the break down of the assumption of the planar model in the Fowler Nordheim equation.

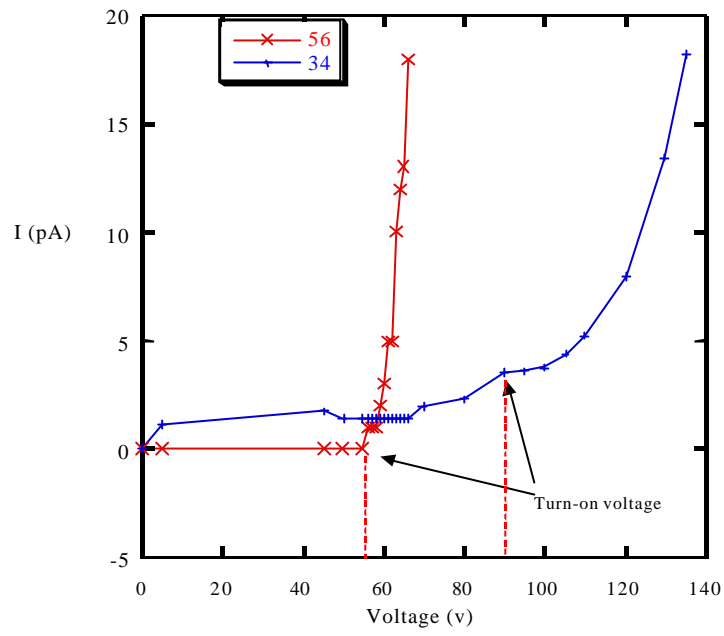
7.4 Summary

Low level current measurement systems as described in chapter 3 were used for testing of the field emission devices. Presently there is no permanent measurement set up for these devices, each measurement required considerable organisation and work. Various precautions needed to be taken to keep the devices and equipment clean. The measurement range (pA) and

low success rate are additional difficulties in this research area. In-situ FIB testing of the device offers the unique possibility of overcoming poisoning by material removal and testing without breaking vacuum. Material was successfully removed from the field emission tip in the FIB without shorting the anode to the cathode. Field emission devices were also heated in the FIB to increase the success rate of device operation. Devices operated in UHV in picoampere range and one device operated with a turn-on voltage of 57 V. Field enhancement and emission area were calculated from Fowler Nordheim plots. The value of field enhancement factor is supported by another researcher. The devices tested were fabricated using relatively large beam current (350 pA) so it is possible that lower beam currents will result in lowering the turn-on voltage. Lowering of turn-on voltage combined with a material more robust towards arcing and poisoning may lead to commercial applications of field emission devices fabricated with the FIB in a field requiring focused electron beams.

7.5 References

32. W. P. Dyke and J. K. Trolan, *Phys. Rev.* **89**, 799 (1953).
33. F. Charbonnier, *J. Vac. Sci. Technol. B* **16**, 880 (1998).
34. H. H. Busta, *J. Micromech. Microeng.* **2**, 43 (1992).
35. R. E. Burgess, H. Kroemer, and J. M. Houston, *Phys. Rev.* **90**, 515 (1953).
36. D. Park, (Chapter 4), *Introduction to the Quantum Theory*, (McGraw-Hill, 1964).
37. L. W. Nordheim, *Roy. Soc. Proc.* **A121**, 626 (1928).
38. R. H. Fowler and L. Nordheim, *Roy. Soc. Proc.* **A119**, 173 (1928).
39. D. K. Roy, (Chapter 4), *Quantum Mechanical Tunnelling and its Applications*, (World Scientific Publishing, 1986).
40. M. Yun, A. Turner, R. J. Roedel, and M. N. Kozicki, *J. Vac. Sci. Technol. B* **17**, 1561 (1999).



Chapter 8

Conclusions and Future Work

FIB nanofabrication is a new and exciting field. Device applications and technological developments are expanding this field at a fast speed. Research work was focused on advancing the FIB technology, learning technological aspects of the FIB technique, which affects the fabrication parameters and learning the fundamental science involved in device fabrication. Research work was performed in this field on an in-situ FIB electrical measurement technique, direct measurement of FIB cut parameters and the development and testing of a lateral field emission device. The following sections discuss the conclusions drawn from the present work and the possible future directions for work in this field.

8.1 Conclusions

Nanofabrication using FIB progressed in different directions during this project. Firstly, the development of an in-situ FIB electrical measurement system led to various applications such as in-situ depth measurements of high aspect ratio nanometer scale cuts and for in-situ field emission measurements. Direct measurements of the FIB cut parameters such as the width and depth of the FIB line cuts were performed with AFM. These measurements led to better understanding of the various material and technological aspects that influence device fabrication. A new lateral field emission device was fabricated and tested for field emission. Devices operated in the picoampere range and one device due to a FIB sharpening process had a turn-on voltage of 57 V. The present device technology is an improvement on the previously reported lateral field emission device fabricated with FIB. Along with the work in these directions, information regarding material sputter rates was obtained and increased understanding regarding milling of multi-layer structures was achieved.

The developed in-situ FIB electrical measurement system was used for various applications such as in-situ depth measurements, in-situ field emission measurements and in-situ FIB heating. In-situ depth measurements are becoming increasingly important as

device applications involving nanofabrication increase. A new technique for measuring depth of nanometer scale high aspect ratio cuts and accurate end-point detection was developed, which uses this electrical measurement system. The accuracy and reproducibility of the technique was tested. AFM technique measured the accuracy of this technique for 1 μm wide cuts. The technique was tested on Nb tracks and it performed accurate thickness measurement on 50 nm wide and 400 nm deep cuts. This technique provides electrical information while milling a track, which can be interpreted to provide information regarding the shape of FIB cuts. The depth measurement method has applications in research areas such as fabrication of tunnel junctions and in areas where the sputtered material in the FIB milling needs to be minimised.

The in-situ electrical measurement system offers the unique possibility of sharpening of the field emission tips in the FIB and then measuring field emission characteristics without breaking vacuum. For this reason, a low level measurement system for in-situ FIB testing of field emission devices was constructed. Construction of a good in-situ FIB low level measurement was a major challenge. The system developed is useful for performing measurements on the developed field emission device and similar devices. An in-situ FIB heater was also developed, this heater was used for heating field emission devices before performing in-situ low level measurements. The heater was operated up to 100°C.

Direct measurements of FIB line cuts were performed with AFM in order to understand the effects of different materials and different technological parameters of the FIB on these types of cuts. Comparison of different techniques such as AFM, SEM and FIB showed that the AFM technique is best suited for low aspect ratio nanometer scale FIB cuts. During this study, a framework was defined for analysing the FIB milled line cuts with AFM. Terms such as the height of the sputtered material, the length of the sputtered material, the width and the depth milled of the FIB cut were defined. These definitions of terms can be used for similar measurements in the future. These parameters are important both for various device applications and for the fundamental understanding of the sputtering processes involved during FIB milling. Different beam currents and magnifications were used to mill FIB line cuts in Si, Nb and an amorphous material. AFM observations led to a number of interesting observations including:

- the formation of a deposit on the surface of Si during enhanced etch ion milling;

- wide variation in width of cut in Nb due to the presence of grains and
- different widths of cuts due to the use of different materials.

This investigation demonstrated the importance of the technological parameters when milling with the FIB. The investigation more importantly showed the significance of material effects such as the presence of oxides on the surface and the presence of grains, which can influence the quality of FIB line cuts.

A new lateral field emission device using Cr as field emission material was fabricated using the FIB. The technology developed uses a weak solution of KOH instead of HF, which was previously used for a similar reported device [1]. Due to this reason, the present device can be fabricated with various materials. FIB offers the flexibility of changing the anode to cathode distance, tip sharpness and the shape of the anode and cathode. During the course of this project, various shapes of the devices were fabricated, anode to cathode spacing below 100 nm and tip sharpness below 50 nm were achieved. Work on these factors with FIB has not been previously reported. Research work was also performed to develop ultra-sharp tips, which can be used for the study of field emission phenomenon. Testing of the devices is presently very difficult, as these devices are new to the device materials group and expert help is not available. Different field emission testing systems were built for testing the devices both in UHV and inside FIB. In-situ FIB testing of field emission device offers the unique possibility of overcoming poisoning by material removal and testing without breaking vacuum. Material was successfully removed from the field emission tip in the FIB without shorting the anode to the cathode. Field emission devices were also heated in the FIB to increase the success rate of device operation. These attempts were very successful as these led to both increased technical understanding of low level measurements and on a fundamental level led to understanding of the device failure mechanism. The device failure mechanism was studied thoroughly, which led to new ideas such as anodization of Al and coating of the devices. The devices were successfully operated in UHV in picoampere range and one device fabricated using a FIB sharpening process had a turn-on voltage of 57 V. Field enhancement and emission area was calculated from Fowler Nordheim plots.

Different materials and structures were milled while pursuing the above mentioned directions. Materials which were milled during the course of the project include: Al, Cr, Nb, Au, SiO₂, Si₃N₄ *etc.* and their multi-layered structures. Milling rate of these materials

were calculated and the milling of the multi-layer structure involving Cr/Al/SiO₂ was studied using EPD. The study with EPD improved understanding regarding the milling process of such a structure in the FIB.

8.2 Future work

The market for micromachining products was estimated in 1990 as \$492 million, which was expected to increase to \$14 billion in 2000 and \$38 billion by year 2002 [2]. These figures suggest that nanotechnology will be one of the most important technologies in the future. Devices in this field range from MEMS devices for example accelerometers that are already commercialised to single-electron transistors which have been developed. FIB has been used extensively for the development of new concept nanodevices such as field emission device, superconductive Josephson devices, accelerometer and for the fundamental understanding of quantum physics in the frame of nanoscale structure. Since considerable amount of knowledge regarding nano scale fabrication and FIB cut parameters was gained during this project, this knowledge can be applied for further development of futuristic nanostructures with FIB.

The present in-situ FIB measurement system was used for depth measurements along with other measurements. The depth measurements involved a single metal track, a study should be conducted for tracks involving two materials, this study is important for devices which involve milling through two materials. A simple model was constructed during the course of the project for the resistance change while a bi-layer track is milled, however no experimental work could be done in this direction. The in-situ FIB heater can also be used for various applications such as:

- to study the effects of heating on ion and electron emission properties of materials in the FIB and
- to study the effect of heating on semiconductor materials inside the FIB.

FIB line cuts should be studied for materials such as GaN which has applications for optical devices [3,4]. In these materials, width measurements can be more accurately performed using an AFM super tip. This will lead to better quality of measurements and measurement of high aspect ratio structures.

One promising application of the deposit observed on the surface of Si while ion milling using enhanced etch is nanolithography. The deposit can be fabricated on the surface of Si with enhanced etch using low ion beam currents. By using this deposit as a mask on the surface of Si and then milling the specimen with Ar ion milling, it may be possible to fabricate nanometer scale lines.

A 3-electrode field emission device which has a gate, anode and a cathode can be fabricated using the fabrication process developed during the course of the project. Appendix 3 shows schematic of a photolithographic mask which can be used for the fabrication of such a device. The fabrication process can be further improved by experimentation with chemicals using the displacement reaction as discussed in chapter 3. Carrying out the reaction in an ultra-sonic bath may lead to better coating of the devices.

Nanofabrication using FIB is an expanding field, only future directions which directly follows from this project were suggested above. There are various other future directions which can be pursued for example fabrication of AFM tips, nanolithography, mask imprinting *etc.* AFM tips modification using the FIB leads to tip with high aspect ratios, thus these tips can be used for performing measurements on high aspect ratio structures. Various materials have been used for lithography using the FIB, these are discussed in

chapter 2. The scale of fabrication with these materials can be improved for applications at the nano scale. Mask imprinting is presently developed in device materials group and will substantially gain from the work done in the present project.

8.3 References

1. Y. Gotoh, T. Ohtake, N. Fujita, K. Inoue, H. Tsuji, and J. Ishikawa, *J. Vac. Sci. Technol. B* **13**, 464 (1995).
2. H. Fujita, *Sens. Actuators A* **56**, 105 (1996).
3. A. J. Steckl and I. Chyr, *J. Vac. Sci. Technol. B* **17**, 362 (1993)
4. M. H. F. Overwijk and J. A. de Poorter, *J. Appl. Phys.* **74**, 7048 (1993).

Appendixes

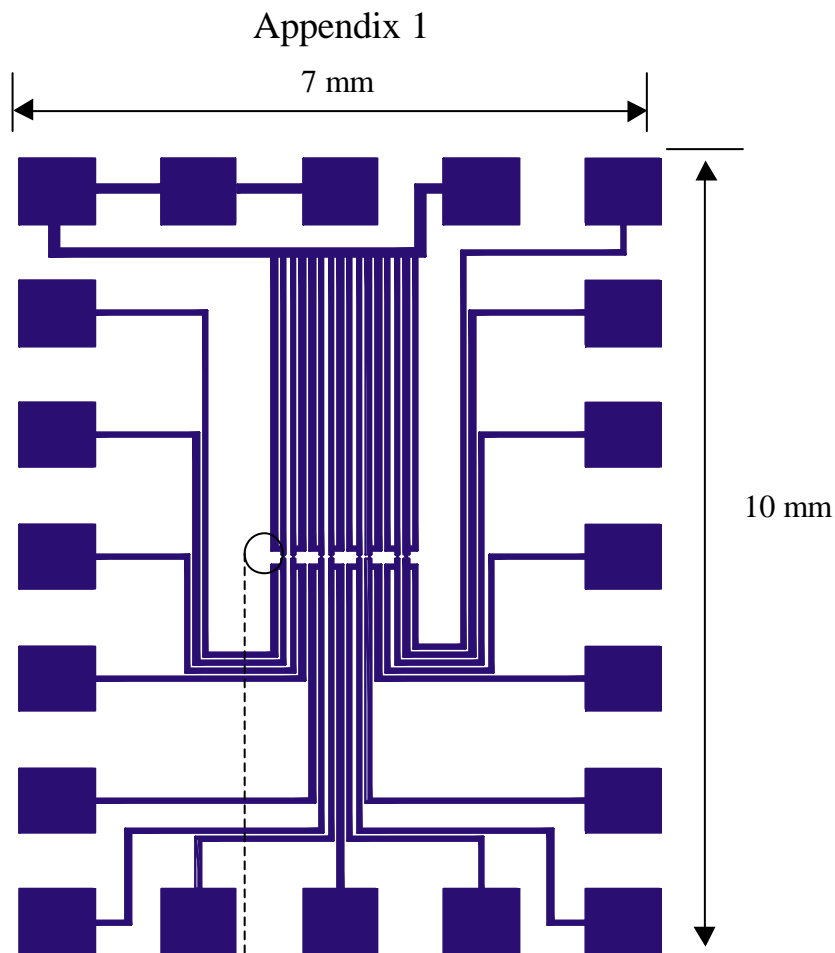


Figure 1-A. Photolithography mask design used for the fabrication of field emission devices.

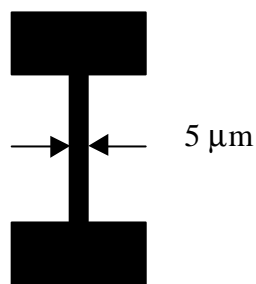


Figure 1-B. Zoomed in diagram of the central part of the mask, this area was used for the fabrication of field emission devices.

Appendix 2

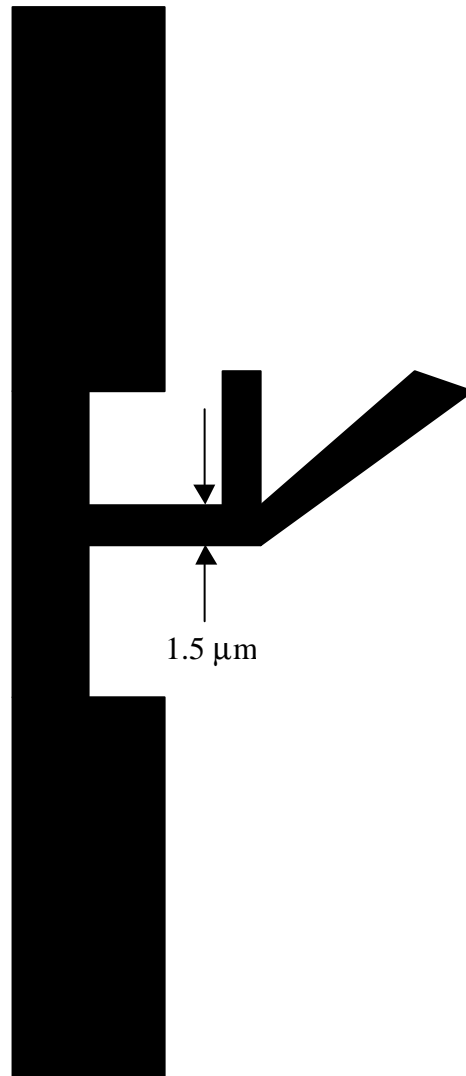


Figure 2-A. A section of the mask design used for four point measurements. The portion of the track which was milled is shown as 1.5 μm.

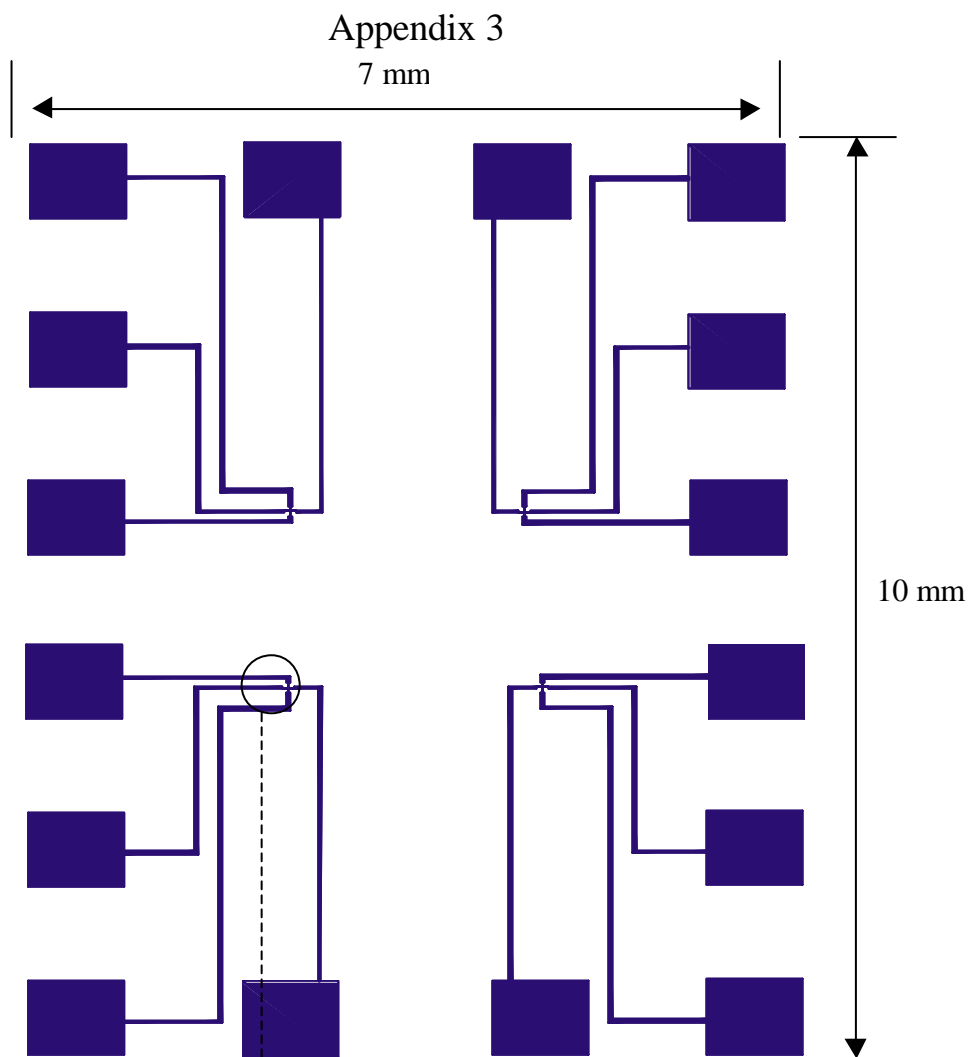


Figure 3-A. Photolithography mask design for a triode.

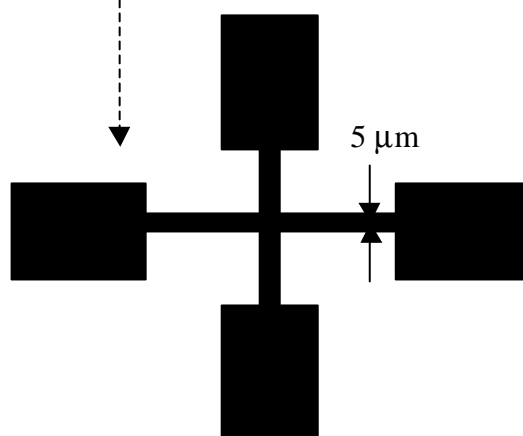


Figure 3-B. Zoomed diagram of the central part of the photolithography mask. This area can be used for the fabrication of a triode device.

Appendix 4

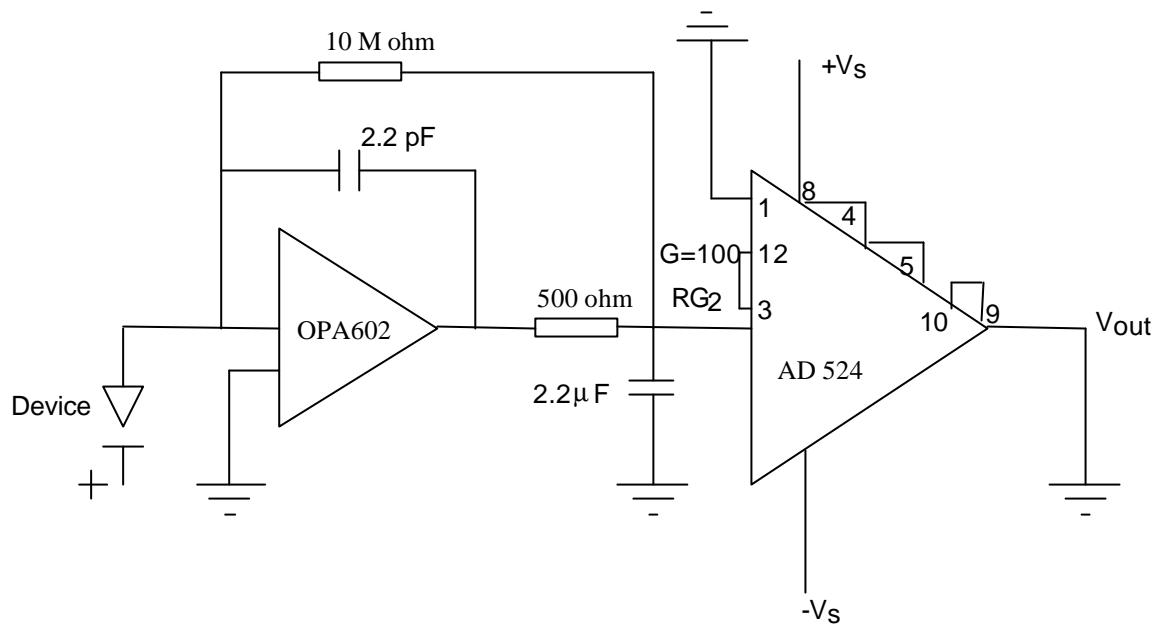


Figure 4-A. Electronics circuit used for field emission measurements.